Synthesis and Characterisation of NASICON-Type Structured Lithium-Ion Conductors with Dielectric Particle Dispersion

SONG Fangzhou (6560-31-7851)

Fundamental Energy Science Department

Graduate School of Energy Science

Kyoto University

Contents

1. Introduction

1.1. Lithium-ion batteries and solid-state electrolytes

1.1.1. Fundamentals of lithium-ion batteries

Owing to the deterioration of global warming, the global temperature is continuously breaking newest high records staring from year 2000 [1,2], accompanying which with extreme climates and weather hazards such as droughts, floods, hurricanes, and wildfires (Fig 1.1). This could cause great damage to our natural environment as well as our society, raising costs for all kinds of productions [3,4]. Curbing of the worsening of climate change requires instant cut in green-house gas emissions through reduction in fossil fuel consumptions. Viable pathways to fulfil such goal involve two types of transitions in the society: i) switching to renewable energies as our major energy source instead of fossil fuel-fired power, and ii) electrification of all kinds of transportations. Successful implementation of both transitions deeply relies on the battery technology to serve as balancing capacity for the intermittent renewable energies, as well as mobile energy storages to power up the vehicles [5,6].

Among all sorts of battery technologies [7–9], the potential of lithium-ion batteries (LIBs) has been proven by its commercial success in the last two decades thanks to their high energy density and rechargeability (i.e., long cycle life). The secondary LIBs operate on a principle of intercalation chemistry at the anode and cathode, as shown in Fig 1.2 [10]. During charging, lithium ion is extracted from the anode at an expense of anode oxidation. The electrons created from the oxidation are conducted through external circuit to the cathode, where the arrival of electron and insertion of the lithium ion completes the reduction reaction. In this process, the electrolyte sandwiched between the electrodes acts as a conduit that conducts lithium ions from one electrode to another by its high ionic conductivity, and 'forces' electrons to travel in external circuit to apply work with its low electronic conductivity. As the charge transport within the battery is established and proceeds, an electric potential between the cathode and anode will be formed with an equilibrium voltage V_0 that is dictated by the difference in chemical potentials between the anode (μ_a) and the cathode (μ_c):

$$\frac{\mu_a - \mu_c}{nF} = V_0 \qquad (1.1)$$

where n is the number of electron transferred per mole of redox reaction, F is the Faraday constant.

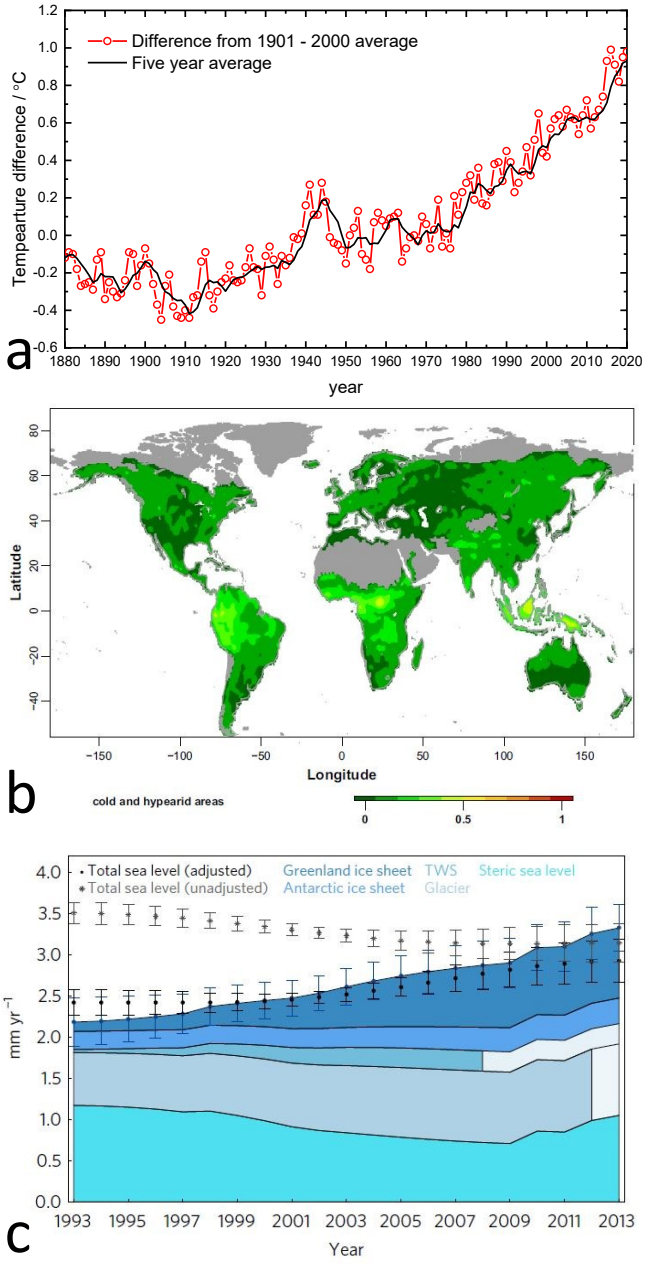

Figure 1.1 (a) Annual global mean surface temperature anomaly from 1880 to 2020, data obtained from ref. [2]. (b) Global map of drought in correlation with temperature rise [11]. (c) Global mean sea level rise by year [12].

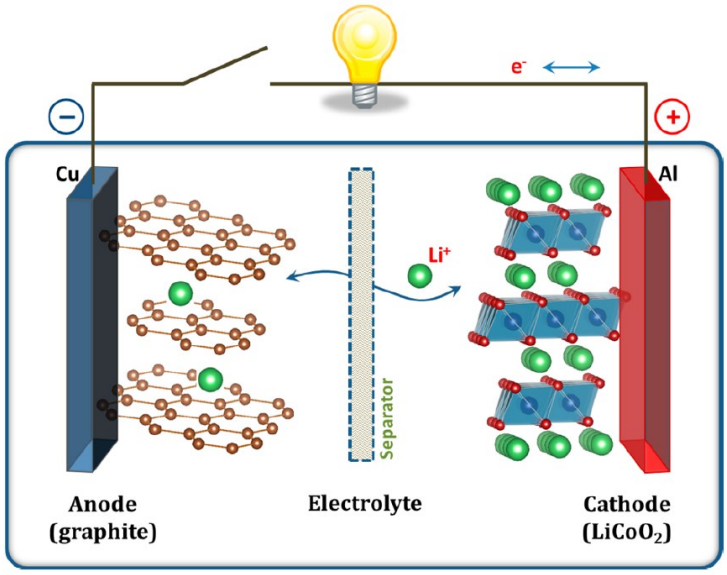

Figure 1.2 Schematic of lithium intercalation at electrodes and lithium-ion migration along electrolytes in lithium-ion battery [10].

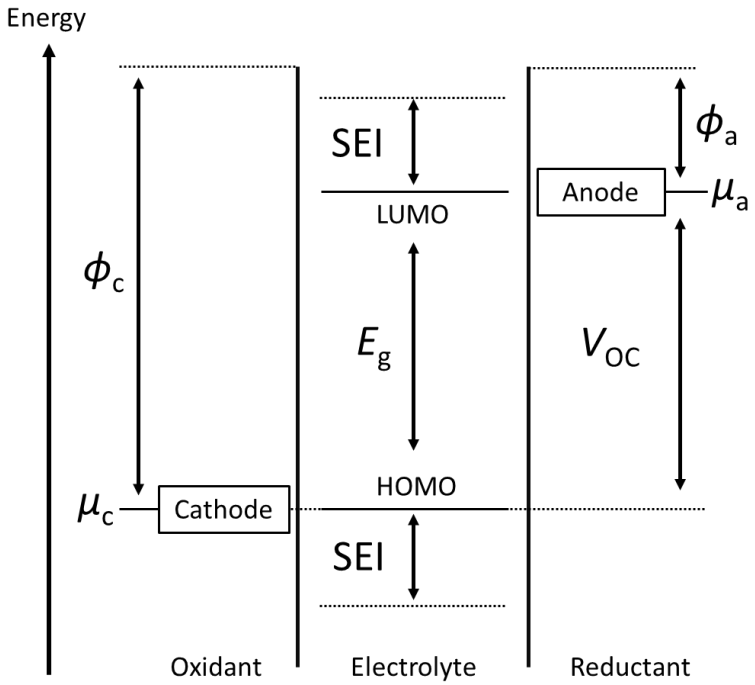

Figure 1.3 Schematic of the energy diagram of cathode (μ_c), electrolyte (E_g = LUMO − HOMO), and anode (μ_a). ϕ_c, ϕ_a and V_{OC} stands for the over potential applied to cathode, anode, and equilibrium voltage V_0 under open circuit condition. The graph is adapted from ref. [13]. Note that for solid-state electrolytes, the E_g is defined by the gap between valence and conduction band edges instead of LUMO and HOMO [14].

The chemical potential μ and electrochemical potential $\bar{\mu}$ are equivalent during open circuit or discharging process where no external voltage is applied. During charging where the redox reaction is reversed, the electrochemical potential is determined by the applied potential ϕ as given in Eq 1.2:

$$\bar{\mu} = \mu + zF\phi \qquad (1.2)$$

where z is the ionic charge of the charge carrier ion in the intercalation process. Originally, the maximum potential a cell could provide (standard cell potential $E^{\ominus}$) is decided by the redox reaction that occur on the electrodes as the lithium ion is extracted (delithiation) or inserted (lithiation):

$$E^{\theta} = \varphi_c^{\theta} - \varphi_a^{\theta} \qquad (1.3)$$

where $\varphi_c{}^{\ominus}$ and $\varphi_a{}^{\ominus}$ are standard redox potential of the cathode and anode. During discharging, change in chemical composition of electrodes as a result of lithiation/delithiation causes the potentials to steadily decrease from standard cell potential, and *vice versa*. Deep delithiation could usually cause destabilisation for the electrodes, leading to irreversible sub-reactions and thereby a loss of rechargeability of the secondary battery. Take the graphite-$LiCoO_2$ cell as instance, the $LiCoO_2$ cathode is delithiated to form $Li_{1-x}CoO_2$ during charging. At delithiation deeper than x = 0.5, the $Li_{1-x}CoO_2$ becomes unstable and experience irreversible reactions at the surface and eventually damage the cell integrity [15,16]. This problem means that not all of the lithium ions in the electrodes can be reversibly intercalated, which is circumvented by limiting the operating voltage of the cell from the standard cell potential (maximum in theory) to a lower cut-off voltage during the discharge (e.g., from 4.1 V of $E^{\ominus}$ for $LiCoO_2$ to 3.6 V cut-off voltage). Nonetheless, researchers are often aiming to maximise $E^{\ominus}$ for its calculability, such that the cell can store as much energy with as less weight as possible.

Energy density ($W{\cdot}h{\cdot}g^{-1}$) is one of the parameters that are frequently used to assess the performance of a cell. The theoretical energy density E_d is calculated by:

$$E_{\mathrm{d}} = V_0 \times Q \qquad (1.4)$$

where Q is the gravimetric specific capacity ($A{\cdot}h{\cdot}g^{-1}$) of the charge transfer between electrodes, which is calculated by:

$$Q = \frac{nF}{3600M_{\mathrm{w}}} \qquad (1.5)$$

where M_w is the molar mass of the active material in the electrode. The capacity Q is defined as the amount of charge per unit mass (sometimes volume) that is transferred outside the cell under a constant current I_{dis} during discharge within an hour. In theory, both of V_0 and Q are decided by the properties of electrode materials, which explains the research incentives in developing new cathodes and anodes. In some cases, however, the V_0 can be restricted by the electrochemical stability window (ESW) of the electrolytes, such that the value of V_0 in Eq 1.5 is decided by ESW instead of μ_a and μ_c. The rationale behind optimisation of ESW for electrolytes will be introduced in following paragraphs.

Another parameter that values the transient electric work output of the cell is gravimetric specific power density ($W \cdot g^{-1}$), which is determined by the charge/discharge rate of the battery given by Eq 1.6 -1.8:

$$P = V_0 \times I \qquad (1.6)$$

$$= V_0 \times i_0\{\exp\left(\frac{\alpha F\eta}{RT}\right) - \exp\left[\frac{(1-\alpha)F\eta}{RT}\right]\} \qquad (1.7)$$

$$= V_0 \times \frac{RT}{nFR_{ct}}\{\exp\left(\frac{\alpha F\eta}{RT}\right) - \exp\left[\frac{(1-\alpha)F\eta}{RT}\right]\} \qquad (1.8)$$

where i_0 is the exchange current, α is the transfer coefficient, η is the polarisation, R and T are gas constant and absolute temperature, R_{ct} is the charge transfer resistant. Optimisation of P can produce a maximised power output for electric vehicles to travel in faster speed.

In terms of materials, most of the current commercialised LIBs employ liquid solution electrolytes composing of lithium salt such as $LiPF_6$ and organic solvent such as ethylene carbonate-dimethyl carbonate (EC-DMC) [17]. The organic solvent ensures a good lithium salt solubility and low viscosity. This combination results in a low activation energy and high conductivity for the lithium-ion migration, such that the polarisation resistance of the cell can be minimised [13,18,19]. However, the carbonate-based solvents are highly flammable, causing thermal runaway issues [20]. The employment of nonaqueous liquid solution electrolytes can also limit the maximum workable voltage V_0 for the battery. As shown in Fig 1.3, apart from the thermodynamic considerations of chemical potential difference between the electrodes ($E^{\ominus}$) and delithiation limit (cut-off voltage), the ESW of the electrolyte adds a third constraint to the maximum voltage that can be applied to and supported by the cell. The ESW is defined as the difference in electron energy level (E_g) between the lowest unoccupied molecular orbit (LUMO) and highest occupied molecular orbit (HOMO) of the electrolyte. To ensure the compatibility of

electrode with the electrolyte, the chemical potential of anode μ_a must be lower than the LUMO and that of cathode μ_c higher than the HOMO. In cases otherwise, although the formation of solid/electrolyte interface (SEI) can provide a tolerance margin, the electrolyte can still be reduced at the anode and/or oxidised at the cathode. For the existing LIBs, the electrode materials that are compatible with the electrolyte are heavily limited by the low ESW of the liquid electrolytes, which subsequently limits the equilibrium voltage V_0 and hence the energy density E_d of the cell [13,21–23]. In summary, the safety and efficiency challenges in LIBs require further developing of electrolyte components that satisfy following constraints:

i) Non-flammability, which is evaluated by the flash point (°C) of the electrolyte
ii) Wide ESW as measured by the E_g
iii) A high lithium-ion conductivity $\sigma_{Li} > 10^{-4}$ S·cm^{-1}
iv) Good interfacial contact with electrodes despite the changing electrode volume during charge/discharge
v) A low electronic conductivity $\sigma_e > 10^{-10}$ S·cm^{-1}

1.1.2. Solid-state electrolytes

Driven by the problems described above, research efforts in recent years have been diverted to the development of solid-state electrolytes with non-flammability and wide ESWs that formulates the safer and more energy-compact all-solid-state batteries (ASSBs) [24–28]. However, the relatively low ionic conductivity of the solid-state electrolytes is the main hurdle for the commercialisation of ASSBs, which accumulates further research interests upon the modifications of extant solid-state electrolyte, or development of new solid-state electrolytes with superionic lattice structures [28–33].

At current stage, the mainstream lithium-ion solid-state electrolytes can be categorised into three domains basing on the anions that construct the sublattice of the crystalline electrolyte materials: halides [34,35,44–46,36–43], sulphides [47], and oxides [33,48–52], among which the oxides are relatively stable at ambient environments and are therefore able to be processed with low costs. Among all kinds of crystalline oxide-based lithium-ion solid-sate electrolytes, following prominent candidates have been drawing most research attention:

i) Lithium analogous of Na-ion superionic conductor (NASICON) [52–55]
ii) Garnet-type $Li_{5+x}La_{3-x}A_xM_{2-y}B_yO_{12}$ (A = divalent, M = tri/tetravalent, B = pentavalent) [33,50,51]
iii) Perovskite-type $Li_{3x}La_{0.67-x}TiO_3$ (LLTO) [56,57]

iv) Li-ion superionic conductor (LISICON) [48,49,58,59]

The conductivities of the mentioned electrolytes as well as some of the halides and sulphides are compared in Fig 1.4. In this work, research is focused on modification of NASICON-type lithium-ion solid-state electrolytes, owing to its easy processability and high room temperature conductivity. The chemical composition of NASICON structure is defined as $NaM_2(PO_4)_3$ (M = Ge, Ti, or Zr), the superionic conductivity of which was firstly reported by Goodenough *et al.* [60]. Its lattice structure (space group $R\bar{3}c$) is composed of corner-sharing MO_6 octahedra and PO_4 tetrahedra that form 3-dimensional diffusion pathways for the sodium ion, as shown in Fig 1.5(a) [61]. The sodium ions can occupy two sites within the lattice: octahedral centre 6*b* site (Na1) and polyhedral centre 18*e* site (Na2). The sodium ion migrates along the 3-dimensional diffusion pathway through jumping between Na1 and Na2 sites, which requires the ion to overcome the coulombic repulsion imposed by a diffusion bottleneck formed by oxygen anions (shown in Fig 1.5 (b)), the size of which correlated with the activation energy of the diffusion [61,62]. Detailed introduction on displacement of particles in solids can be found in section 1.3. The lithium analogues of NASICON possess same $R\bar{3}c$ lattice structure with chemical composition expressed as $LiM_2(PO_4)_3$, where M = Ti or Ge, and therefore utilises a similar diffusion pathway as the NASICON, with a metastable site 36*f* (tetragonal centre) acting as intermediate location along the diffusion pathway: $6b \rightarrow 36f \rightarrow 18e \rightarrow 36f \rightarrow 6b$ [55]. The most prominent compositions of the lithium analogous NASICON are $Li_{1+x}Al_xTi_{2-x}(PO_4)_3$ and $Li_{1+x}Al_xGe_{2-x}(PO_4)_3$ developed by H. Aono *et al.* [54,63]. The partial substitution of the tetravalent titanium or germanium ions with trivalent aluminium ions introduces charge imbalance within the lattice, which is compensated by the increased lithium-ion concentration within the lattice, resulting in increased ionic conductivities. The ionic conductivity for LATP and LAGP was reported to be a function of the aluminium content and reaches optimum at $x = 0.3$ (LATP) and $x = 0.5$ (LAGP), respectively [53].

In efforts to enhance the ionic conductivity for the oxide-based solid-state electrolytes, techniques have been developed based on the principles in defect chemistry and crystallography, the most common methods being:

i) Aliovalent doping [64,65,74,75,66–73]

ii) Grain boundary modification [76–78]

iii) Sintering aid [79,80]

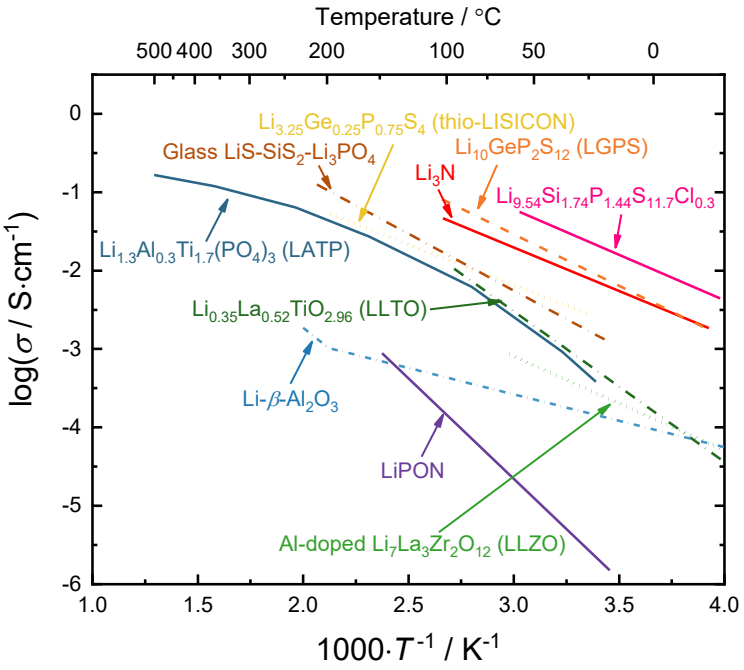

Figure 1.4 Electrical conductivity of inorganic solid-state lithium-ion electrolytes compared in an Arrhenius plot, data converted from ref [25] and ref [28].

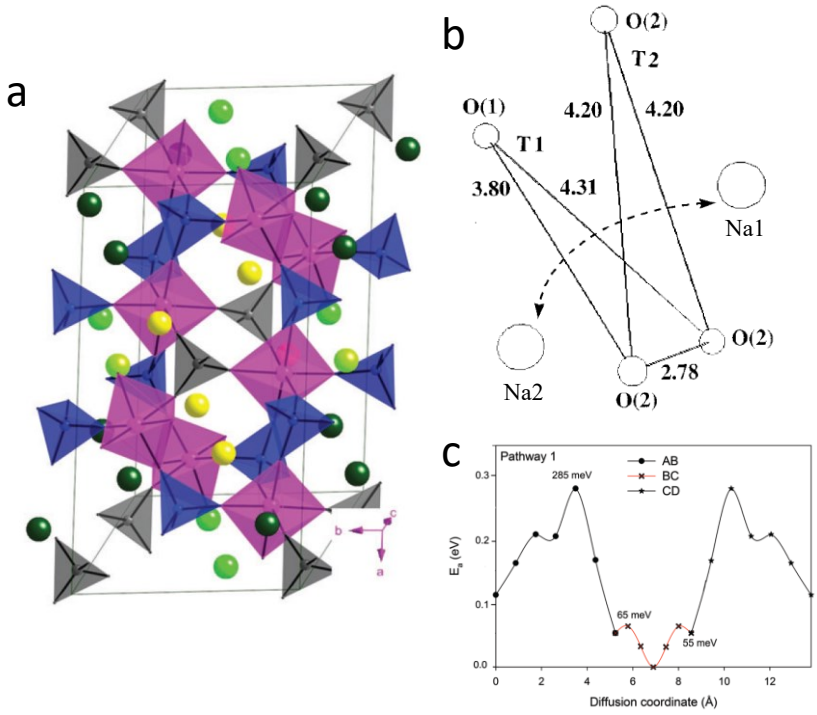

Figure 1.5 (a) Lattice structure of NASICON, Na1 and Na2 sites are represented by yellow and green balls. (b) Illustration of diffusion bottleneck between Na1 and Na2 sites. (c) Energy landscape of sodium ion diffusion from Na2 to Na1 (AB), Na1 to Na1 (BC), and Na1 to Na2 (CD). Graphs are converted from ref. [60] and [61].

Aliovalent doping is to deliberately include a (or more than one) foreign ion into the lattice of an ionic solid, such that the aliovalent ion substitutes the former host ion in the lattice [64]. The defect created by the aliovalent doping varies according to the valent of the foreign ion. In subvalent doping (foreign ion has lower valence), a cation interstitial defect or an anion vacancy defect (in most cases oxygen vacancy $V_{O}^{\cdot\cdot}$) will be created to compensate the charge imbalance introduced from the substitution. In the formation of LATP, for example, the Ti^{4+} in $LiTi_2(PO_4)_3$ (LTP) is substituted by Al^{3+}, which forms an interstitial lithium $Li_i^{\bullet}$:

$$Li_{Li}^{\times} + Al_2O_3 \overset{LTP}{\Longleftrightarrow} Al_{Ti}' + Li_i^{\bullet} + O_O^{\times} \quad (1.9)$$

where the Al_2O_3 is the dopant reagent added during synthesis as a source of Al^{3+}. Although the mechanism of how increment of lithium ion in LATP lattice enhances conductivity is still under dispute [65,66], it has been postulated that the increased lithium occupation at Li2 site (corresponding to the Na2 site introduced in NASICON) concentration within the lattice enhances the hopping rate of lithium-ion during diffusion and thereby increases the ionic conductivity [81]. On the other hand, in supervalent doping (foreign ion has higher valence), cation vacancies can be increased within the lattice. Good examples of modification through supervalent doping are the aluminium- and gallium-doped garnet-type solid electrolyte $Li_5La_3Zi_2O_{12}$ (LLZO), where the lithium-ion is substituted by Al^{3+} or Ga^{3+}, forming large amount of V_{Li}' that enhances the stability of highly ionically conductive phase at room temperature [67,72–75]. In some cases, the lattice parameter can also be tailored due to the large difference in ionic radii between the host and foreign ions, leading to expanded diffusion bottleneck which increases the ionic conductivity [68–71].

The grain boundary modification refers to modification of lithium-ion conductivity at the grain boundary through optimising the sintering process or grain boundary coating, which subsequently increases the total conductivity [76–78]. On the other hand, although adding sintering aid to the precursor during sintering introduces secondary phases to the grain boundary, the role of the intergranular phase is different from that in the grain boundary modification technique. Sintering aids (also called binder in some cases) are mostly low-melting-temperature phases that forms liquid phase at sintering temperature which aligns the grains of host solid-state electrolyte and/or enhances recrystallisation of the host grain. Under such effect, the densification of the sintered sample and hence the total conductivity can be improved [79,80]. Owing to the formation of liquid phase, this type of sintering is also referred to as liquid phase sintering.

It has to be noted that the techniques to improve the conductivity for the solid-state electrolytes are not straightforward and modification results in most cases are usually difficult to predict [71]. For example, substitution of Al^{3+} ions in LTP could introduce interstitial lithium-ions, and also expand the diffusion bottleneck, creating synergistic effects to enhance the conductivity [81]. In more complex cases, adding $NaSiO_3$ additive into NASICON to introduce liquid phase sintering behaviour can create a mixed effect of improvement in grain boundary conductivity and densification due to the existence of intergranular phase, but decreased bulk conductivity due to the loss of charge carrier sodium-ion in the bulk [82]. Therefore, successful modifications should always be coupled with thorough materials characterisation experiments, such that the mechanism of conductivity enhancement can be fully understood.

1.2. Insulative particle dispersion and space charge layer model

Different from homogenously altering the chemical composition or lattice structure of an ionic conductor, C. Liang achieved a 50-time enhancement in room-temperature conductivity by incorporating insulative Al_2O_3 particles in LiI solid electrolyte [83]. Such insulative particle dispersion effect has later been successfully translated into other halide-based ionic conductors, where the resulted electrolytes are usually categorised as composite electrolytes [84–93]. The initial phenomenological studies observed that the conductivity enhancement firstly increased to a maximum and then decreased with the volume fraction of the introduced insulative particles, with the extent of the enhancement inversely related to the particle sizes [83,86]. In effort to explain the conductivity enhancement on atomic scale, J. Wagner Jr. adapted the concept of space charge region that is originally used to model the depletion layer at the electron-hole interface in hetero-structured semiconductors [84,86,94,95]. According to Wagner's adaptation, a depletion layer of point defect is formed as an effort to align the Fermi energy of two phases and establish equilibrium at the hetero-interface between the ionic conductor and the insulative particle [28,84,87–90,96]. J. Maier has proven from the perspective of defect chemistry that, for insulative particles with nucleophilic surface, formation of such depletion layer can eliminate the electrical neutrality at space charge regions [28,88,89,93,96–98]. The pre-existing defect equilibrium in ionic conductors with Frenkel intrinsic disorder can be described as [97,99]:

$$M_M^{\times} + V_i \leftrightarrow M_i^{\bullet} + V_{\mathrm{M}}' \qquad (1.10)$$

At the hetero-interface, this equilibrium can be separated into two steps with interfacial cation defect $M_s^{\bullet}$ as bridging species [97,99]:

$$M_M^{\times} + V_{\mathrm{S}} \leftrightarrow M_{\mathrm{S}}^{\bullet} + V_{\mathrm{M}}' \qquad (1.11)$$

$$M_{\mathrm{S}}^{\bullet} + V_i \leftrightarrow V_{\mathrm{S}} + V_{\mathrm{M}}' \qquad (1.12)$$

For insulative particles with cation stabilising surface (i.e., nucleophilic), Eq 1.11 will be shifted towards the right, while Eq 1.12 towards the left. This could lead to increased amount of cation vacancies but decreased amount of interstitial cation defects at the interface, as shown in the Brouwer diagram in Fig 1.6 [97]. This boundary region with absent electric neutrality contributed by redistribution of ionic defect is denoted as space charge layer, and the related method of local defect introduction is usually referred to as heterogenous doping [98,99]. The space charge layer can improve the ionic conductivity by either i) creation of diffusion pathways with new kinetics,

or ii) direct influence on conductivity through change in point defect concentration [99]. For the role of defect concentration in the conduction of charge carrier ions, see section 1.3. The local defect density enhancement ζ_j can be described as a function of spatial position x in relation to the Debye length λ of the space charge layer [96,97,99]:

$$\zeta_j = \frac{[1+\exp\left(\frac{-x}{\lambda}\right)\theta_j]^2}{[1-\exp\left(\frac{-x}{\lambda}\right)\theta_j]^2} \qquad (1.13)$$

where j denotes the type of the point defect (vacancy V or interstitial i), θ_j is a phenomenological parameter representing the degree of influence from the interface upon the point defect (0 to 1 stands for enrichment effect, −1 to 0 stands for depletion effect, 0 stands for no effect) [99]. For detailed derivation of the mathematical expressions, the readers are referred to the original works and subsequent review articles [96,99].

The Debye length λ indicates a distance from the immediate surface of the insulative particle within which the defect redistribution occurs. It directly dictates the thickness of the space charge layer [84,96,99–105]:

$$\lambda = [\frac{\varepsilon\varepsilon_0 RT}{2Fc_\infty}]^{\frac{1}{2}} \qquad (1.14)$$

where $\varepsilon\varepsilon_0$ stands for the absolute dielectric permeability of the ionic conductor, c_∞ is the defect concentration in the bulk. J. Maier has argued that the $\lambda(T)$ decreases with the temperature and results in decreased volume fraction of space charge layer and therefore reduced conductivity enhancement from the heterogenous doping at elevated temperatures [84,99]. However, such claim has not yet been supported by further calculations or experimental observations. Experimental determination of the Debye length requires precise measurement of the conductivity along and across the space charge layer, which is usually conducted on hetero-structured thin-film specimens [96]. The results usually range from a few to several tens of nm, which are found to be proportionally correlated with the extent of overall conductivity enhancement in the composite electrolytes [100–105]. The schematics of the microstructure of a composite electrolyte and the defect concentration at the hetero-interface are illustrated in Fig 1.7.

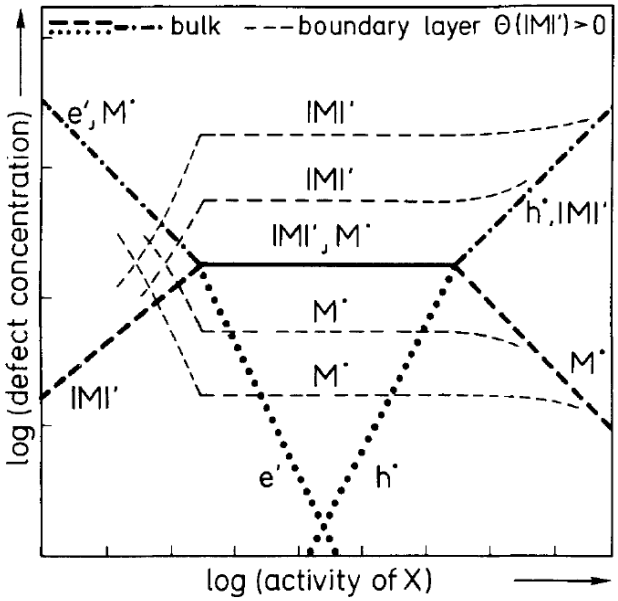

Figure 1.6 Brouwer diagram of point defect at bulk (thick dash lines or dotted lines) and space charge layer (thin dash line) of a composite electrolyte, with Frenkel intrinsic disorder in the matrix. e' and $h^{\bullet}$ stand for electronic defects (electron and hole). $M^{\bullet}$ and $|M|'$ stand for interstitial cation $M_i^{\bullet}$ and cation vacancy V_M'. As the spatial position becomes further from the hetero-interface, the deviation in defect concentration between the interstitial cation and cation vacancy becomes smaller and eventually returns to bulk level [97].

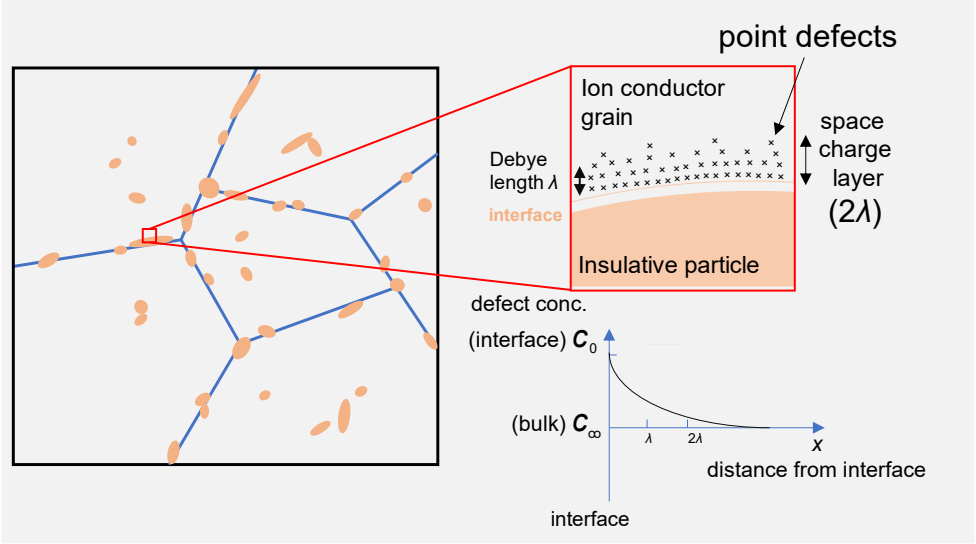

Figure 1.7 Schematics of microstructure of a composite electrolyte, and defect concentration at the space charge layer. The blue lines stand for grain boundary, orange islands are insulative particles, and cross marks represents point defects. The dimension of the interface is exaggerated. The typical size of the insulative particle is below 1 μm.

On the macroscopic scale, ignoring the conductivity of the insulative particles, the overall conductivity of the composite electrolyte σ_m can be generalised as [96,99]:

$$\sigma_m = \beta_\infty(1 - x_V)\sigma_\infty + \beta_L x_V \sigma_L \qquad (1.15)$$

where σ_∞ and σ_L are the conductivity in the bulk of the matrix phase and along the space charge layer, x_V is the volume fraction of the insulative particle, β_∞ and β_L are the parameters of bulk and space charge layer, taking the geometry, particle distribution and interfacial effect into account [96,99].

In efforts to quantitively define the β_∞ and β_L parameters, several models have been developed using different approaches to simplify the geometry in the microstructure of the composite electrolytes:

i) Resistor network model [106,107]
ii) Percolation model [108–111]
iii) Effective medium model [112–114]

Although no agreement has been reached upon which model fits best to the experimental observations, these models describe the conductivity of the composite electrolytes as functions of size and volume fraction of the introduced insulative particles [96]. In general, as the connectivity of the highly conductive hetero-interface (i.e., space charge layer) is increased with the volume fraction of the introduced insulative particles, the total conductivity reaches a peak level. Further introduction of the insulative particles will lead to particle aggregation which produces blocking effect and reduces the overall conductivity. The readers are referred to the original works for detailed descriptions [99,107,109,114,115].

In summary, for insulative-particle-dispersed composite electrolytes, the defect chemistry at the vicinity of the particle will be altered under the effect of the nucleophilic surface of the particle. The affected region of the ionic conductor matrix would increase in defect concentration as well as deviate from electric neutrality, forming a space charge layer which contributes to high ionic conductivity at room temperature. The conductivity enhancement is directly dictated by the size and volume fraction of the introduced insulative particle, which can be offset by the blocking effect of the aggregating particles at higher volume fractions. The space charge layer model constructed around the composite electrolytes has successfully fitted and predicted the experimental results in halide-based materials [88,112]. Many works have also reported experimental measurements of the conductivity along the space charge layer, cohering with the

prediction of the space charge layer model [87,91,116–118]. The insulative particle dispersion (or heterogenous doping) technique is therefore proven to be an effective and predictable modification method in solid-state electrolytes for room-temperature applications. Similar to the homogenous doping technique, the heterogenous doping can also give rise to one or more unexpected effect that may be for or against conductivity enhancement, typical instances being: i) formation of highly conductive intergranular phases [77,80,119,120], introduction of high-dimension defects around the particles due to the mismatch of thermal expansion coefficients of the particle and matrix [121,122], or adjusted microstructure due to grain boundary pinning (Zinner pinning), heterogeneous recrystallisation, or liquid-phase-aided preferential grain growth [79]. This layer of complexity therefore requires comprehensive investigation techniques when tackling with determination of conductivity enhancement mechanisms in composite electrolytes.

1.3. Mass transportation in solid-state electrolytes

1.3.1. Diffusion in solids

As introduced in section 1.1, to carry the internal current through mass transportation of charge carrier ions is a primary requirement for a functioning solid-state electrolyte in ASSBs. As a method of studying the motion of matter along certain direction in solids, the particles can be quantified in form of flux (number of particles per unit area) *j*. Similar to that of heat flux, the flux of substance particles is the result of random molecular motion under the influence of concentration gradient *dc*/*dx* along the direction of mass transport, as defined by Fick's first law of diffusion [123,124]:

$$j = -D\frac{dc}{dx} \qquad (1.16)$$

This equation describes the transient mass flux *j* at a given time instance to be proportional to the local concentration gradient of the diffusing species by a coefficient *D* (chemical diffusion coefficient). To consider the evolution of concentration *c* (*x*, *t*) with time, Fick's second law of diffusion dictates that change of concentration per unit time ($\partial c/\partial x$) is proportional to the negative value of the change of flux *j* with spatial position ($\partial j/\partial x$):

$$\frac{\partial c}{\partial t} = -\frac{\partial j}{\partial x} \qquad (1.17)$$

$$= -\frac{\partial}{\partial x}\left(-D\frac{dc}{dx}\right)$$

$$\frac{\partial c}{\partial t} = D\frac{\partial^2 c}{\partial x^2} \qquad (1.18)$$

Given different boundary conditions and their related assumptions, Eq 1.18 can be explicitly solved with different solutions. The readers are referred to the original work by J. Crank for the detailed boundary conditions and their correlated solutions [125].

The diffusion of matter is a collective result of large number of particles jumping from one site to another for multiple times. On atomic level, with absent of applied electric potential, the jump attempts of the particle (in 1 dimension) can be described by the random walk model [126]:

$$j = -\frac{1}{2}a^2\nu\frac{dc}{dx} \qquad (1.19)$$

where *a* is the total distance of displacement after multiple jumps, *v* is the mean frequency of jump during the distance *a*, the factor 1/2 means that half of the jumps are along the desired flux

direction. By comparing Eq 1.19 with Eq 1.16, one can realise that:

$$D = \frac{1}{2}a^2\nu \qquad (1.20)$$

In long-range mass transportation where a large number of jump n occurs within time t, the mean jump frequency ν can be expressed by n/t, such that:

$$na = x = \sqrt{2Dt} \qquad (1.21)$$

This expression relates the random travel distance of particle a to the collective displacement of the diffusing species along the flux direction x. Eqs 1.20 and 1.21 suggest that the diffusion coefficient can be measured on both microscopic (measuring a and ν) and macroscopic (measuring x and t) scales [127].

Except for the diffusion driven by the concentration gradient and the related chemical diffusion coefficient, particles also experience the self-diffusion in a chemically homogenous solid in absence of external electric field or chemical potential. This type of diffusion represents the spontaneous mixing of atoms driven by the thermal motions, where the vibrating particles exchange positions with their neighbouring vacancy or particles. The self-diffusion can be experimentally tracked using labelled particles (isotopes) as 'tracer'. Since the labelled particle is chemically identical to the unlabelled particle, the interchange of the particles is purely driven by the thermal motion (i.e., self-diffusion). Neglecting the mass difference between the isotopes, the so-called tracer diffusion coefficient D^* measured from the labelled particles can be treated as self-diffusion coefficients [125].

1.3.2. Conductivity

For charged particles such as lithium ions in solid-state electrolytes, except for dc/dx, the ion migration can also be driven by the external electric field E or electrochemical potential. The displacement of the charged particles can generate internal ionic current within the ASSB that supports redox reactions at electrodes during the charging and discharging processes, the current density i of which can be expressed by [126]:

$$i = zqcv \qquad (1.22)$$

where z and c are the valence and concentration of the charge carrier, q is the charge of electron. The drift velocity v of the charge carrier is defined as the product of the mobility of ions μ_i and electric field E:

$$v = \mu_i E \qquad (1.23)$$

Relating Eq 1.23 to Eq 1.22, and apply Ohm's law to the current density:

$$i = zqc\mu_i E$$

$$\frac{i}{E} = \frac{1}{\rho} = \sigma_i = zqc\mu_i \qquad (1.24)$$

where ρ is the resistivity of the solid-state electrolyte, and σ_i is the ionic conductivity. Eq 1.24 indicates that under electrochemical potential, higher ionic conductivity allows the solid-state electrolyte to support higher ionic current and therefore a faster charge/discharge rate for the ASSB.

On the atomic scale. the migration of ions in solid relies on defects in lattice. In real solids, the intrinsic disorder (Frenkel or Schottky) can generate point defects which are essentially unoccupied sites or interstitial ions in the lattice. Any mobile ions that are adjacent to the vacant site is able to hop from its original position to the unoccupied position with an expanse of activation energy E_a as shown in Fig 1.8(a). Take LATP for example, considering equation 1.24, the charge carrier lithium-ion must be 'coupled' with a point defect to become mobile. Therefore, the concentration of *mobile* charge carrier c is decided by the concentration of point defects in LATP. This explains why the enhancement in defect concentration at the vicinity of insulative particles introduced in section 1.2 can result in enhancement in local conductivity.

Without external electric field, the hopping of an ion to the neighbouring vacancy occurs with a probability P that is defined as (1 dimension):

$$P = \upsilon_0 \exp\left(\frac{-E_a}{k_B T}\right) \qquad (1.25)$$

where υ_0 is the attempt frequency of hopping, k_B is the Boltzmann's constant. As shown in Fig 1.8, the energy landscape is distorted with the presence of an external electric field E, such that energy barrier for the ion to hop along and against the electric field are reduced and increased by a same amount. The probability for the 'forward' and 'reverse' hopping becomes:

$$P' = \upsilon_0 \exp\left[\frac{-\left(E_a - \frac{1}{2}aEq\right)}{k_B T}\right] \qquad (1.26)$$

$$P'' = \upsilon_0 \exp\left[\frac{-\left(E_a + \frac{1}{2}aEq\right)}{k_B T}\right] \qquad (1.27)$$

where the lattice constant a is considered as the hopping distance. In real systems where the external filed E is relatively low, the drift velocity υ can be expressed by:

$$\upsilon = a(P' - P'') = a\upsilon_0 \exp\left(\frac{-E_a}{k_B T}\right) \times \frac{aEq}{k_{BT}} \qquad (1.28)$$

Although the aEq/k_BT provides a relatively small change in energy barrier (Fig 1.8) for a single lithium ion, the probability change can become significant when considering all the lithium ions within an ionic conductor. Therefore, the ion mobility μ_i (which measures the collective migration behaviour of all the ion i in the system) can be represented by:

$$\mu_i = \frac{a^2 q \upsilon_0}{k_B T} \exp\left(\frac{-E_a}{k_B T}\right) \qquad (1.29)$$

The Arrhenius behaviour of ionic conductivity can therefore be represented by the following equation, *viz.*, $\ln(\sigma_i)$ is proportional to the reciprocal of absolute temperature $(1/T)$ by a factor of $-E_a/k_BT$.:

$$\sigma_i = \frac{za^2 q^2 c\upsilon_0}{k_B T} \exp\left(\frac{-E_a}{k_B T}\right) = \sigma_0 \exp\left(\frac{-E_a}{k_B T}\right) \qquad (1.30)$$

The ionic conductivity is also linked with the diffusion coefficient through the Nernst Einstein relation:

$$D_i = \frac{\sigma_i k_B T}{cq^2} \qquad (1.31)$$

In a most solids, multiple types of charge carrier can be mobile. Lithium-ions, electrons e' and holes $h^{\cdot}$ can simultaneously migrate from one electrode to another through solid-state electrolyte. The generalised conductivity for solids is often written as:

$$\sigma_m = \sum_j \sigma_j = \sum_j n_j q_j \mu_j \qquad (1.32)$$

To maximise the efficiency of desired redox reaction per charge transferred, the conductivity of lithium ion should be maximised. The conductivity ratio of charge carrier j to the total conductivity σ_m is called transference number t_j:

$$t_j = \frac{\sigma_j}{\sigma_m} \qquad (1.33)$$

For practical applications in ASSBs, the solid-state electrolyte should satisfy: $t_{Li} \rightarrow 1$ and $t_{e'} \rightarrow 0$. The readers are referred to a review article by J. Goodenough for detailed derivation of Eq 1.22-1.33 [126].

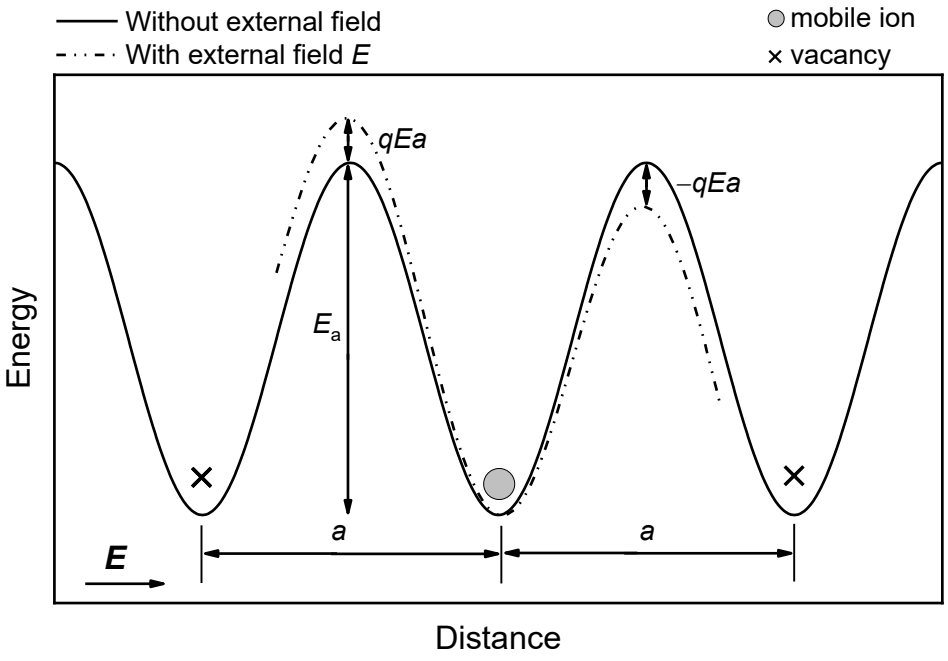

Figure 1.8 Schematic of energy landscape for ion-vacancy interchange, without (solid curve) and with the external electric field (dashed curve). The cross mark represents the position of vacancies, grey circle represents the position of a mobile ion with charge q. The original energy barrier is E_a, distances between the lattice sites (trough of the energy landscape) is represented by lattice parameter a. The external electric force $\boldsymbol{E}$ points rightwards. After application of external electric field, the energy barrier for a 'reverse' hopping is increased by qEa, while that along the external field is decreased by qEa. The figure is adapted from ref. [128].

1.4. Purpose of this study

In the previous sections, the rationales behind development of ASSBs and research values in modification of solid-state electrolytes (i.e., ionic conductors) have been introduced. This leads to a focus on improving ionic conductivity for solid-state electrolytes through insulative particle dispersion method. The mathematics and chemical defect mechanisms in space charge layer model is introduced to explain the origin of conductivity enhancement in particle dispersion method and predicts the general performance of this technique: i) the conductivity enhancement is function of volume fraction and size of the insulative particle, ii) maximum conductivity can be found with increasing addition of insulative particle, and iii) the conductivity enhancement is expected to be significant at around room temperature. Finally, theoretical concerns in study of the ion transportation in solids are introduced. Basic parameters of solid-state electrolytes such as diffusion coefficient and conductivity, and how these parameters are influenced by first-principal properties of the materials are introduced.

Although successful incorporation of insulative particle dispersion technique has been achieved in halide-based ionic conductors [84–86,88,89,91–93], the modified products are still insufficient in several ways to be used as solid-state electrolytes in ASSBs:

i) Large scale production of halide-based materials requires strict environments without humidity or air, which are expensive to construct and maintain
ii) The resulting conductivities are still inferior to the non-aqueous liquid solution electrolytes

On the other hand, the productions of oxide-based ionic conductors are less demanding (in most cases ambient environment) and less energy intense, while the ionic conductivity for most of the oxide-based solid-state electrolytes are inherently higher than that of halides (10^{-3} S·cm^{-1} compared with 10^{-6} S·cm^{-1}) [25,129]. These features enable ASSB to be produced with higher power density and lower costs.

Among the oxide-based systems, NASICON-type structured LATP and LAGP are two of the promising candidates due to their low processing temperatures and relatively high room-temperature ionic conductivities (10^{-4}-10^{-3} S·cm^{-1}) [53]. With these considerations, the research goal of this work is to improve the ionic conductivity of NASICON-type structured solid-state electrolytes using insulative particle dispersion technique and perform in-depth characterisations to identify how space charge layer affect conductivities in oxide-based systems.

1.5. References

[1] S. Rahmstorf, G. Foster, N. Cahill, Global temperature evolution: recent trends and some pitfalls, Environ. Res. Lett. 12 (2017) 54001. https://doi.org/10.1088/1748-9326/aa6825

[2] NOAA National Centers for Environmental Information, Climate at a Glance: Global Time Series, (2021). https://www.ncdc.noaa.gov/cag/ (accessed November 8, 2021).

[3] N.W. Arnell, J.A. Lowe, A.J. Challinor, T.J. Osborn, Global and regional impacts of climate change at different levels of global temperature increase, Clim. Change. 155 (2019) 377–391. https://doi.org/10.1007/s10584-019-02464-z

[4] T. Iizumi, J. Furuya, Z. Shen, W. Kim, M. Okada, S. Fujimori, T. Hasegawa, M. Nishimori, Responses of crop yield growth to global temperature and socioeconomic changes, Sci. Rep. 7 (2017) 1–10. https://doi.org/10.1038/s41598-017-08214-4

[5] J. Rugolo, M.J. Aziz, Electricity storage for intermittent renewable sources, Energy Environ. Sci. 5 (2012) 7151–7160. https://doi.org/10.1039/C2EE02542F

[6] J.P. Barton, D.G. Infield, Energy storage and its use with intermittent renewable energy, IEEE Trans. Energy Convers. 19 (2004) 441–448. https://doi.org/10.1109/TEC.2003.822305

[7] D.O. Akinyele, R.K. Rayudu, Review of energy storage technologies for sustainable power networks, Sustain. Energy Technol. Assessments. 8 (2014) 74–91. https://doi.org/10.1016/j.seta.2014.07.004

[8] G.L. Soloveichik, Battery technologies for large-scale stationary energy storage, Annu. Rev. Chem. Biomol. Eng. 2 (2011) 503–527. https://doi.org/10.1146/annurev-chembioeng-061010-114116

[9] S. Manzetti, F. Mariasiu, Electric vehicle battery technologies: From present state to future systems, Renew. Sustain. Energy Rev. 51 (2015) 1004–1012. https://doi.org/10.1016/j.rser.2015.07.010

[10] J.B. Goodenough, K.-S. Park, The Li-ion rechargeable battery: a perspective, J. Am. Chem. Soc. 135 (2013) 1167–1176. https://doi.org/10.1021/ja3091438

[11] H. Carrão, G. Naumann, P. Barbosa, Global projections of drought hazard in a warming climate: a prime for disaster risk management, Clim. Dyn. 50 (2018) 2137–2155. https://doi.org/10.1007/s00382-017-3740-8

[12] X. Chen, X. Zhang, J.A. Church, C.S. Watson, M.A. King, D. Monselesan, B. Legresy, C. Harig, The increasing rate of global mean sea-level rise during 1993–2014, Nat. Clim. Chang. 7 (2017) 492–495. https://doi.org/10.1038/nclimate3325

[13] J.B. Goodenough, Y. Kim, Challenges for rechargeable Li batteries, Chem. Mater. 22 (2010) 587–603. https://doi.org/10.1021/cm901452z

[14] T. Binninger, A. Marcolongo, M. Mottet, V. Weber, T. Laino, Comparison of computational methods for the electrochemical stability window of solid-state electrolyte materials, J. Mater. Chem. A. 8 (2020) 1347–1359. https://doi.org/10.1039/C9TA09401F

[15] R. V Chebiam, F. Prado, A. Manthiram, Comparison of the chemical stability of Li_{1-}

$_x$CoO$_2$ and Li$_{1-x}$Ni$_{0.85}$Co$_{0.15}$O$_2$ cathodes, J. Solid State Chem. 163 (2002) 5–9. https://doi.org/10.1006/jssc.2001.9404

[16] X.Q. Yang, X. Sun, J. McBreen, New phases and phase transitions observed in Li$_{1-x}$CoO$_2$ during charge: in situ synchrotron X-ray diffraction studies, Electrochem. Commun. 2 (2000) 100–103. https://doi.org/10.1016/S1388-2481(99)00155-1

[17] Y. Lu, J.A. Alonso, Q. Yi, L. Lu, Z.L. Wang, C. Sun, A High-Performance Monolithic Solid-State Sodium Battery with Ca^{2+} Doped $Na_3Zr_2Si_2PO_{12}$ Electrolyte, Adv. Energy Mater. 9 (2019) 1901205. https://doi.org/10.1002/aenm.201901205

[18] K. Hayashi, Y. Nemoto, S. Tobishima, J. Yamaki, Mixed solvent electrolyte for high voltage lithium metal secondary cells, Electrochim. Acta. 44 (1999) 2337–2344. https://doi.org/10.1016/S0013-4686(98)00374-0

[19] K. Xu, Nonaqueous liquid electrolytes for lithium-based rechargeable batteries, Chem. Rev. 104 (2004) 4303–4418. https://doi.org/10.1021/cr030203g

[20] L. Vogdanis, B. Martens, H. Uchtmann, F. Hensel, W. Heitz, Synthetic and thermodynamic investigations in the polymerization of ethylene carbonate, Die Makromol. Chemie Macromol. Chem. Phys. 191 (1990) 465–472. https://doi.org/10.1002/macp.1990.021910301

[21] D. Larcher, J.M. Tarascon, Towards greener and more sustainable batteries for electrical energy storage, Nat. Chem. 7 (2015) 19–29. https://doi.org/10.1038/nchem.2085

[22] J.G. Kim, B. Son, S. Mukherjee, N. Schuppert, A. Bates, O. Kwon, M.J. Choi, H.Y. Chung, S. Park, A review of lithium and non-lithium based solid state batteries, J. Power Sources. 282 (2015) 299–322. https://doi.org/10.1016/j.jpowsour.2015.02.054

[23] T. Famprikis, P. Canepa, J.A. Dawson, M.S. Islam, C. Masquelier, Fundamentals of inorganic solid-state electrolytes for batteries, Nat. Mater. (2019) 1–14. https://doi.org/10.1038/s41563-019-0431-3

[24] Z. Zou, Y. Li, Z. Lu, D. Wang, Y. Cui, B. Guo, Y. Li, X. Liang, J. Feng, H. Li, C-W. Nan, M. Armand, L. Chen, K. Xu, S. Shi, Mobile Ions in Composite Solids, Chem. Rev. 120 (2020) 4169–4221. https://doi.org/10.1021/acs.chemrev.9b00760

[25] Z. Zhang, Y. Shao, B. Lotsch, Y.-S. Hu, H. Li, J. Janek, L.F. Nazar, C.-W. Nan, J. Maier, M. Armand, L. Chen, New horizons for inorganic solid state ion conductors, Energy Environ. Sci. 11 (2018) 1945–1976. https://doi.org/10.1039/C8EE01053F

[26] Y.-Z. Sun, J.-Q. Huang, C.-Z. Zhao, Q. Zhang, A review of solid electrolytes for safe lithium-sulfur batteries, Sci. China Chem. 60 (2017) 1508–1526. https://doi.org/10.1007/s11426-017-9164-2

[27] J.-M. Tarascon, M. Armand, Issues and challenges facing rechargeable lithium batteries, in: V. Dusastre (Ed.), Materials for Sustainable Energy A Collection of Peer-Reviewed Research and Review Articles from Nature Publishing Group, Nature Publishing Group, UK, 2011: pp. 171–179. https://doi.org/10.1142/9789814317665_0024

[28] P. Knauth, Inorganic solid Li ion conductors: An overview, Solid State Ionics. 180 (2009) 911–916. https://doi.org/10.1016/j.ssi.2009.03.022

[29] T. Tang, P. Chen, W. Luo, D. Luo, Y. Wang, Crystalline and electronic structures of

lithium silicates: A density functional theory study, J. Nucl. Mater. 420 (2012) 31–38. https://doi.org/10.1016/j.jnucmat.2011.08.040

[30] R. Xiao, H. Li, L. Chen, Candidate structures for inorganic lithium solid-state electrolytes identified by high-throughput bond-valence calculations, J. Mater. 1 (2015) 325–332. https://doi.org/10.1016/j.jmat.2015.08.001

[31] Z. Gao, H. Sun, L. Fu, F. Ye, Y. Zhang, W. Luo, Y. Huang, Promises, challenges, and recent progress of inorganic solid-state electrolytes for all-solid-state lithium batteries, Adv. Mater. 30 (2018) 1705702. https://doi.org/10.1002/adma.201705702

[32] F. Zheng, M. Kotobuki, S. Song, M.O. Lai, L. Lu, Review on solid electrolytes for all-solid-state lithium-ion batteries, J. Power Sources. 389 (2018) 198–213. https://doi.org/10.1016/j.jpowsour.2018.04.022

[33] V. Thangadurai, S. Narayanan, D. Pinzaru, Garnet-type solid-state fast Li ion conductors for Li batteries: critical review, Chem. Soc. Rev. 43 (2014) 4714–4727. https://doi.org/10.1039/C4CS00020J

[34] T. Asano, A. Sakai, S. Ouchi, M. Sakaida, A. Miyazaki, S. Hasegawa, Solid Halide Electrolytes with High Lithium-Ion Conductivity for Application in 4 V Class Bulk-Type All-Solid-State Batteries, Adv. Mater. 30 (2018). https://doi.org/10.1002/adma.201803075

[35] R. Kanno, Y. Takeda, O. Yamamoto, Ionic conductivity of solid lithium ion conductors with the spinel structure: Li_2MCl_4 (M = Mg, Mn, Fe, Cd), Mater. Res. Bull. 16 (1981) 999–1005. https://doi.org/10.1016/0025-5408(81)90142-2

[36] H.D. Lutz, P. Kuske, K. Wussow, Ionic motion of tetrahedrally and octahedrally coordinated lithium ions in ternary and quaternary halides, Solid State Ionics. 28 (1988) 1282–1286. https://doi.org/10.1016/0167-2738(88)90371-2

[37] R. Kanno, Y. Takeda, O. Yamamoto, C. Cros, W. Gang, P. Hagenmuller, Ionic Conductivity and Phase Transition of the Bromide Spinels, $Li_{2-2x}M_{1+x}Br_4$ (M=Mg, Mn), J. Electrochem. Soc. 133 (1986). https://doi.org/1052. 10.1149/1.2108704

[38] R. Kanno, Y. Takeda, O. Yamamoto, Structure, ionic conductivity and phase transformation of double chloride spinels, Solid State Ionics. 28–30 (1988) 1276–1281. https://doi.org/10.1016/0167-2738(88)90370-0

[39] A. Bohnsack, F. Stenzel, A. Zajonc, G. Balzer, M.S. Wickleder, G. Meyer, Ternäre Halogenide vom Typ A_3MX_6. VI. Ternäre Chloride der Selten-Erd-Elemente mit Lithium, Li_3MCl_6 (M = Tb–Lu, Y, Sc): Synthese, Kristallstrukturen und Ionenbewegung, Zeitschrift Für Anorg. Und Allg. Chemie. 623 (1997) 1067–1073. https://doi.org/10.1002/zaac.19976230710

[40] Y. Tomita, K. Yamada, H. Ohki, T. Okuda, Cation Diffusion in $MGaBr_4$ (M = Li, Cu, and Ag) Studied by ^{7}Li, ^{63}Cu, and ^{71}Ga NMR, ^{81}Br NQR, and Conductivity, Bull. Chem. Soc. Jpn. 70 (1997) 2405–2410. https://doi.org/10.1246/bcsj.70.2405

[41] Y. Tomita, A. Fuji-i, H. Ohki, K. Yamada, T. Okuda, New Lithium Ion Conductor Li_3InBr_6 Studied by ^{7}Li NMR, Chem. Lett. (1998). https://doi.org/10.1246/cl.1998.223

[42] Y. Tomita, K. Yamada, H. Ohki, T. Okuda, Structure and dynamics of Li_3InBr_6 and $NaInBr_4$ by means of nuclear magnetic resonance, Zeitschrift Für Naturforsch. A. 53

(1998) 466–472. https://doi.org/10.1515/zna-1998-6-730

[43] Y. Tomita, H. Ohki, K. Yamada, T. Okuda, Ionic conductivity and structure of halocomplex salts of group 13 elements, Solid State Ionics. 136–137 (2000) 351–355. https://doi.org/10.1016/S0167-2738(00)00491-4

[44] Y. Tomita, H. Matsushita, K. Kobayashi, Y. Maeda, K. Yamada, Substitution effect of ionic conductivity in lithium ion conductor, $Li_3InBr_{6-x}Cl_x$, Solid State Ionics. 179 (2008) 867–870. https://doi.org/10.1016/j.ssi.2008.02.012

[45] R. Kanno, Y. Takeda, A. Takahashi, O. Yamamoto, R. Suyama, S. Kume, New double chloride in the LiCl–$CoCl_2$ system, J. Solid State Chem. 71 (2004) 196–204. https://doi.org/10.1016/0022-4596(87)90159-9

[46] R. Kanno, Ionic Conductivity and Phase Transition of the Spinel System $Li_{2-2x}M_{1+x}Cl_4$ (M = Mg, Mn, Cd), J. Electrochem. Soc. 131 (2006) 469. https://doi.org/10.1149/1.2115611

[47] S.P. Ong, Y. Mo, W.D. Richards, L. Miara, H.S. Lee, G. Ceder, Phase stability, electrochemical stability and ionic conductivity of the $Li_{10\pm1}MP_2X_{12}$ (M = Ge, Si, Sn, Al or P, and X = O, S or Se) family of superionic conductors, Energy Environ. Sci. 6 (2013) 148–156. https://doi.org/10.1039/c2ee23355j

[48] H.Y-P. Hong, Crystal structure and ionic conductivity of $Li_{14}Zn(GeO_4)_4$ and other new Li^+ superionic conductors, Mater. Res. Bull. 13 (1978) 117–124. https://doi.org/10.1016/0025-5408(78)90075-2

[49] P.G. Bruce, A.R. West, Ion trapping and its effect on the conductivity of LISICON and other solid electrolytes, J. Solid State Chem. 53 (1984) 430–434. https://doi.org/10.1016/0022-4596(84)90122-1

[50] R. Murugan, V. Thangadurai, W. Weppner, Fast lithium ion conduction in garnet-type $Li_7La_3Zr_2O_{12}$, Angew. Chemie - Int. Ed. 46 (2007) 7778–7781. https://doi.org/10.1002/anie.200701144

[51] R. Murugan, V. Thangadurai, W. Weppner, Lattice parameter and sintering temperature dependence of bulk and grain-boundary conduction of garnet-like solid Li-electrolytes, J. Electrochem. Soc. 155 (2007) A90. https://doi.org/10.1149/1.2800764

[52] K. Arbi, M. Hoelzel, A. Kuhn, F. Garcia-Alvarado, J. Sanz, Local structure and lithium mobility in intercalated $Li_3Al_xTi2\text{-}x(PO_4)_3$ NASICON type materials: a combined neutron diffraction and NMR study, Phys. Chem. Chem. Phys. 16 (2014) 18397–18405. https://doi.org/10.1039/C4CP02938K

[53] H. Aono, E. Sugimoto, Y. Sadaoka, N. Imanaka, G. Adachi, The electrical properties of ceramic electrolytes for $LiM_xTi_{2-x}(PO_4)_3 + yLi_2O$, M= Ge, Sn, Hf, and Zr systems, J. Electrochem. Soc. 140 (1993) 1827. https://doi.org/10.1149/1.2220723

[54] G. Adachi, N. Imanaka, H. Aono, Fast $Li^{\oplus}$ conducting ceramic electrolytes, Adv. Mater. 8 (1996) 127–135. https://doi.org/10.1002/adma.19960080205

[55] Y. Xiao, K. Jun, Y. Wang, L.J. Miara, Q. Tu, G. Ceder, Lithium oxide superionic conductors inspired by garnet and NASICON structures, Adv. Energy Mater. 11 (2021) 2101437. https://doi.org/10.1002/aenm.202101437

[56] M. Catti, First-Principles Modeling of Lithium Ordering in the LLTO ($Li_xLa_{2/3-x/3}TiO_3$) Superionic Conductor, Chem. Mater. 19 (2007) 3963–3972. https://doi.org/10.1021/cm0709469

[57] Y. Inaguma, C. Liquan, M. Itoh, T. Nakamura, T. Uchida, H. Ikuta, M. Wakihara, High ionic conductivity in lithium lanthanum titanate, Solid State Commun. 86 (1993) 689–693. https://doi.org/10.1016/0038-1098(93)90841-A

[58] P.G. Bruce, A.R. West, Phase diagram of the LISICON, solid electrolyte system, Li_4GeO_4-Zn_2GeO_4, Mater. Res. Bull. 15 (1980) 379–385. https://doi.org/10.1016/0025-5408(80)90182-8

[59] I. Abrahams, P.G. Bruce, W.I.F. David, A.R. West, A re-examination of the lisicon structure using high-resolution powder neutron diffraction: evidence for defect clustering, Acta Crystallogr. Sect. B. 45 (1989) 457–462. https://doi.org/10.1107/S0108768189006245.

[60] J.B. Goodenough, H.Y-P. Hong, J.A. Kafalas, Fast Na^+-ion transport in skeleton structures, Mater. Res. Bull. 11 (1976) 203–220. https://doi.org/10.1016/0025-5408(76)90077-5

[61] K.M. Bui, V.A. Dinh, S. Okada, T. Ohno, Na-ion diffusion in a NASICON-type solid electrolyte: a density functional study, Phys. Chem. Chem. Phys. 18 (2016) 27226–27231. https://doi.org/10.1039/C6CP05164B

[62] E.R. Losilla, M.A.G. Aranda, S. Bruque, M.A. Paris, J. Sanz, A.R. West, Understanding Na mobility in NASICON materials: a Rietveld, ^{23}Na and ^{31}P MAS NMR, and impedance study, Chem. Mater. 10 (1998) 665–673. https://doi.org/10.1021/cm970648j

[63] H. Aono, E. Sugimoto, Y. Sadaoka, N. Imanaka, G. Adachi, Ionic conductivity of solid electrolytes based on lithium titanium phosphate, J. Electrochem. Soc. 137 (1990) 1023. https://doi.org/10.1149/1.2086597

[64] Y. Feng, J. Wu, Q. Chi, W. Li, Y. Yu, W. Fei, Defects and aliovalent doping engineering in electroceramics, Chem. Rev. 120 (2020) 1710–1787. https://doi.org/10.1021/acs.chemrev.9b00507

[65] S. Wang, L. Ben, H. Li, L. Chen, Identifying Li^+ ion transport properties of aluminum doped lithium titanium phosphate solid electrolyte at wide temperature range, Solid State Ionics. 268 (2014) 110–116. https://doi.org/10.1016/j.ssi.2014.10.004

[66] A.D. Robertson, A.R. West, A.G. Ritchie, Review of crystalline lithium-ion conductors suitable for high temperature battery applications, Solid State Ionics. 104 (1997) 1–11. https://doi.org/10.1016/S0167-2738(97)00429-3

[67] J.L. Allen, J. Wolfenstine, E. Rangasamy, J. Sakamoto, Effect of substitution (Ta, Al, Ga) on the conductivity of $Li_7La_3Zr_2O_{12}$, J. Power Sources. 206 (2012) 315–319. https://doi.org/10.1016/j.jpowsour.2012.01.131

[68] A. Martinez-Juarez, C. Pecharromán, J.E. Iglesias, J.M. Rojo, Relationship between activation energy and bottleneck size for Li^+ ion conduction in NASICON materials of composition $LiMM'(PO_4)_3$; M, M' = Ge, Ti, Sn, Hf, J. Phys. Chem. B. 102 (1998) 372–375. https://doi.org/10.1021/jp973296c

[69] S. Stramare, V. Thangadurai, W. Weppner, Lithium lanthanum titanates: a review, Chem.

Mater. 15 (2003) 3974–3990. https://doi.org/10.1021/cm0300516

[70] J.C. Bachman, S. Muy, A. Grimaud, H.-H. Chang, N. Pour, S.F. Lux, O. Paschos, F. Maglia, S. Lupart, P. Lamp, L. Giordano, Y. Shao-Horn, Inorganic solid-state electrolytes for lithium batteries: mechanisms and properties governing ion conduction, Chem. Rev. 116 (2016) 140–162. https://doi.org/10.1021/acs.chemrev.5b00563

[71] S. Muy, J.C. Bachman, L. Giordano, H.-H. Chang, D.L. Abernathy, D. Bansal, O. Delaire, S. Hori, R. Kanno, F. Maglia, S. Lupart, P. Lamp, Y. Shao-Horn, Tuning mobility and stability of lithium ion conductors based on lattice dynamics, Energy Environ. Sci. 11 (2018) 850–859. https://doi.org/10.1039/C7EE03364H

[72] M. Amores, T.E. Ashton, P.J. Baker, E.J. Cussen, S.A. Corr, Fast microwave-assisted synthesis of Li-stuffed garnets and insights into Li diffusion from muon spin spectroscopy, J. Mater. Chem. A. 4 (2016) 1729–1736. https://doi.org/10.1039/C5TA08107F

[73] B. Xu, H. Duan, W. Xia, Y. Guo, H. Kang, H. Li, H. Liu, Multistep sintering to synthesize fast lithium garnets, J. Power Sources. 302 (2016) 291–297. https://doi.org/10.1016/j.jpowsour.2015.10.084

[74] D. Rettenwander, G. Redhammer, F. Preishuber-Pflügl, L. Cheng, L. Miara, R. Wagner, A. Welzl, E. Suard, M.M. Doeff, M. Wilkening, J. Fleig, G. Amthauer, Structural and electrochemical consequences of Al and Ga cosubstitution in $Li_7La_3Zr_2O_{12}$ solid electrolytes, Chem. Mater. 28 (2016) 2384–2392. https://doi.org/10.1021/acs.chemmater.6b00579

[75] J.-F. Wu, E.-Y. Chen, Y. Yu, L. Liu, Y. Wu, W.K. Pang, V.K. Peterson, X. Guo, Gallium-doped $Li_7La_3Zr_2O_{12}$ garnet-type electrolytes with high lithium-ion conductivity, ACS Appl. Mater. Interfaces. 9 (2017) 1542–1552. https://doi.org/10.1021/acsami.6b13902

[76] C.R. Mariappan, C. Yada, F. Rosciano, B. Roling, Correlation between micro-structural properties and ionic conductivity of $Li_{1.5}Al_{0.5}Ge_{1.5}(PO_4)_3$ ceramics, J. Power Sources. 196 (2011) 6456–6464. https://doi.org/10.1016/j.jpowsour.2011.03.065

[77] H. Yamada, D. Tsunoe, S. Shiraishi, G. Isomichi, Reduced grain boundary resistance by surface modification, J. Phys. Chem. C. 119 (2015) 5412–5419. https://doi.org/10.1021/jp510077z

[78] K. Takahashi, J. Ohmura, D. Im, D.J. Lee, T. Zhang, N. Imanishi, A. Hirano, M.B. Phillipps, Y. Takeda, O. Yamamoto, A super high lithium ion conducting solid electrolyte of grain boundary modified $Li_{1.4}Ti_{1.6}Al_{0.4}(PO_4)_3$, J. Electrochem. Soc. 159 (2012) A342. https://doi.org/10.1149/2.018204jes

[79] H. Aono, E. Sugimoto, Y. Sadaoka, N. Imanaka, G. Adachi, Electrical Properties and Sinterability for Lithium Germanium Phosphate $Li_{1+x}M_xGe_{2-x}(PO_4)_3$, M= Al, Cr, Ga, Fe, Sc, and In Systems, Bull. Chem. Soc. Jpn. 65 (1992) 2200–2204. https://doi.org/10.1246/bcsj.65.2200

[80] S. Hao, H. Zhang, W. Yao, J. Lin, Solid-state lithium battery chemistries achieving high cycle performance at room temperature by a new garnet-based composite electrolyte, J. Power Sources. 393 (2018) 128–134. https://doi.org/10.1016/j.jpowsour.2018.05.028

[81] G. Nuspl, T. Takeuchi, A. Weiß, H. Kageyama, K. Yoshizawa, T. Yamabe, Lithium ion migration pathways in $LiTi_2(PO_4)_3$ and related materials, J. Appl. Phys. 86 (1999) 5484–

5491. https://doi.org/10.1063/1.371550

[82] J.A.S. Oh, L. He, A. Plewa, M. Morita, Y. Zhao, T. Sakamoto, X. Song, W. Zhai, K. Zeng, L. Lu, Composite NASICON ($Na_3Zr_2Si_2PO_{12}$) solid-state electrolyte with enhanced Na^+ ionic conductivity: effect of liquid phase sintering, ACS Appl. Mater. Interfaces. 11 (2019) 40125–40133. https://doi.org/10.1021/acsami.9b14986

[83] C.C. Liang, Conduction Characteristics of the Lithium Iodide-Aluminum Oxide Solid Electrolytes, J. Electrochem. Soc. 120 (1973) 1289. https://doi.org/10.1149/1.2403248

[84] T. Jow, J.B. Wagner Jr, The effect of dispersed alumina particles on the electrical conductivity of cuprous chloride, J. Electrochem. Soc. 126 (1979) 1963. https://doi.org/10.1149/1.2128835

[85] K. Shahi, J.B. Wagner Jr, Ionic Conductivity and Thermoelectric Power of Pure and Al_2O_3-Dispersed AgI, J. Electrochem. Soc. 128 (1981) 6. https://doi.org/10.1149/1.2127390

[86] K. Shahi, J.B. Wagner Jr, Enhanced ionic conduction in dispersed solid electrolyte systems (DSES) and/or multiphase systems: Agl-Al_2O_3, Agl-SiO_2, Agl-Fly ash, and Agl-AgBr, J. Solid State Chem. 42 (1982) 107–119. https://doi.org/10.1016/0022-4596(82)90256-0

[87] U. Lauer, J. Maier, Impedance Spectroscopic Investigation of the Interface Silver Halide/Oxide: Detection of an Ionic Depletion Layer, J. Electrochem. Soc. 139 (1992) 1472. https://doi.org/10.1149/1.2069434

[88] J. Maier, Heterogeneous doping of silver bromide (AgBr:Al_2O_3), Mater. Res. Bull. 20 (1985) 383–392. https://doi.org/10.1016/0025-5408(85)90005-4

[89] J. Maier, On the heterogeneous doping of ionic conductors, Solid State Ionics. 18 (1986) 1141–1145. https://doi.org/10.1016/0167-2738(86)90323-1

[90] A.C. Khandkar, J.B. Wagner Jr, Fast ion transport in composites, Solid State Ionics. 18 (1986) 1100–1104. https://doi.org/10.1016/0167-2738(86)90316-4

[91] R.E. Soltis, E.M. Logothetis, A.D. Brailsford, J.B. Wagner Jr, AC Impedance Studies of AgI/Al_2O_3 Composites, J. Electrochem. Soc. 135 (1988) 2380. https://doi.org/10.1149/1.2096276

[92] H. Maekawa, R. Tanaka, T. Sato, Y. Fujimaki, T. Yamamura, Size-dependent ionic conductivity observed for ordered mesoporous alumina-LiI composite, Solid State Ionics. 175 (2004) 281–285. https://doi.org/10.1016/j.ssi.2003.12.032

[93] S. Sultana, R. Rafiuddin, Enhancement of ionic conductivity in the composite solid electrolyte system: TlI–Al_2O_3, Ionics. 15 (2009) 621–625. https://doi.org/10.1007/s11581-008-0312-2

[94] C. Wagner, The electrical conductivity of semi-conductors involving inclusions of another phase, J. Phys. Chem. Solids. 33 (1972) 1051–1059. https://doi.org/10.1016/S0022-3697(72)80265-8

[95] J. Bruce, J.B. Wagner Jr, Composite solid ion conductors, in: T. Takahashi (Ed.), High Conductivity Solid Ion Conductors Recent Trends and Application, World Scientific, 1989: pp. 146–165. https://doi.org/10.1142/9789814434294_0007

[96] X. Chen, P.M. Vereecken, Solid and Solid-Like Composite Electrolyte for Lithium Ion Batteries: Engineering the Ion Conductivity at Interfaces, Adv. Mater. Interfaces. 6 (2019) 1800899. https://doi.org/https://doi.org/10.1002/admi.201800899

[97] J. Maier, Defect chemistry and conductivity effects in heterogeneous solid electrolytes, J. Electrochem. Soc. 134 (1987) 1524. https://doi.org/10.1149/1.2100703

[98] J. Maier, Pushing nanoionics to the limits: charge carrier chemistry in extremely small systems, Chem. Mater. 26 (2014) 348–360. https://doi.org/10.1021/cm4021657

[99] J. Maier, Ionic conduction in space charge regions, Prog. Solid State Chem. 23 (1995) 171–263. https://doi.org/10.1016/0079-6786(95)00004-E

[100] E. Schreck, K. Läuger, K. Dransfeld, Enhanced ionic conductivity at the interface between sapphire and solid lithium iodide, Zeitschrift Für Phys. B Condens. Matter. 62 (1986) 331–334. https://doi.org/10.1007/BF01313455

[101] N. Sata, K. Eberman, K. Eberl, J. Maier, Mesoscopic fast ion conduction in nanometre-scale planar heterostructures, Nature. 408 (2000) 946–949. https://doi.org/10.1038/35050047

[102] X.X. Guo, J. Maier, Ionic conductivity of epitactic MBE-grown BaF_2 films, Surf. Sci. 549 (2004) 211–216. https://doi.org/10.1016/j.susc.2003.11.044

[103] X. Guo, I. Matei, J. Jamnik, J.-S. Lee, J. Maier, Defect chemical modeling of mesoscopic ion conduction in nanosized CaF_2/BaF_2 multilayer heterostructures, Phys. Rev. B. 76 (2007) 125429. https://doi.org/10.1103/PhysRevB.76.125429

[104] X. Guo, J. Maier, Ionically conducting two-dimensional heterostructures, Adv. Mater. 21 (2009) 2619–2631. https://doi.org/10.1002/adma.200900412

[105] X. Guo, J. Maier, Comprehensive modeling of ion conduction of nanosized CaF_2/BaF_2 multilayer heterostructures, Adv. Funct. Mater. 19 (2009) 96–101. https://doi.org/10.1002/adfm.200800805

[106] N.J. Dudney, Effect of Interfacial Space-Charge Polarization on the Ionic Conductivity of Composite Electrolytes, J. Am. Ceram. Soc. 68 (1985) 538–545. https://doi.org/10.1111/j.1151-2916.1985.tb11520.x

[107] J.C. Wang, N.J. Dudney, Model for the composition dependence of conductivity of an ionic conductor containing submicron particles of an insulator, Solid State Ionics. 18 (1986) 112–116. https://doi.org/10.1016/0167-2738(86)90096-2

[108] A. Bunde, W. Dieterich, E. Roman, Dispersed ionic conductors and percolation theory, Phys. Rev. Lett. 55 (1985) 5. https://doi.org/10.1103/PhysRevLett.55.5

[109] A. Bunde, W. Dieterich, E. Roman, Monte Carlo studies of ionic conductors containing an insulating second phase, Solid State Ionics. 18 (1986) 147–150. https://doi.org/10.1016/0167-2738(86)90102-5

[110] H.E. Roman, A. Bunde, W. Dieterich, Conductivity of dispersed ionic conductors: A percolation model with two critical points, Phys. Rev. B. 34 (1986) 3439. https://doi.org/10.1103/PhysRevB.34.3439

[111] H.E. Roman, M. Yussouff, Particle-size effect on the conductivity of dispersed ionic conductors, Phys. Rev. B. 36 (1987) 7285. https://doi.org/10.1103/PhysRevB.36.7285

[112] A.M. Stoneham, E. Wade, J.A. Kilner, A model for the fast ionic diffusion in alumina-doped LiI, Mater. Res. Bull. 14 (1979) 661–666. https://doi.org/10.1016/0025-5408(79)90049-7

[113] S. Fujitsu, H. Kobayashi, K. Koumoto, H. Yanagida, Enhancement of Ionic Conductivity in the $SrCl_2$-Al_2O_3 System, J. Electrochem. Soc. 133 (1986) 1497. https://doi.org/10.1149/1.2108943

[114] I.V. Belova, G.E. Murch, Calculation of the effective conductivity and diffusivity in composite solid electrolytes, J. Phys. Chem. Solids. 66 (2005) 722–728. https://doi.org/10.1016/j.jpcs.2004.09.009

[115] N.F. Uvarov, V.P. Isupov, V. Sharma, A.K. Shukla, Effect of morphology and particle size on the ionic conductivities of composite solid electrolytes, Solid State Ionics. 51 (1992) 41–52. https://doi.org/10.1016/0167-2738(92)90342-M

[116] V. Epp, M. Wilkening, Motion of Li^+ in nanoengineered $LiBH_4$ and $LiBH_4$:Al_2O_3 comparison with the microcrystalline form, ChemPhysChem. 14 (2013) 3706–3713. https://doi.org/10.1002/cphc.201300743

[117] S. Breuer, V. Pregartner, S. Lunghammer, H.M.R. Wilkening, Dispersed solid conductors: fast interfacial Li-ion dynamics in nanostructured LiF and LiF:γ-Al_2O_3 composites, J. Phys. Chem. C. 123 (2019) 5222–5230. https://doi.org/https://doi.org/10.1021/acs.jpcc.8b10978

[118] V. Gulino, M. Brighi, F. Murgia, P. Ngene, P. de Jongh, R. Černý, M. Baricco, Room-Temperature Solid-State Lithium-Ion Battery Using a $LiBH_4$–MgO Composite Electrolyte, ACS Appl. Energy Mater. 4 (2021) 1228–1236 https://doi.org/10.1021/acsaem.0c02525

[119] S. Pack, J.B. Wagner Jr, B. Owens, Electrical Conductivity of the LiI-H_2O-Al_2O_3 System, J. Electrochem. Soc. 127 (1980) 2177–2179. https://doi.org/10.1149/1.2129368

[120] R. Dupree, J.R. Howells, A. Hooper, F.W. Poulsen, NMR studies of lithium iodide based solid electrolytes, Solid State Ionics. 9 (1983) 131–133. https://doi.org/10.1016/0167-2738(83)90221-7

[121] N.J. Dudney, Enhanced Ionic Conduction in AgCl-Al_2O_3 Composites Induced by Plastic Deformation, J. Am. Ceram. Soc. 70 (1987) 65–68. https://doi.org/10.1111/j.1151-2916.1987.tb04930.x

[122] D.A. Jones, J.W. Mitchell, Observations on helical dislocations in crystals of silver chloride, Philos. Mag. 3 (1958) 1–7. ttps://doi.org/10.1080/14786435808243219

[123] A. Fick, Ueber diffusion, Ann. Phys. 170 (1855) 59–86. https://doi.org/10.1002/andp.18551700105

[124] A.R. West, Crystalline solid electrolytes I: general considerations and the major materials, in: P.G. Bruce (Ed.), Solid state electrochemistry, Cambridge University press, Oxford, UK, 1997: pp. 8-9. https://doi.org/10.1017/CBO9780511524790.003

[125] J. Crank, The mathematics of diffusion, Oxford university press, UK, 1979.

[126] J.B. Goodenough, Oxide-ion electrolytes, Annu. Rev. Mater. Res. 33 (2003) 91–128. https://doi.org/10.1146/annurev.matsci.33.022802.091651

[127] H. Mehrer, Diffusion in solids: fundamentals, methods, materials, diffusion-controlled processes, Springer Science Business Media, Berlin, Germany, 2007. https://doi.org/10.1007/978-3-540-71488-0

[128] M. V Reddy, C.M. Julien, A. Mauger, K. Zaghib, Sulfide and oxide inorganic solid electrolytes for all-solid-state Li batteries: A Review, Nanomaterials. 10 (2020) 1606. https://doi.org/10.3390/nano10081606

[129] J.T.S. Irvine, A.R. West, Crystalline lithium ion conductors, in: T. Takahashi (Ed.), High Conductivity Solid Ion Conductors Recent Trends and Application, World Scientific, 1989: pp. 201–222. https://doi.org/10.1142/9789814434294_0009

2. LAGP – LLTO composite

2.1. Introduction

This chapter introduces the conductivity enhancement method for $Li_{1.5}Al_{0.5}Ge_{1.5}(PO_4)_3$ (LAGP) solid-state composite through insulative particle dispersion technique. LAGP is a type of oxide-based solid-state electrolyte with NASICON-type crystallographic structure (space group *R*–3*c*) that is constructed by corner sharing MO_6 (M = Ge, Al) octahedra and PO_4 tetrahedra as shown in Fig 2.1. Under equilibrium state, lithium ions could occupy two possible sites: octahedral centre 6*b* site (Li1) or polyhedral centre 18*e* site (Li2), while another tetrahedral centre 36*f* site can also be occupied as a metastable bridging node during diffusion process [1,2]. Such structure allows formulation of a 6*b* → 36*f* → 18*e* → 36*f* → 6*b* diffusion pathway that stretches in 3-dimension in the NASICON lattice, which is the origin of the superionic lithium-ion conductivity for LAGP [2]. In terms of modification for LAGP compound (or $LiGe_2(PO_4)_3$ in general), research efforts are mainly focused on i) engineering of the lattice structure of LAGP, ii) increasing the lithium-ion concentration within lattice, or iii) improving the recrystallisation of LAGP during sintering to improve the densification [3–8]. Li_2O additives or excessive lithium addition in starting materials have also been proven effective in alleviating the poor grain boundary conductivity in LAGP [9,10], which achieves good room-temperature conductivity improvement for LAGP [11,12].

As a new type of modification technique that is different from the aliovalent doping or grain boundary enhancement, the insulative particle dispersion methods have been explored in oxide-based solid-state conductors in recent years [13–16]. In previous work, $LaPO_4$ particles were dispersed in $Li_{1.3}Al_{0.3}Ti_{1.7}(PO_4)_3$ (LATP) matrix through co-sintering LATP precursor with 4 wt.% $Li_{0.348}La_{0.55}TiO_3$ (LLTO) powder, which resulted in 3-fold improvement in conductivity [16]. Although $LaPO_4$ particle was formed in the resulted samples instead of LLTO, directly incorporating $LaPO_4$ into LATP matrix failed to produce similar effect [17]. Therefore, these types of the samples are denoted as LATP – LLTO composite electrolytes to emphasise the materials originally employed before sintering. As introduced in Chapter 1, the insulative particle dispersion technique was mostly employed in halide-based solid-state electrolytes [18–25], upon which the space charge layer model was developed to explain the conductivity enhancement observed in these systems [25–27]. At the lithium-ion conductor / insulator particle interface (also referred to as hetero-interface in some works), the equilibrium defect concentration at local is

altered under the effect of chemical potential from the insulator phase, such that a space charge layer with a relatively high lithium-ion mobility can be formed [26,27]. The existence of space charge layer at the hetero-interfaces in composite electrolytes have been convincingly identified from extra rapid lithium-ion migration mechanism in composite electrolytes using solid-state ^{7}Li nuclear magnetic resonance (NMR) experiments in other works [28–31]. It is therefore believed that space charge layer is also formed at the LATP matrix / $LaPO_4$ particle interface in the previously reported LATP – LLTO composite.

One main shortcoming of employing LATP as the matrix of composite electrolyte is that owing to the multivalence of the titanium ion, LATP can be vulnerable to reduction reactions as the $LaPO_4$ particles are formed by LLTO decomposition during the sintering process [32]. This might introduce electronic defects into the ionic conductor that lead to reduced transport number. Dispersing insulative $LaPO_4$ particles in LAGP matrix instead of LATP would not only replicate the conductivity enhancement mechanism, but also yield composite electrolytes with higher electrochemical stability. Therefore, in this work, LLTO particles are mixed with LAGP precursors before sintering to form $LaPO_4$ dispersants within the LAGP matrix through solid-state reactions between LLTO and LAGP during sintering. The phase composition, microstructure, evolution in electrical conductivity as functions of LLTO addition are investigated.

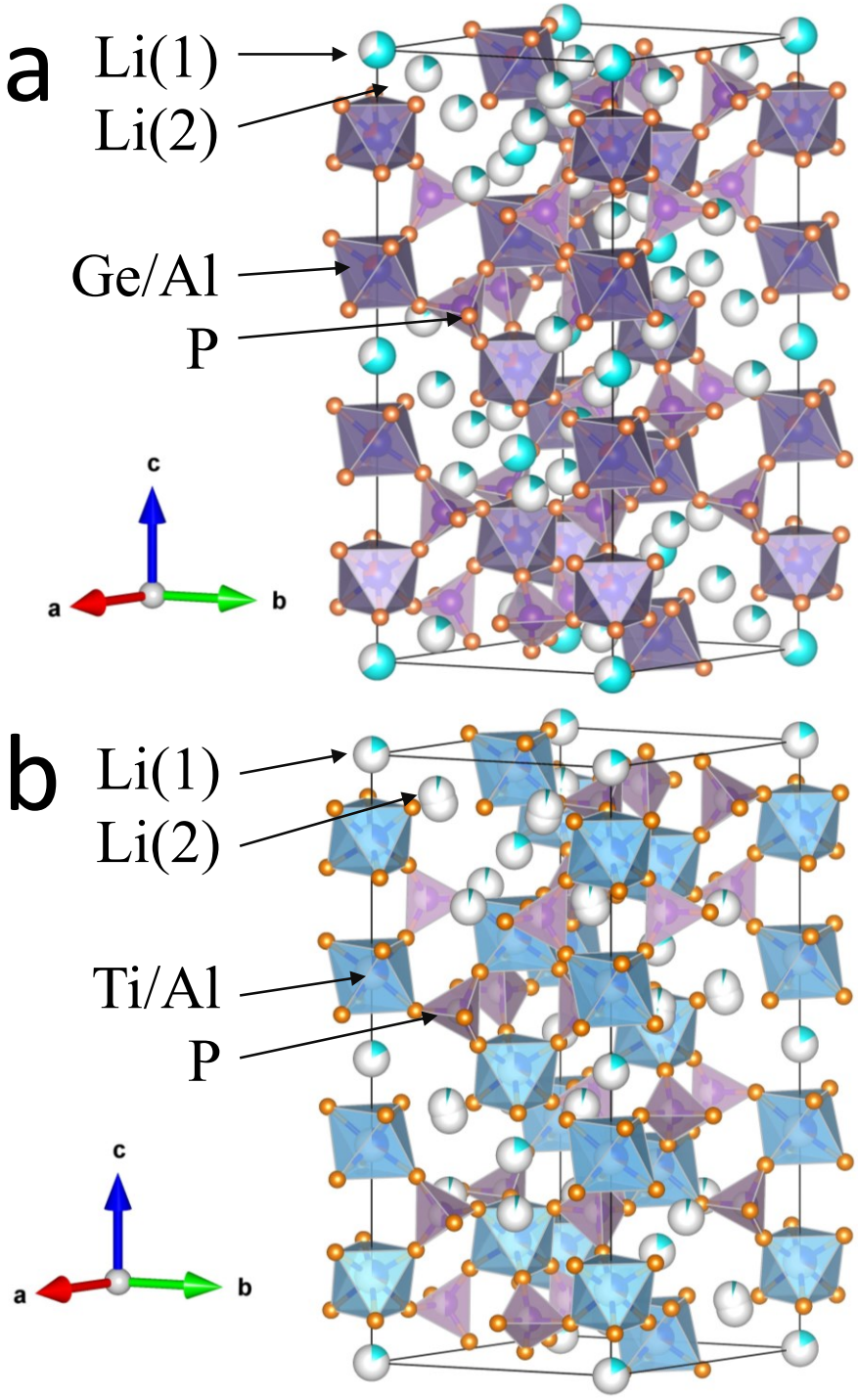

Figure 2.1 Drawings of crystal lattice of (a) LAGP and (b) LATP, according to the structural refinement data from ref [33] and ref [34].

2.2. Experiments

2.2.1. Synthesis of LLTO powder

$Li_{0.348}La_{0.55}TiO_3$ (LLTO) was synthesised by solid-state reaction method. Stoichiometric amount of $LiCO_3$ (99% Wako Pure Chem., Japan), La_2O_3 (99.99% Wako Pure Chem.) and TiO_2 (99.9% Wako Pure Chem., anatase) were weighed on an electronic balance and mixed by hand in alumina mortar and pestle briefly. Extra Li_2CO_3 (10 wt.%) was added into the mixture to compensate the lithium loss during subsequent heat-treatments. The mixture was then transferred into in another alumina mortar on the automatic grinder (ANM1000, Nitto Kagaku, Japan) with an aid of ethanol (99.0% Wako Pure Chem.) for a further 5 h grinding to ensure a thorough mixing of starting materials, during which a ring-shaped transparent plastic sheet was used to cover the mortar, and ethanol was replenished every 15-20 min. After mixing, the mixture was dried in air in a 60 °C-drying oven overnight, then recovered into a glass bottle for further drying at 120 °C in vacuum to remove residual ethanol and moisture from the mixture.

After drying, 2-3 g of the mixture powder was weighed and uniaxially pressed into a green pellet with a ϕ22 mm die by hand, which was then calcined in an alumina crucible at 800 °C for 10 h (detailed heat-treatment conditions are listed in Table 2.1). The calcined product was then crushed in an alumina mortar by hand to form precursor powder, which is then uniaxially pressed with a ϕ7 mm die by hand and sealed in rubber probe covers using vacuum pump. The seals were then cold-isostatically pressed at 100 MPa for 3 min to form pellets (Dr. CIP, KOBELCO, Japan).

The iso-pressed pellets were sintered in an alumina crucible at 1300 °C for 10 h to be fully densified, the detail of the heat-treatment is listed in Table 2.2. The sintered pellets were then crushed in an alumina mortar by hand to form LLTO powder for further synthesis.

Table 2.1 Heat-treatment conditions for LLTO calcination.

heating rate	5 °C/min
calcinating temperature	800 °C
calcinating time	10 h
cooling rate	5 °C/min
crucible	Al_2O_3
heat-treat atmosphere	air

Table 2.2 Heat-treatment conditions for LLTO sintering.

heating rate	5 °C/min
sintering temperature	1300 °C
sintering time	10 h
cooling rate	5 °C/min
crucible	Al_2O_3
heat-treat atmosphere	air

2.2.2. Synthesis of LAGP precursor

The starting materials of LAGP: Li_2CO_3 (99% Wako Pure Chem., with 10 wt.% excess), γ-Al_2O_3 (97% Stream Chemical, USA), GeO_2 (99.99% Nacalai Tesque, Japan) and $NH_4H_2PO_4$ (99% Wako Pure Chem.) were mixed in alumina mortar and alumina pestle by hand, then transferred into another alumina mortar coupled with ethanol for further mixing by automatic grinder for 5 h (ANM1000, Nitto Kagaku). A ring-shaped transparent plastic sheet was applied to fully cover the top of the mortar during the mixing to prevent introduction of impurities, with ethanol (99.0% Wako Pure Chem) replenished every 15-20 min. The mixture was dried at 60 °C for overnight then at 120 °C in vacuum for 24 h to remove moisture and residual ethanol. The dried powder was then weighed by 2-3 g and uniaxially pressed in a ϕ22 mm die by hand to form green compact. The green compact was placed on a platinum foil in an alumina crucible and fired at 450 °C for 20 h, the detailed heat-treatment condition is shown in Table 2.3. To produce fine precursor, the heat-treatment product was crushed in an alumina mortar by hand, then ball-milled in zirconia pot with zirconia balls and ethanol at 400 RPM for 5 h (Pulverisette7 premium line, Fritsch, Germany, detailed condition is shown in Table 2.4). The ball-milled product was then recovered and dried at 120 °C vacuum for 24 to remove moisture and ethanol.

2.2.3. Fabrication of pristine LAGP and LAGP – LLTO composite samples

To form pristine LAGP pellets, the fine precursor was weighed and uniaxially pressed into pellets by hand using a ϕ7 mm die, which were then sealed in rubber probe covers by a vacuum pump and isostatically pressed at 200 MPa for 3 min (Dr. CIP, KOBELCO). The isostatically pressed pellets were placed in an alumina crucible to be sintered at 800 °C for 10 h, the detailed sintering condition is shown in Table 2.5. To prevent reaction between the pellets and the crucible and reduce lithium loss during sintering, the pellets were embedded in the LAGP precursor powder, and isolated from the crucible surface using a platinum foil.

To form LAGP – LLTO composite pellets, the fine LAGP precursor and LLTO powder were weighed and mixed by ball-milling at 400 RPM for 1.5 h with an aid of ethanol (99.0% Wako Pure Chem.) to achieve thorough mixture (Pulverisette7 premium line, Fritsch, detailed conditions are shown in Table 2.6). The powder was then dried in 120 °C vacuum for 24 h before uniaxial pressing using a ϕ7 mm die and isostatic pressing at 200 MPa for 3 min (Dr. CIP, KOBELCO). The pellets were embedded in LAGP – LLTO mixture powder and isolated by a platinum foil during sintering at conditions listed in Table 2.5. Composite samples with 2,4, 6, 8 and 20 wt.% of LLTO addition were prepared.

Table 2.3 Heat-treatment conditions for LAGP calcination.

heating rate	5 °C/min
calcinating temperature	450 °C
calcinating time	20 h
cooling rate	5 °C/min
crucible	Al_2O_3 with a Pt foil
heat-treat atmosphere	air

Table 2.4 Ball-milling conditions for fine LAGP precursor formation.

pot and balls	zirconia (Fritsch)
ball size	ϕ5 mm
mass ratio (ball:sample)	10:1
ball-mill stage	Pulverisette7 premium line, Fritsch
duration	60 min
rest interval	60 min
cycles (total ball-milling time)	5 (5 h in total)
ball-mill media	ethanol (99.0% Wako Pure Chem)

Table 2.5 Heat-treatment conditions for LAGP and LAGP - LLTO composite sintering.

heating rate	5 °C/min
sintering temperature	800 °C
sintering time	10 h
cooling rate	5 °C/min
crucible	Al_2O_3 with a Pt foil
heat-treat atmosphere	air

Table 2.6 Ball-milling conditions for LAGP precursor – LLTO powder mixture fabrication.

pot and balls	zirconia (Fritsch)
ball size	ϕ5 mm
mass ratio (ball:sample)	10:1
ball-mill stage	Pulverisette7 premium line, Fritsch
duration	30 min
rest interval	30 min
cycles (total ball-milling time)	3 (1.5 h in total)
ball-mill media	ethanol (99.0% Wako Pure Chem)

2.2.4. Characterisations

To investigate the phase composition of pristine LAGP and LAGP – LLTO composite, the sintered pellets were crushed by alumina mortar and pestle to be loaded onto glass holders for powder X-ray diffraction (XRD) characterisations, which were carried out on an Ultima VI diffractometer (Rigaku, Japan) using a CuKα radiation source (40 kV, 40 mA). The detailed powder XRD characterisation conditions are listed in Table 2.7. For microstructural investigation, the samples were polished with up to #3000 grid abrasive paper and observed under a field emission scanning electron microscopy (FE-SEM, SU-6600, Hitachi, Japan) operating at 20 mA and 20 kV. Back-scattered electron images of the samples were taken without gold-sputtering to observe the particle distribution in the composite samples. The particle size distribution of the LLTO powder was evaluated by the dynamic light scattering (DLS) measurement. Small amount of LLTO powder was suspended in the deionised water and loaded in the glass sample tube for DLS characterisation under 100 times repeated scattering mode.

For electrochemical impedance spectroscopy (EIS) investigation, the sample pellets were polished on two surfaces with up to #3000 grid abrasive paper to obtain mirror reflection finish, then sputtered with gold using a magnetron plasma sputter (MSP-Mini Magnetron Sputter, Vacuum Device, Japan) to form lithium-blocking electrodes. The prepared pellets were then clamped in a 4-electrode cell which is placed in a tubular furnace for temperature control. The 4-electrode cell was connected with an LRC metre (3531 Z Hitester, Hioki, Japan) in a 4-electrode symmetric setup to control the input perturbation and record the impedance response. The temperature of the tubular furnace was controlled by a temperature controller with a type-K thermocouple (AGC-S, Asahi Rika, Japan). The impedance data were collected in a frequency range of 130 Hz - 1.3 MHz under a temperature range of 25 – 200 °C to measure the temperature dependence of the sample conductivity (i.e., Arrhenius behaviours). During the temperature control process, the pellets are kept at target temperature ± 0.5 °C for over 10 minutes before EIS measurement to reduce the impact from the temperature fluctuation of the samples.

Table 2.7 Specifications of X-ray diffractometer and powder XRD.

diffractometer	Ultima VI, Rigaku
scanning speed	2˚/min
2θ step	0.04˚
2θ range	10˚ - 50˚
x-ray generator (wavelength)	copper Kα (0.154 nm)
voltage and current	40 kV, 40 mA

2.3. Phase Composition

This section focuses on the phase composition of the LAGP – LLTO, which involves assession of the phase stability of NASICON structure and identification of secondary phase and impurity phases after sintering using powder XRD characterisation technique. Basing on the characterisation results, further experiments were carried out to investigate the roles of the secondary phases in the solid-state reactions during the sintering, which is also discussed in this section.

The phase compositions of the pristine LAGP and LAGP – *x* wt.% LLTO investigated by X-ray diffraction pattern are shown in Fig 2.2 (a). The major peaks are in good agreement with the structure of $LiGe_2(PO_4)_3$ (LGP), which is isostructural with LAGP. The peaks at 20.4˚, 25.92˚ and 30.84˚ in the XRD of pristine LAGP are ascribed to GeO_2 which is commonly formed in the course of LAGP sintering [35,36]. Peaks of the introduced LLTO are completely absent in the patterns of composite samples, while that of $LaPO_4$ (labelled by diamond symbol) appeared and increased with nominal LLTO addition. This phenomenon is similar to the previous works by Onishi *et al*., where the LLTO introduced to LATP decomposed and formed $LaPO_4$ phase after sintering [16,17]. During the sintering process, the introduced LLTO reacted with LAGP by donating La^{3+} ions and combined with PO_4^{3-} from the LAGP matrix to form $LaPO_4$ phase. The decomposition of introduced LLTO, plus the similarities in the crystal structures of LAGP and LATP (shown in Fig 2.1), also facilitates the substitution of Ge^{4+} ion in LAGP by the Ti^{4+} from the LLTO. This leads to increased GeO_2 precipitation from the LAGP and formation of $Li_{1+x}Al_xTi_yGe_{2-x-y}(PO_4)_3$ (LAGTP)-like solid solutions, which is also reported by other researchers [4]. The incorporation of larger ion Ti^{4+} (74.5 p.m. of radius in a 6-coordination position in comparison to 64 p.m. for Ge^{4+}) into the LAGP lattice can give rise to lattice expansion, which contributes to the peak-shift towards smaller angles as observed in Fig 2.2 (b). At 8 wt.% of LLTO addition, the peak shift towards $LiTi_2(PO_4)_3$ structure becomes most significant, indicating a significant LAGTP-like solid solution formation.

GeO_2 and $LaPO_4$, as secondary phases on the XRD patterns, were also mixed with LAGP and co-sintered, the mass ratio of which being based on the assumption that all LLTO (4 wt.%) decomposed to form $LaPO_4$ or reacted to substitute Ge^{4+} in the LAGP lattice to precipitate GeO_2. As shown in Fig 2.3, in case where $LaPO_4$ was directly dispersed in LAGP, the peaks are similar to that of LAGP – 4 wt.% LLTO composites. The peak intensity of directly introduced $LaPO_4$ is

higher than that formed by LLTO decomposition, this might be explained by the orientation preference of $LaPO_4$ formed by LLTO/LAGP reaction, which gives lower peak intensities. Another possible reason is that the LLTO in the LAGP – 4 wt.% LLTO was not fully converted to $LaPO_4$ during sintering. However, no residual LLTO peak or extra impurity peak can be observed on the LAGP – 4 wt.% LLTO patterns in comparison to LAGP – $LaPO_4$ sample, which concludes that this hypothesis could be less plausible. For the LAGP – GeO_2 sample, the peak positions and intensity are in reasonable agreements with the LAGP – 4 wt.% LLTO composites.

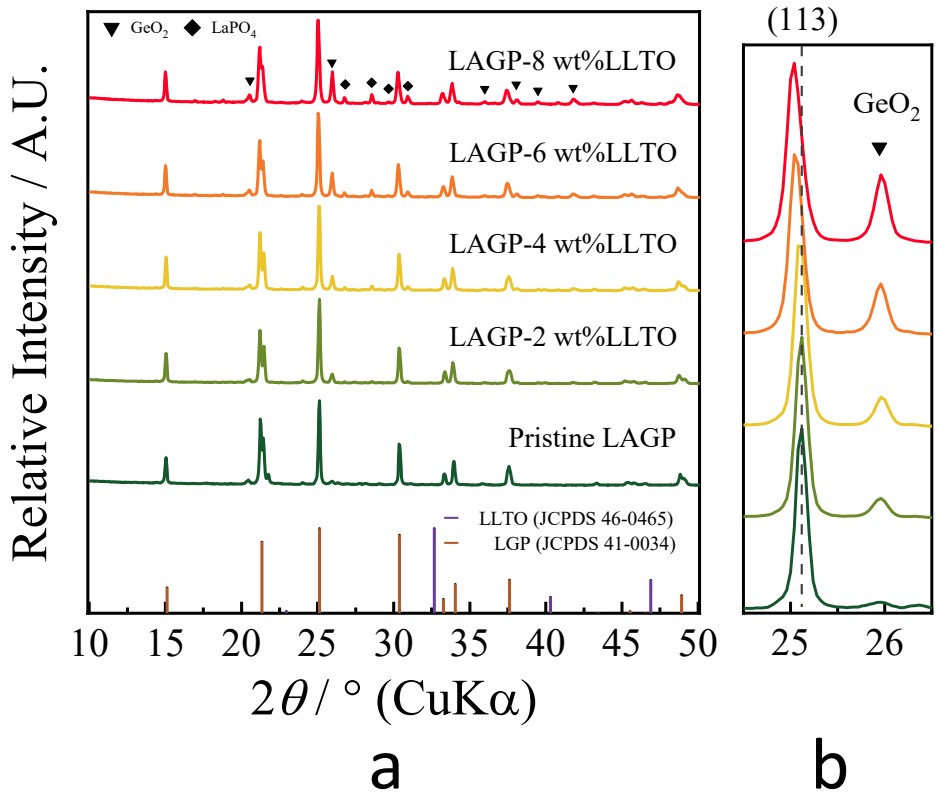

Figure 2.2 (a) Powder XRD patterns of pristine LAGP and LAGP – *x* wt.% LLTO composites with *x* = 2, 4, 6, and 8, peaks in addition to that from LGP lattice structure are identified as GeO_2 (invert triangle) and $LaPO_4$ (diamond) . (b) Zoom-in XRD pattern on angle range 24 to 27˚.

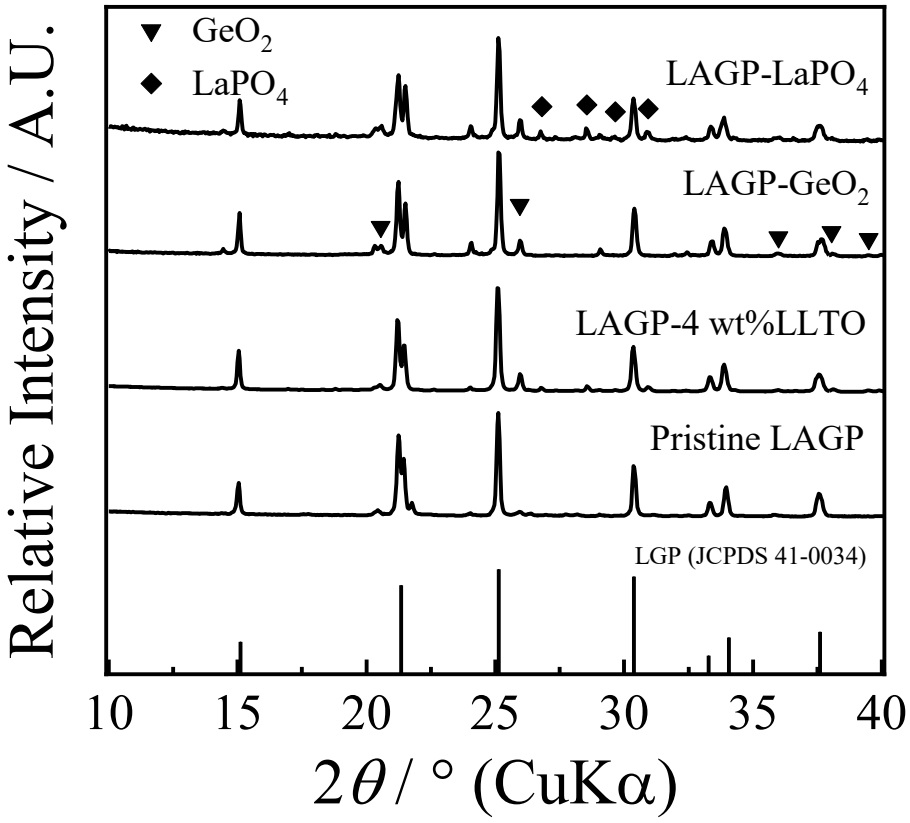

Figure 2.3 Powder XRD pattern of pristine LAGP, LAGP – 4 wt.% LLTO, LAGP – GeO_2, and LAGP – $LaPO_4$ composites. The amounts of GeO_2 or $LaPO_4$ were decided by assuming all Ti^{4+} in the introduced 4 wt.% LLTO substituted Ti^{4+} in LAGP to precipitate GeO_2, or all La^{3+} are converted to $LaPO_4$.

2.4. Microstructural Analysis

In this section, the microstructures of the LAGP – LLTO composites are investigated using SEM to discuss the size and distribution of the $LaPO_4$ particles. The sizes of the dispersed particles before and after sintering are also compared based on SEM images and results from DLS spectrum. Two techniques of incorporating $LaPO_4$ particles in LAGP matrix are investigated and discussed in terms of the particle morphology: i) *in-situ* formation of $LaPO_4$ through LLTO decomposition during LAGP – LLTO co-sintering, and ii) direct dispersion of $LaPO_4$ through LAGP – $LaPO_4$•H_2O co-sintering.

Fig 2.4 shows the back-scattered SEM images of pristine LAGP, LAGP – *x* wt.% LLTO composites and LAGP – $LaPO_4$ composite. For all samples, bright particles and dark areas can be observed on the back-scattered images. Although owing to the particle size and resolution of EDX detector of the FE-SEM, it is challenging to investigate the exact chemical composition of the particles, the bright particles can be identified as La^{3+}-containing $LaPO_4$ phase as the heavy lanthanum element scattered more electrons than other elements in the LAGP – LLTO composite. At 2 and 4 wt.% of LLTO addition (Fig 2.4 (b) and (c)), the particles are scattered across the microstructure in isolated form, with particle sizes ranging from few hundred nm to 1 μm. The size distribution of the particles is significantly lower than the initially introduced particle size of the LLTO powder which is introduced in the following paragraph. This further suggests that the observed lanthanum containing particles are formed by the decomposition of LLTO powder as the LLTO reacted with LAGP matrix during sintering. As observed in LAGP – 8 wt.% LLTO sample (Fig 2.4 (d), the size and connectivity of the particles are also increased with the LLTO addition, forming particle clusters. At 20 wt.% of LLTO addition, interconnecting bright areas can be observed in Fig 2.4 (e) as a result of severe particle aggregation, which breaks the continuity of the matrix.

To study the relationship between the introduced LLTO particles and the $LaPO_4$ particles formed through solid-state reaction between LLTO and LAGP matrix during the co-sintering, the size distribution of the LLTO particle was investigated through DLS method, the result of which shown in Fig 2.5. The LLTO particles formed by crushing in alumina mortar have diameters ranging from 900 to 3000 nm, with an average of approximately 2500 nm, which is larger than the $LaPO_4$ particles observed in Fig 2.4 (b) and (c). Due to the solid-state reaction with LAGP matrix during the co-sintering, the LLTO particles underwent decomposition which forms

fine $LaPO_4$ particles with smaller sizes. For comparison, Fig 2.6 exhibits the back-scattered SEM images of samples prepared co-sintering LAGP precursor with 3.17 wt.% $LaPO_4 \cdot H_2O$ reagent, which contains the same amount of lanthanum as LAGP – 4 wt.% LLTO. The observed $LaPO_4$ particles are in polygonal shape and are significantly larger than that of LAGP – 4 wt.% LLTO in Fig 2.4 (c). Both features lead to less LAGP matrix / $LaPO_4$ particle interface that are available for the space charge layer formation, the impact of which will be discussed in following section.

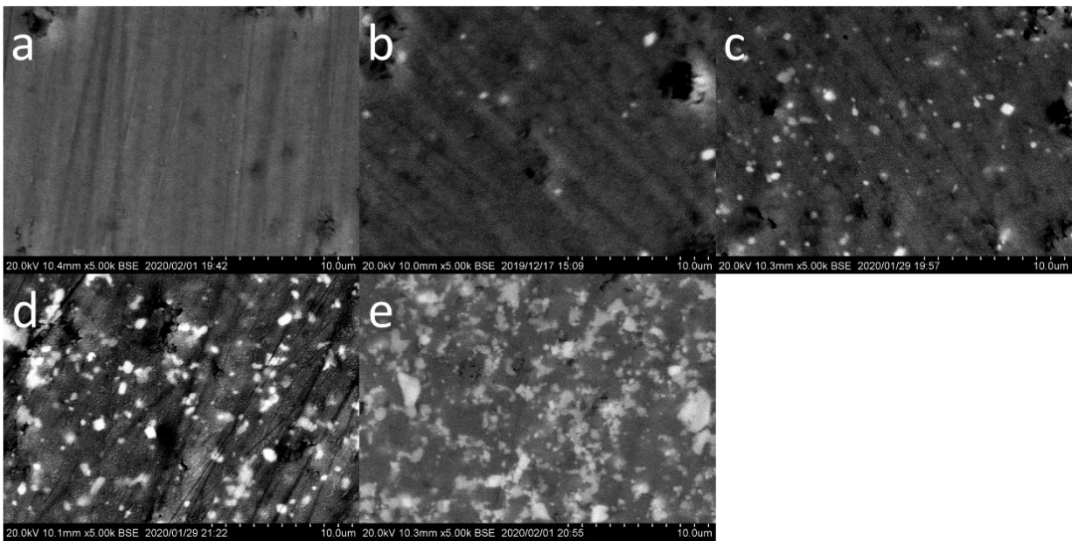

Figure 2.4 Back-scattered SEM images of (a) pristine LAGP, (b) LAGP – 2 wt.% LLTO, (c) LAGP – 4 wt.% LLTO, (d) LAGP – 6 wt.% LLTO and, (e) LAGP – 20 wt.% LLTO composites.

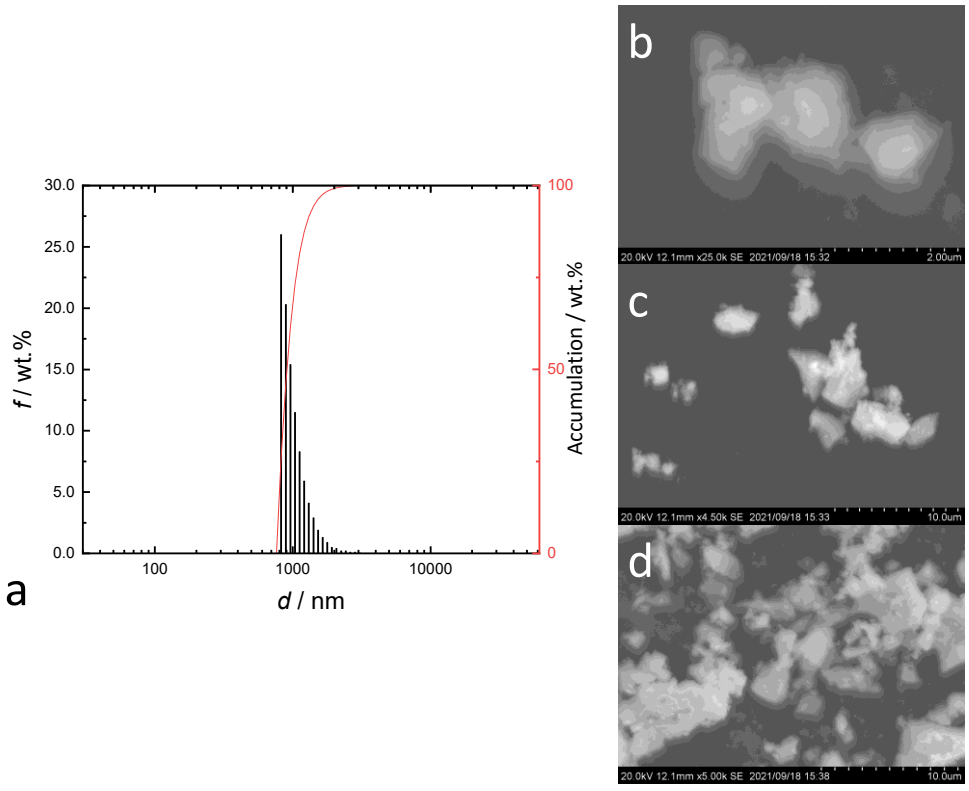

Figure 2.5 (a) Particle size distribution by weight percentages measured from DLS on LLTO particles suspended in deionised water. (b)-(d) Secondary electron SEM images of LLTO particles.

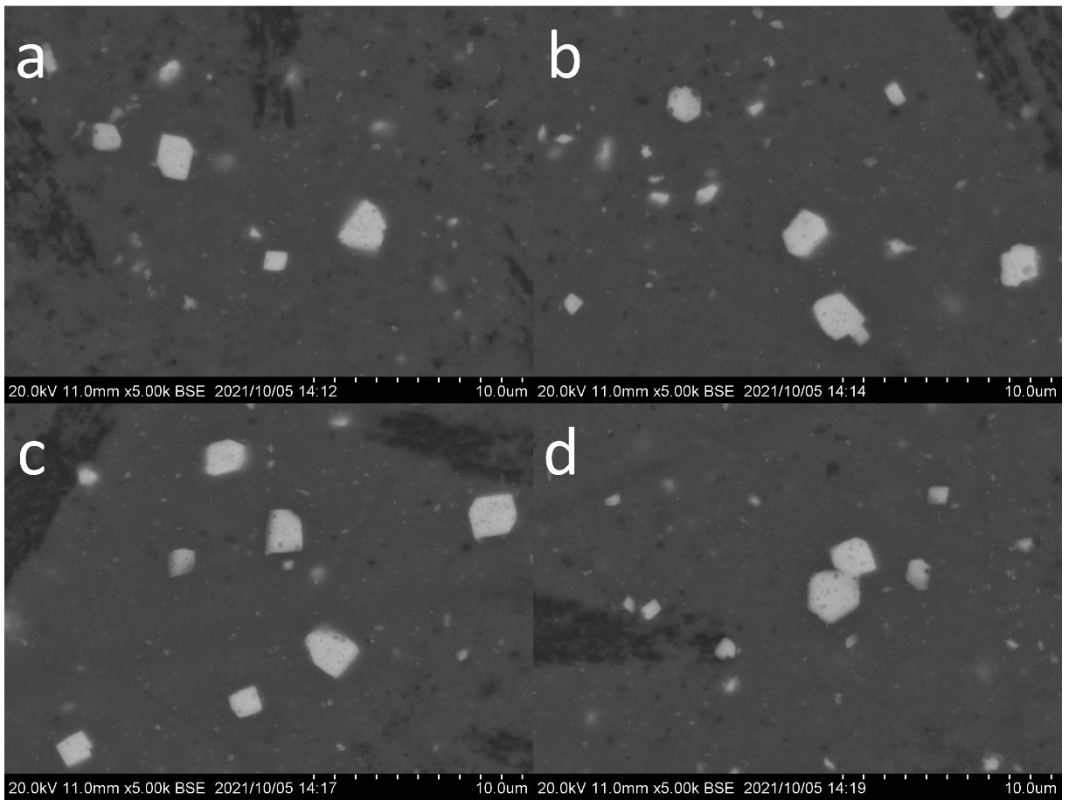

Figure 2.6 Back-scattered SEM images of LAGP – 3.17 wt.% $LaPO_4 \cdot H_2O$ sample. Bright $LaPO_4$ particles are embedded in dark LAGP matrix.

2.5. Electrochemical Analysis

This section assesses the electrochemical property of the LAGP – LLTO composites. The electrical conductivities and related activation energies are interpretated from the EIS spectra, while the ionic and electronic conductivity are qualitatively studied by the potentiostatic analysis. LAGP – GeO_2 and LAGP – $LaPO_4$ composites are also reviewed to investigate the roles of secondary phases and $LaPO_4$ particle incorporation methods on the conductivity performance of the composites.

The electrochemical impedance spectra of pristine LAGP and LAGP – *x* wt.% LLTO composites measured at 25 °C are presented in Fig 2.7. Owing to the detection range of the LRC meter, the low-frequency part of the semi-circles, which is believed to be representing total resistivity of the samples, can be observed on the EIS spectra. Therefore, the impedance spectra are fitted by the equivalent circuit shown in the inset of Fig 2.7 to calculate the total resistance (interception at around 29.1 kHz) and hence total conductivity of the samples, which is represented by R1. The low frequency parts of the spectra are represented by the R2//CPE2, to fit the semicircle respond which is believed to be generated by the lithium-blocking gold electrodes.

The conductivities of the cylindrical samples are calculated by the equation:

$$\sigma = \frac{t}{A \cdot R} = \frac{t}{\pi \frac{D^2}{4} \cdot R} \qquad (2.1)$$

where σ is the conductivity (S/cm), t is the thickness of the cylindrical sample (cm), A is the area of the circular surface of the cylindrical sample (cm^2), R is the resistance measured by the equivalent circuit fitting (Ω), D is the diameter of the circular surface (cm). The room temperature conductivities of the samples are listed in Table 2.8 and plotted in Fig 2.8 as a function of LLTO addition. The conductivity is increased with LLTO addition from 0 to 4 wt.% and decreased at LLTO introductions higher than 4 wt.%, which is similar to the LATP – *x* wt.% LLTO composite in the previous work, as well as other halide-based composite lithium-ion conductors [16,18,26,27]. The increase in conductivity can be attributed by the formation of the space charge layer at the LAGP / $LaPO_4$ interface, which increases the lithium mobility at local and hence the total conductivity as the amount of interface increases with the introduction of the LLTO. Although the formation of an LAGTP-like solid solution can be another possible explanation, as reported by Ling *et al*., the LAGTP solid solution with the highest electrical conductivity is formed in the LAGP – 20 wt.% LATP binary system [37]. However, the LAGTP solid solution

with 4 wt.% LLTO in this work is equivalent to that of the LAGP – 5.2 wt.% LATP system (assuming all the Ti^{4+} from LLTO substitutes the Ge^{4+}). If the major reason for the increase in conductivity is due to the formation of LAGTP, the highest conductivity should occur at high LLTO contents.

With the increased LLTO introduction, the aggregation of the $LaPO_4$ particles is also increased, which forms insulative particle clusters that can impede the migration of the lithium ions. After 4 wt.%, this effect suppresses the conductivity enhancement offered by the space charge layer at the LAGP / $LaPO_4$ interface and starts to reduce the conductivity. At 20 wt.% of LLTO addition, the severe $LaPO_4$ particle aggregation forms interconnecting $LaPO_4$ areas (as observed in the SEM images in Fig 2.4 (e)) which breaks the continuity of the LAGP matrix and heavily limits the conductivity. The room temperature conductivity results and corresponding EIS Nyquist plots of LAGP composites introduced with GeO_2 and $LaPO_4$ are also shown in Figs 2.8 and 2.9. These results demonstrate that i) the GeO_2 as an impurity phase observed in powder XRD pattern in Fig 2.2 does not contribute to the enhancement in conductivity, and ii) the LAGP / $LaPO_4$ interface formed by directly co-sintering of LAGP with $LaPO_4$ is not effective for space charge layer formation, this might suggest that it is necessary to form $LaPO_4$ particles in LAGP through reaction. As discussed in section 2.4, the $LaPO_4$ particles formed by LLTO decomposition is also smaller in size in comparison to the directly incorporated $LaPO_4$, which could increase the total area of space charge layer at the LAGP / $LaPO_4$ interface as well as facilitating distribution of $LaPO_4$ particles. Furthermore, it is believed that the reaction between LAGP and a lanthanum doner can create an intimate contact between LAGP and $LaPO_4$ particle, which is vital for the formation of space charge layer.

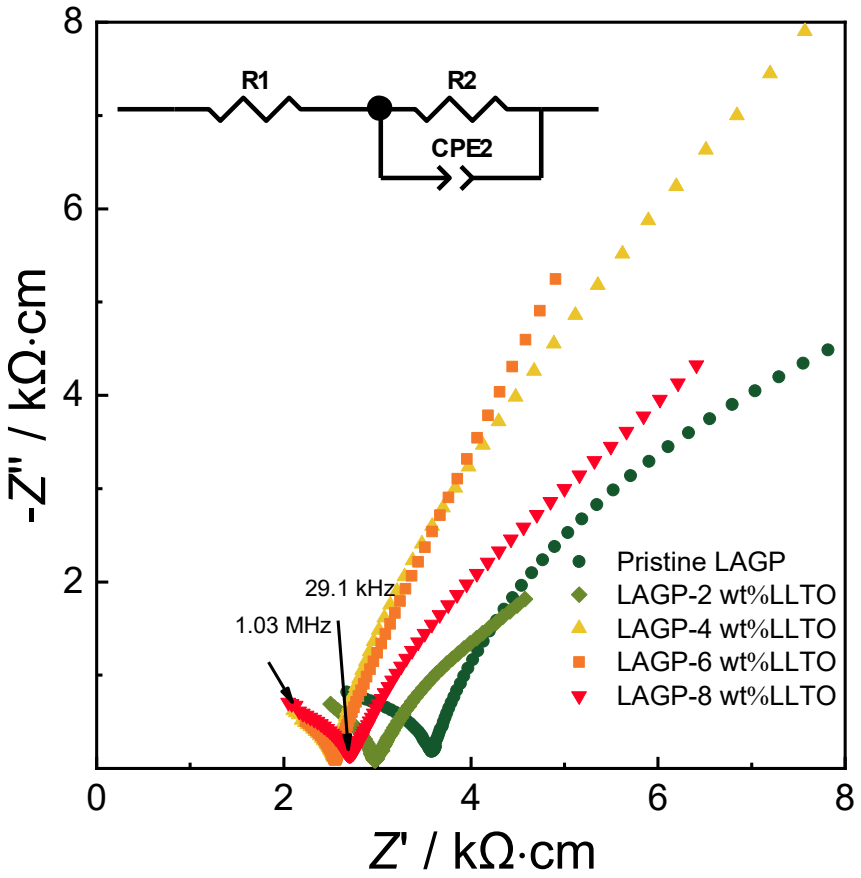

Figure 2.7 Normalised Nyquist plot of electrochemical impedance for pristine LAGP samples and LAGP – *x* wt.% LLTO samples measured at 25 °C.

Table 2.8 Room temperature conductivity and activation energy of LAGP – *x* wt.% LLTO, LAGP – GeO_2 and LAGP – $LaPO_4$ composites.

LLTO addition (wt.%)	σ (mS·cm^{-1})	E_a (eV)
0	0.2881	0.3769
2	0.3444	0.3629
4	0.4043	0.3635
6	0.4015	0.3658
8	0.3765	0.3622
20	0.1218	0.3528
LAGP – GeO_2	0.2600	--
LAGP – $LaPO_4$	0.1450	--

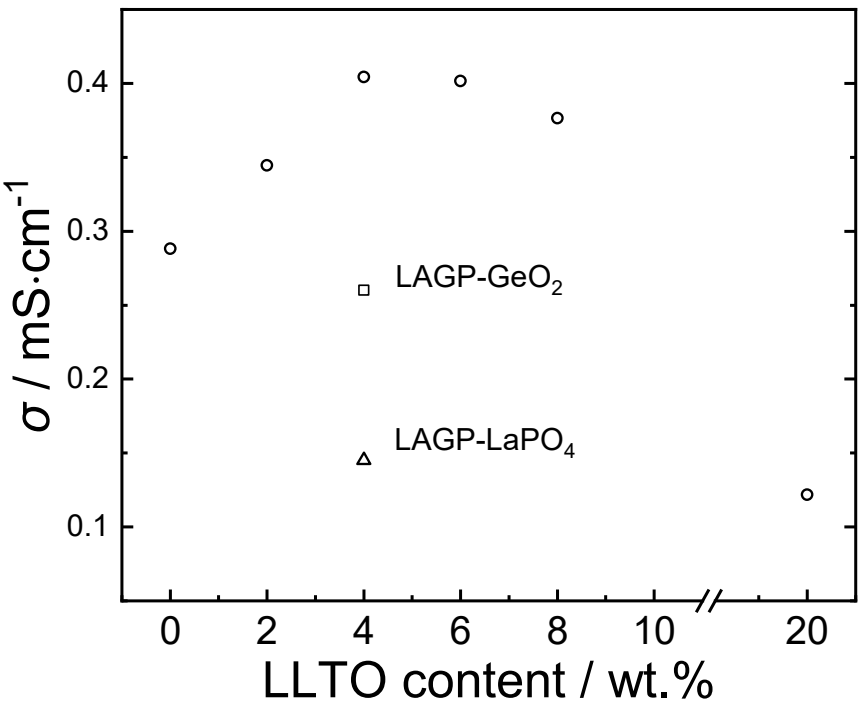

Figure 2.8 Conductivity of LAGP – LLTO composite at 25 °C as a function of LLTO addition (open circle). The open square and open triangle stands for LAGP – GeO_2 and LAGP – $LaPO_4$ composites respectively.

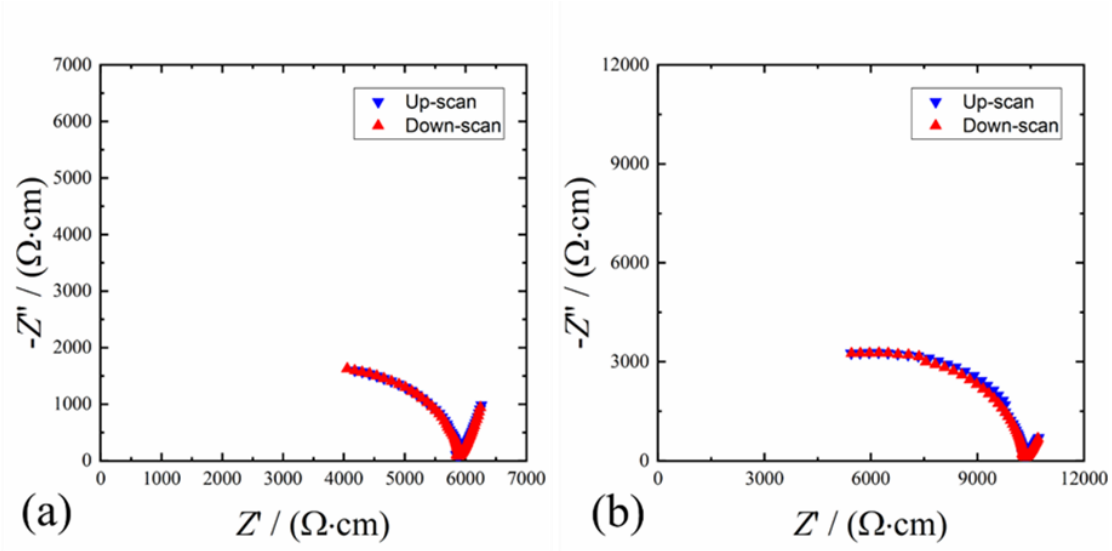

Figure 2.9 Nyquist plots of (a) GeO_2 and (b) $LaPO_4$ - dispersed LAGP samples measured at 25 °C, represented by open circle and open square respectively. Down-scan stands for frequency sweeping from 1.3 MHz to 130 Hz and up-scan the opposite.

EIS tests were also conducted at 50 to 200 °C to investigate the temperature dependence of conductivity for pristine LAGP and LAGP – LLTO composites, the results of which are shown in the Arrhenius plots in Fig 2.10. The temperature dependence behaviours are linear for all the samples, which suggests that the lithium-ion migration mechanism for an LAGP – *x* wt.% remains unchanged within the temperature range 25 - 200 °C. The data points can be fitted linearly according to the Arrhenius equation:

$$T\sigma_T = \sigma_0 \exp\left(\frac{-E_a}{kT}\right) \qquad (2.2)$$

where σ_T is the total conductivity (S/cm), σ_0 is the exponential term (S/cm), E_a is the activation energy (J), k is the Boltzmann constant (J/K), and T is temperature (K). The activation energies of the samples can be obtained from the slopes of the linear fitting to the data points, which are listed in Table 2.8 and plotted in Fig 2.11 as a function of LLTO introduction. The activation energy is slightly decreased upon introduction of LLTO, which is also reported in other works [38–40]. While this might be attributed to the formation of defects accompanying the introduction of secondary phase, this suggests that the lithium-ion migration mechanism from the LAGP matrix remains to be the main contribution to the LAGP – LLTO system, and requires further studies for elaborations. It is speculated that as the matrix / particle phase boundary forms, the particles act as an assembly of point defects, leading to the facilitated migration of lithium ions at these boundaries and hence the decrease of the overall activation energy.

To further confirm the charge carrier in the composite sample, the LAGP – 4 wt.% LLTO sample was assembled in an asymmetric cell using lithium foil and stainless steel as two electrodes (Li foil | LAGP 4 wt.% LLTO | stainless steel) and carried out potentiostatic tests by polarising Li foil and stainless steel as anodes respectively. Current through the cell was monitored while applying 0.5 V DC potential. From Fig 2.12, it can be observed that when the lithium-ion-blocking stainless steel was polarised as anode, the current was significantly suppressed, indicating a limited electronic conductivity and lithium ion being a major charge carrier in the composite sample.

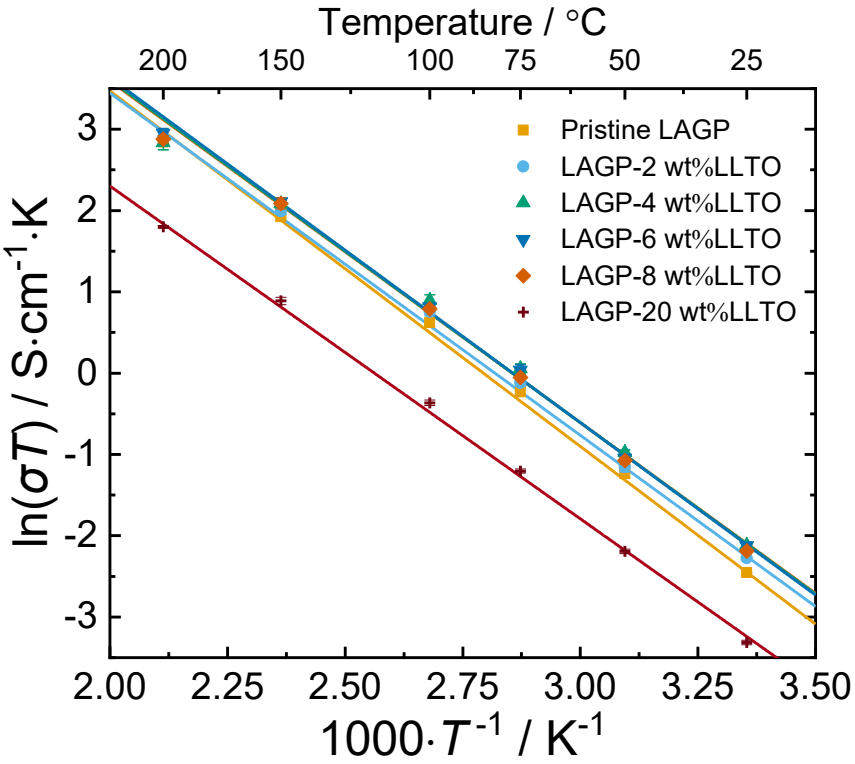

Figure 2.10 Arrhenius plots of pristine LAGP and LAGP – *x* wt.% LLTO samples within temperature range 25 - 200 °C.

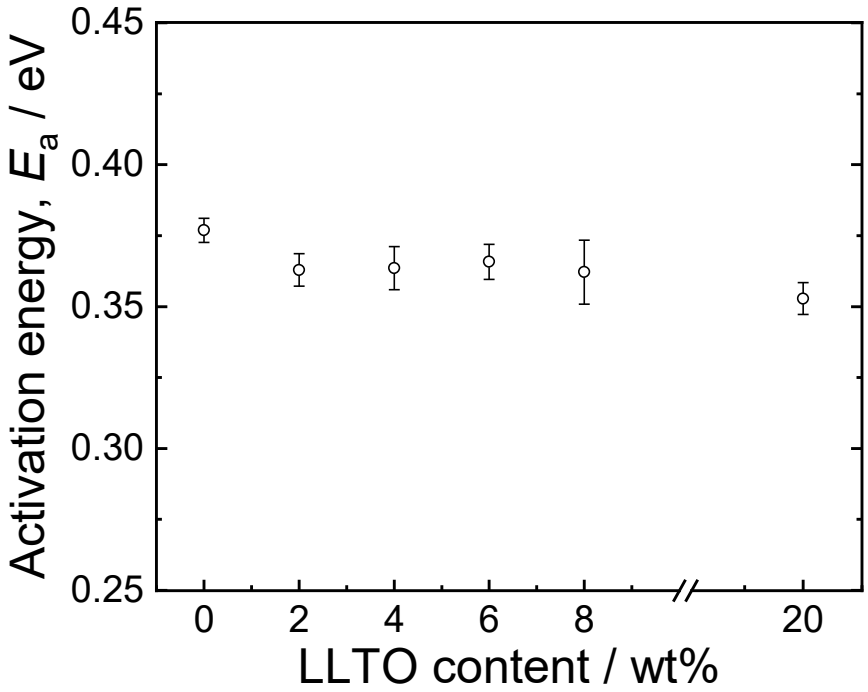

Figure 2.11 Activation energy of pristine LAGP and LAGP – *x* wt.% LLTO samples as a function of LLTO addition.

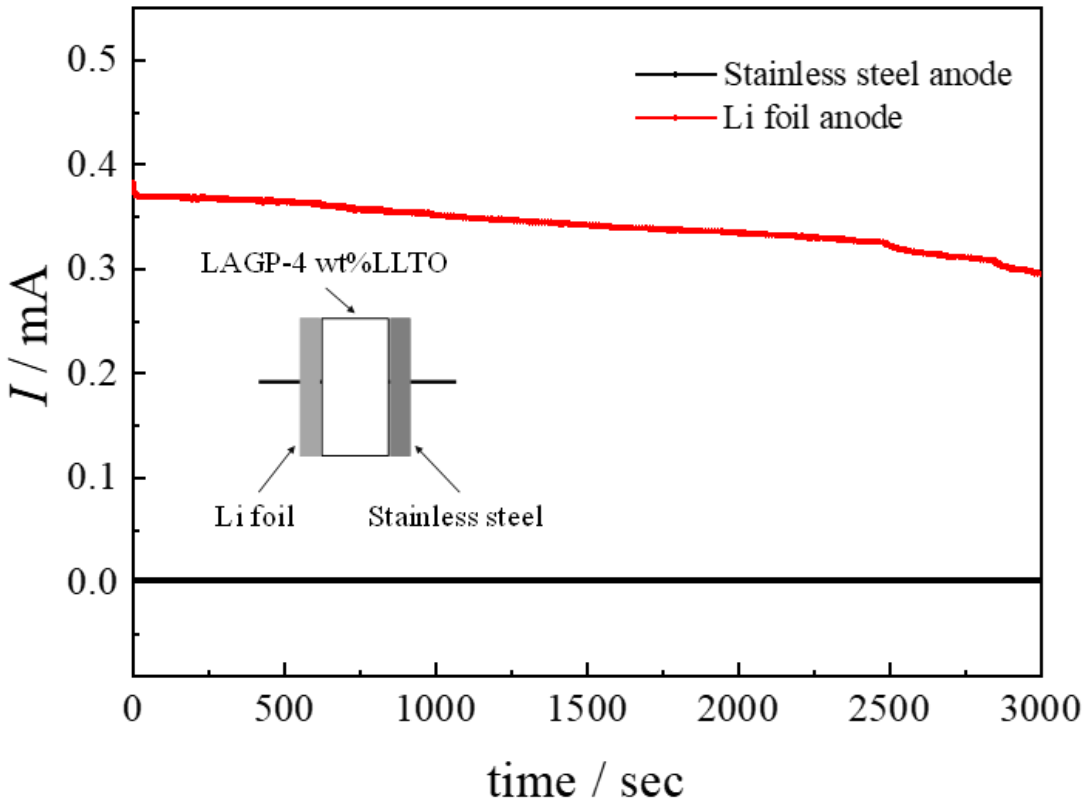

Figure 2.12 Result of potentiostatic test on LAGP – 4 wt.% LLTO composite. The schematic shows the configuration of asymmetric cell.

2.6. Summary

This chapter reports the synthesis procedures of LAGP – LLTO composites and results of subsequent crystallographic, microstructural and electrochemical characterisations. The optimum amount of LLTO addition that yields LAGP – LLTO composites with highest room-temperature conductivity is concluded. By mixing a small amount of LLTO powder with LAGP precursor and sintering, the LLTO powder would undergo a decomposition process and react with LAGP matrix to form $LaPO_4$ particles that are embedded among the LAGP matrix. In addition, GeO_2 phases can also be formed as a by-product of this reaction. Incorporating $LaPO_4$ particles in LAGP through this method could firstly increase and then decrease the room-temperature conductivity, with the maximum at LAGP – 4 wt.% LLTO. On the other hand, directly mixing LAGP precursor with $LaPO_4$ powder followed by sintering does not improve the conductivity. SEM and DLS investigations suggest that forming $LaPO_4$ particles through LLTO decomposition is essential to the conductivity enhancement, as it produces finer $LaPO_4$ particles in comparison to the directly incorporated $LaPO_4$. Therefore, in order to emphasise the starting composition of the co-sintering, the composite is nominated as LAGP – LLTO composite instead of LAGP – $LaPO_4$ composite.

The conductivity enhancement mechanism in the LAGP – LLTO composites is explained by the widely accepted space charge layer model in composite electrolytes [27,30,31,41]. The intimate contact between LAGP matrix and $LaPO_4$ particle owing to the reaction between LAGP and LLTO during sintering facilitates the change in defect concentration and subsequently increase in conductivity at the interface. Although the conductivity at space charge layer is not directly observed in this work, evidence from potentiostatic analysis results suggests that instead of electronic conduction, the improved conductivity is contributed by ionic conduction which might be originated from the space charge layer.

For further works, low-temperature EIS test is required to investigate the evolution of bulk and grain boundary conductivity as functions of LLTO addition respectively to elucidate the possibility of conductivity modification at grain boundary, which is a competing hypothesis against the space charge layer model to explain the conductivity enhancement in LAGP – LLTO composites. Lithium-ion migration behaviour can also be directly observed through solid-state NMR experiments [28–31]. Nonetheless, other additives such as La_2O_3 should be explored as lanthanum donors to form fine $LaPO_4$ particles with higher efficiency and lower impurities.

2.7. Reference

[1] B. Lang, B. Ziebarth, C. Elsässer, Lithium ion conduction in $LiTi_2(PO_4)_3$ and related compounds based on the NASICON structure: a first-principles study, Chem. Mater. 27 (2015) 5040–5048. https://doi.org/10.1021/acs.chemmater.5b01582

[2] Y. Xiao, K. Jun, Y. Wang, L.J. Miara, Q. Tu, G. Ceder, Lithium oxide superionic conductors inspired by garnet and NASICON structures, Adv. Energy Mater. 11 (2021) 2101437. https://doi.org/10.1002/aenm.202101437

[3] B. Yan, L. Kang, M. Kotobuki, L. He, B. Liu, K. Jiang, Boron group element doping of $Li_{1.5}Al_{0.5}Ge_{1.5}(PO_4)_3$ based on microwave sintering, J. Solid State Electrochem. 25 (2021) 527–534. https://doi.org/10.1007/s10008-020-04829-2

[4] X. Xu, Z. Wen, Z. Gu, X. Xu, Z. Lin, Lithium ion conductive glass ceramics in the system $Li_{1.4}Al_{0.4}(Ge_{1-x}Ti_x)_{1.6}(PO_4)_3$ (x=0–1.0), Solid State Ionics. 171 (2004) 207–213. https://doi.org/10.1016/j.ssi.2004.05.009

[5] X. Xu, Z. Wen, Z. Gu, X. Xu, Z. Lin, Preparation and characterization of lithium ion-conducting glass-ceramics in the $Li_{1+x}Cr_xGe_{2-x}(PO_4)_3$ system, Electrochem. Commun. 6 (2004) 1233–1237. https://doi.org/10.1016/j.elecom.2004.09.024

[6] Y. Nikodimos, M.-C. Tsai, L.H. Abrha, H.H. Weldeyohannis, S.-F. Chiu, H.K. Bezabh, K.N. Shitaw, F.W. Fenta, S.-H. Wu, W.-N. Su, W.-C. Yang, B.J. Hwang, Al-Sc dual-doped $LiGe_2(PO_4)_3$ - a NASICON-type solid electrolyte with improved ionic conductivity, J. Mater. Chem. A. 8 (2020) 11302–11313. https://doi.org/10.1039/D0TA00517G

[7] Y. Nikodimos, L.H. Abrha, H.H. Weldeyohannes, K.N. Shitaw, N.T. Temesgen, B.W. Olbasa, C.-J. Huang, S.-K. Jiang, C.-H. Wang, H.-S. Sheu, S.-H. Wu, W.-N. Su, C.-C. Yang, B.J. Hwang, A new high-Li^+-conductivity Mg-doped $Li_{1.5}Al_{0.5}Ge_{1.5}(PO_4)_3$ solid electrolyte with enhanced electrochemical performance for solid-state lithium metal batteries, J. Mater. Chem. A. 8 (2020) 26055–26065. https://doi.org/10.1039/D0TA07807G

[8] P. Maldonado-Manso, E.R. Losilla, M. Martínez-Lara, M.A.G. Aranda, S. Bruque, F.E. Mouahid, M. Zahir, High Lithium Ionic Conductivity in the $Li_{1+x}Al_xGe_yTi_{2-x-y}(PO_4)_3$ NASICON Series, Chem. Mater. 15 (2003) 1879–1885. https://doi.org/10.1021/cm021717j

[9] C.R. Mariappan, C. Yada, F. Rosciano, B. Roling, Correlation between micro-structural properties and ionic conductivity of Li1.5Al0.5Ge1.5(PO4)3 ceramics, J. Power Sources. 196 (2011) 6456–6464. https://doi.org/10.1016/j.jpowsour.2011.03.065

[10] C.R. Mariappan, C. Yada, F. Rosciano, B. Roling, Correlation between micro-structural properties and ionic conductivity of $Li_{1.5}Al_{0.5}Ge_{1.5}(PO_4)_3$ ceramics, J. Power Sources. 196 (2011) 6456–6464. https://doi.org/10.1016/j.jpowsour.2011.03.065

[11] X. Xu, Z. Wen, X. Wu, X. Yang, Z. Gu, Lithium ion-conducting glass–ceramics of $Li_{1.5}Al_{0.5}Ge_{1.5}(PO_4)_3 - xLi_2O$ (x=0.0 – 0.20) with good electrical and electrochemical properties, J. Am. Ceram. Soc. 90 (2007) 2802–2806. https://doi.org/10.1111/j.1551-2916.2007.01827.x

[12] H. Chung, B. Kang, Increase in grain boundary ionic conductivity of $Li_{1.5}Al_{0.5}Ge_{1.5}(PO_4)_3$

by adding excess lithium, Solid State Ionics. 263 (2014) 125–130. https://doi.org/10.1016/j.ssi.2014.05.016

[13] Y. Saito, J. Mayne, K. Ado, Y. Yamamoto, O. Nakamura, Electrical conductivity enhancement of $Na_4Zr_2Si_3O_{12}$ dispersed with ferroelectric $BaTiO_3$, Solid State Ionics. 40 (1990) 72–75. https://doi.org/10.1016/0167-2738(90)90289-4

[14] A. Mei, X.-L. Wang, Y.-C. Feng, S.-J. Zhao, G.-J. Li, H.-X. Geng, Y.-H. Lin, C.-W. Nan, Enhanced ionic transport in lithium lanthanum titanium oxide solid state electrolyte by introducing silica, Solid State Ionics. 179 (2008) 2255–2259. https://doi.org/10.1016/j.ssi.2008.08.013

[15] F. Bai, X. Shang, H. Nemori, M. Nomura, D. Mori, M. Matsumoto, N. Kyono, Y. Takeda, O. Yamamoto, N. Imanishi, Lithium-ion conduction of $Li_{1.4}Al_{0.4}Ti_{1.6}(PO_4)_3$-$GeO_2$ composite solid electrolyte, Solid State Ionics. 329 (2019) 40–45. https://doi.org/10.1016/j.ssi.2018.11.005

[16] H. Onishi, S. Takai, T. Yabutsuka, T. Yao, Synthesis and electrochemical properties of LATP-LLTO lithium ion conductive composites, Electrochemistry. 84 (2016) 967–970. https://doi.org/10.5796/electrochemistry.84.967

[17] S. Takai, T. Yabutsuka, T. Yao, Synthesis and ion conductiviyt enhancement in oxide-based solid electrolyte LLZ-LLTO and LATO-LLTO compsite (in Japanese), in: Technical Information Institute (Ed.), Dev. Technol. Mater. Fabr. Process Improv. Ion Conduct. All Solid State Batter., Technical Information Institute, Tokyo, 2017: pp. 74–80.

[18] C.C. Liang, Conduction Characteristics of the Lithium Iodide-Aluminum Oxide Solid Electrolytes, J. Electrochem. Soc. 120 (1973) 1289. https://doi.org/10.1149/1.2403248

[19] J. Maier, Heterogeneous doping of silver bromide ($AgBr:Al_2O_3$), Mater. Res. Bull. 20 (1985) 383–392. https://doi.org/10.1016/0025-5408(85)90005-4

[20] J. Maier, On the heterogeneous doping of ionic conductors, Solid State Ionics. 18 (1986) 1141–1145. https://doi.org/10.1016/0167-2738(86)90323-1

[21] A.C. Khandkar, J.B. Wagner Jr, Fast ion transport in composites, Solid State Ionics. 18 (1986) 1100–1104. https://doi.org/10.1016/0167-2738(86)90316-4

[22] J. Schoonman, F.W. Poulsen, N.H. Andersen, B. Kindl, Properties of LiI—Alumina composite electrolytes, Solid State Ionics. 9 (1983) 119–122. https://doi.org/10.1016/0167-2738(83)90219-9

[23] H. Maekawa, R. Tanaka, T. Sato, Y. Fujimaki, T. Yamamura, Size-dependent ionic conductivity observed for ordered mesoporous alumina-LiI composite, Solid State Ionics. 175 (2004) 281–285. https://doi.org/10.1016/j.ssi.2003.12.032

[24] S. Sultana, R. Rafiuddin, Enhancement of ionic conductivity in the composite solid electrolyte system: $TlI–Al_2O_3$, Ionics. 15 (2009) 621–625. https://doi.org/10.1007/s11581-008-0312-2

[25] P. Knauth, Inorganic solid Li ion conductors: An overview, Solid State Ionics. 180 (2009) 911–916. https://doi.org/10.1016/j.ssi.2009.03.022

[26] J. Maier, Ionic conduction in space charge regions, Prog. Solid State Chem. 23 (1995) 171–263. https://doi.org/10.1016/0079-6786(95)00004-E

[27] J. Maier, Pushing nanoionics to the limits: charge carrier chemistry in extremely small systems, Chem. Mater. 26 (2014) 348–360

[28] T. Asai, C.-H. Hu, S. Kawai, ^{7}Li NMR study on the LiI Al_2O_3 composite electrolyte, Mater. Res. Bull. 22 (1987) 269–274. https://doi.org/10.1016/0025-5408(87)90080-8

[29] J. Lefevr, L. Cervini, J.M. Griffin, D. Blanchard, Lithium Conductivity and Ions Dynamics in $LiBH_4/SiO_2$ Solid Electrolytes Studied by Solid-State NMR and Quasi-Elastic Neutron Scattering and Applied in Lithium–Sulfur Batteries, J. Phys. Chem. C. 122 (2018) 15264–15275. https://doi.org/10.1021/acs.jpcc.8b01507

[30] S. Breuer, V. Pregartner, S. Lunghammer, H.M.R. Wilkening, Dispersed solid conductors: fast interfacial Li-ion dynamics in nanostructured LiF and LiF: γ-Al_2O_3 composites, J. Phys. Chem. C. 123 (2019) 5222–5230. https://doi.org/https://doi.org/10.1021/acs.jpcc.8b10978

[31] V. Gulino, M. Brighi, F. Murgia, P. Ngene, P. de Jongh, R. Černý, M. Baricco, Room-Temperature Solid-State Lithium-Ion Battery Using a $LiBH_4$–MgO Composite Electrolyte, ACS Appl. Energy Mater. 4 (2021) 1228–1236 https://doi.org/10.1021/acsaem.0c02525

[32] E. Zhao, F. Ma, Y. Guo, Y. Jin, Stable LATP/LAGP double-layer solid electrolyte prepared via a simple dry-pressing method for solid state lithium ion batteries, Rsc Adv. 6 (2016) 92579–92585. https://doi.org/10.1039/C6RA19415J

[33] M. Weiss, D.A. Weber, A. Senyshyn, J. Janek, W.G. Zeier, Correlating Transport and Structural Properties in $Li_{1+x}Al_xGe_{2-x}(PO_4)_3$ (LAGP) Prepared from Aqueous Solution, ACS Appl. Mater. Interfaces. 10 (2018) 10935–10944. https://doi.org/10.1021/acsami.8b00842

[34] G.J. Redhammer, D. Rettenwander, S. Pristat, E. Dashjav, C.M.N. Kumar, D. Topa, F. Tietz, A single crystal X-ray and powder neutron diffraction study on NASICON-type $Li_{1+x}Al_xTi_{2-x}(PO_4)_3$ ($0 \leq x \leq 0.5$) crystals: Implications on ionic conductivity, Solid State Sci. 60 (2016) 99–107. https://doi.org/10.1016/j.solidstatesciences.2016.08.011

[35] S. V Pershina, B.D. Antonov, A.S. Farlenkov, E.G. Vovkotrub, Glass-ceramics in $Li_{1+x}Al_xGe_{2-x}(PO_4)_3$ system: the effect of Al_2O_3 addition on microstructure, structure and electrical properties, J. Alloys Compd. 835 (2020) 155281. https://doi.org/10.1016/j.jallcom.2020.155281

[36] P. Hartmann, T. Leichtweiss, M.R. Busche, M. Schneider, M. Reich, J. Sann, P. Adelhelm, J. Janek, Degradation of NASICON-type materials in contact with lithium metal: formation of mixed conducting interphases (MCI) on solid electrolytes, J. Phys. Chem. C. 117 (2013) 21064–21074. https://doi.org/10.1021/jp4051275

[37] S.-G. Ling, J.-Y. Peng, Q. Yang, J.-L. Qiu, J.-Z. Lu, H. Li, Enhanced ionic conductivity in LAGP/LATP composite electrolyte, Chinese Phys. B. 27 (2018) 38201. https://doi.org/10.1088/1674-1056/27/3/038201

[38] O. Nakamura, J.B. Goodenough, Conductivity enhancement of lithium bromide monohydrate by Al2O3 particles, Solid State Ionics. 7 (1982) 119–123. https://doi.org/10.1016/0167-2738(82)90004-2.

[39] R. Mercier, M. Tachez, J.P. Malugani, G. Robert, Effect of homovalent (I^-–Br^-) ion substitution on the ionic conductivity of $LiI_{1-x}Br_x$ systems, Solid State Ionics. 15 (1985)

109–112. https://doi.org/10.1016/0167-2738(85)90088-8

[40] R.C.T. Slade, I.M. Thompson, Influence of surface area and particle size of dispersed oxide on conductivities of lithium bromide composite electrolytes, Solid State Ionics. 26 (1988) 287–294. https://doi.org/10.1016/0167-2738(88)90256-1

[41] Z. Zou, Y. Li, Z. Lu, D. Wang, Y. Cui, B. Guo, Y. Li, X. Liang, J. Feng, H. Li, C.-W. Nan, M. Armand, L. Chen, K. Xu, S. Shi, Mobile Ions in Composite Solids, Chem. Rev. 120 (2020) 4169–4221. https://doi.org/10.1021/acs.chemrev.9b00760

3. LATP – La_2O_3 composite

3.1. Introduction

This chapter focuses on the enhancement of conductivity for $Li_{1.3}Al_{0.3}Ti_{1.7}(PO_4)_3$ (LATP) through insulative particle dispersion methods. Similar to the $Li_{1.5}Al_{0.5}Ge_{1.5}(PO_4)_3$ (LAGP) introduced in Chapter 2, LATP is originated from $LiTi_2(PO_4)_3$ that inherent NASICON-type lattice structure consisting of MO_6 octahedra and PO_4 tetrahedra [1–7]. As shown in Fig 2.1(b), the super-ionic skeleton of LATP (space group *R*–3*c*) allows a 3-dimensional diffusion pathways for lithium ions, which yields a high ionic conductivity. To facilitate commercialisation of LATP as solid-state electrolytes for all-solid-state batteries (ASSBs), research attentions have been focused on improvements of room-temperature conductivities of LATP electrolytes, mainly through cation or anion substitutions [8–11].

The work introduced in this chapter aims to achieve the same goal through the insulative particle dispersion technique described in Chapter 2, which can be viewed as a further work to the previously reported LATP – $Li_{0.385}La_{0.55}TiO_3$ (LLTO) composite [12]. In the previous work, $LaPO_4$ particles were incorporated in the LATP matrix through decomposition of the introduced LLTO particles during sintering, the reaction of which was believed to be vital to the 3-fold improvement in conductivity since directly added $LaPO_4$ powder failed to provide same effect [12,13]. However, the chemical composition of LLTO powder is radically different from the $LaPO_4$ particles, which could: i) lead to a 'detoured' chemical reaction towards the desired $LaPO_4$, and ii) introduce a large amount of undesired titanium ions to the resulted composite. On the other hand, forming $LaPO_4$ through *in-situ* reactions during sintering is proven by Chapter 2 and Chapter 4 to be an effective practice to enhance contact between $LaPO_4$ particle and LATP matrix, such that space charge layer can be formed at the LATP / $LaPO_4$ hetero-interface and provide rapid lithium-ion diffusion pathway. In this chapter, by employing La_2O_3 nano-powder instead of LLTO as a direct lanthanum donor to form $LaPO_4$ particles, the amount of impurity ions can be reduced, while a chemical reaction during sintering is preserved to guarantee a good interfacial contact between the $LaPO_4$ particle and LATP matrix [14].

3.2. Experiments

3.2.1. Synthesis of LATP precursor

To synthesis LATP, stoichiometric amounts of starting materials, Li_2CO_3 (99.0% Wako Pure Chem., Japan, with 10 wt.% excess), γ-Al_2O_3 (97.0% Stream Chem., USA), TiO_2 (rutile, 99.9% High Purity Chem., Japan) and $NH_4H_2PO_4$ (99.0% Wako Pure Chem.,) were weighed and mixed by an alumina mortar and pestle. The mixture was then transferred to another alumina mortar for a further 5 h mixing by an automatic grinder (ANM1000, Nitto Kagaku, Japan), during which ethanol (99.0% Wako Pure Chem.) was added and replenished every 15-20 min. The mixed slurry was firstly dried at 60 °C in air for 8 h then at 120 °C in vacuum for 24 h to remove residual moisture and ethanol. The dried mixture was uniaxially pressed by a ϕ22 mm die before being placed on a platinum foil in an alumina crucible and calcined at 700 °C for 2 h (detail of the heat-treatment is shown in Table 3.1). To form fine LATP precursor power, the calcined product was crushed by alumina mortar and pestle, then ball-milled at 400 RPM for 5 h with an aid of ethanol (Pulverisette7 premium line, Fritsch, Germany, Table 3.2). After ball-milling, the slurry was dried at 60 °C in air then 120 °C in vacuum for 24 h for further use.

3.2.2. Fabrication of pristine LATP and LATP – La_2O_3 composites

For pristine LATP pellet fabrication, the fine LATP precursor was weighed and uniaxially pressed using a ϕ7 mm die to form pellets. The obtained pellets were sealed in rubber probe covers by vacuum pump and subjected to isostatic pressing at 200 MPa for 3 min. The pressed pellets were embedded in the LATP precursor and placed on a platinum foil in an alumina crucible to sinter at 1000 °C for 2 to 10 h. The detailed sintering conditions are listed in Table 3.3.

For LATP – La_2O_3 composite pellet fabrication, the fine LATP precursor and La_2O_3 nano powder (<100 nm, 99% Sigma-Aldrich, Germany) were weighed and mixed by an alumina mortar and pestle before further mixing through ball-milling (zirconia pot and balls, Pulverisette7 premium line, Fritsch, Germany) with an aid of ethanol. The detailed ball-milling conditions are listed in Table 3.4. The ball-milled slurry was dried at 60 °C overnight and then at 120 °C in vacuum for 24 h to form dried powder, which was weighed and uniaxially pressed using a ϕ7 mm die. The formed pellets were isostatically pressed at 200 MPa for 3 min (Dr. CIP, KOBELCO) before being embedded by the dried LATP – La_2O_3 mixture powder and sintered at conditions listed in Table 3.3. The weighed La_2O_3 nano power was 2, 4, 6, 8, 12 and 16 wt.% of the total weight (LATP + La_2O_3).

Table 3.1 Heat-treatment condition for LATP calcination.

heating rate	5 °C/min
calcinating temperature	700 °C
calcinating time	2 h
cooling rate	5 °C/min
crucible	Al_2O_3 with a Pt foil
heat-treat atmosphere	air

Table 3.2 Ball-milling conditions for the fine LATP precursor formation.

pot and balls	zirconia (Fritsch)
ball size	ϕ5 mm
mass ratio (ball:sample)	10:1
ball-mill stage	Pulverisette7 premium line, Fritsch
duration	60 min
rest interval	60 min
cycles (total ball-milling time)	5 (5 h in total)
ball-mill media	ethanol (99.0% Wako Pure Chem)

Table 3.3 Heat-treatment conditions for LATP and LATP – La_2O_3 composite sintering.

heating rate	5 °C/min
sintering temperature	1000 °C
sintering time	2-10 h
cooling rate	5 °C/min
crucible	Al_2O_3 with a Pt foil
heat-treat atmosphere	air

Table 3.4 Ball-milling conditions for LATP precursor – La_2O_3 powder mixture fabrication.

pot and balls	zirconia (Fritsch)
ball size	ϕ5 mm
mass ratio (ball:sample)	10:1
ball-mill stage	Pulverisette7 premium line, Fritsch
duration	30 min
rest interval	30 min
cycles (total ball-milling time)	3 (1.5 h in total)
ball-mill media	ethanol (99.0% Wako Pure Chem)

3.2.3. Characterisations

In investigation of the phase composition of pristine LATP and LATP – La_2O_3 composite, the sintered pellets were crushed to form powder using alumina mortar and pestle before being loaded onto glass holders for powder X-ray diffraction (XRD) characterisations (Ultima VI diffractometer, Rigaku, Japan). The detailed powder XRD characterisation conditions are listed in Table 3.5. To prepare for microstructural investigation, the samples were polished by abrasive paper up to #3000 grade. A field emission scanning electron microscopy (FE-SEM, SU-6600, Hitachi, Japan) operating at 20 mA and 20 kV was employed to observe the back-scattered electron images without applying gold-sputtering. To verify the size of La_2O_3 nano-powder, 0.2 grams of La_2O_3 regent was suspended in deionised water and loaded in a glass tube for dynamic light scattering (DLS), with scattering test repeated 100 times.

To prepare for electrochemical impedance spectroscopy (EIS) investigation, the sample pellets were polished on two surfaces to obtain mirror finish using abrasive papers up to #3000 grid before being sputtered with gold using a magnetron plasma sputter (MSP-Mini Magnetron Sputter, Vacuum Device, Japan) to form lithium-blocking electrodes. The pellets were loaded in a 4-electrode cell placed in a tubular furnace and connected with an LRC metre (3531 Z Hitester, Hioki, Japan) to conduct EIS characterisations under controlled temperatures. A temperature controller (AGC-S, ASAHI Rika, Japan) coupled with type-K thermocouple was employed to manage the temperature of the tubular furnace. The impedance data were collected in a frequency range of 130 Hz-4.1 MHz under a temperature range of 25-200 °C to measure the temperature dependency of the sample conductivity.

Table 3.5 Specifications of X-ray diffractometer and powder XRD.

diffractometer	Ultima VI, Rigaku
scanning speed	2 °/min
step size	0.04 °
2θ range	10 ° - 40 °
x-ray generator (wavelength)	copper Kα (0.154 nm)
voltage and current	40 kV, 40 mA

3.3. Phase Composition

This section includes investigation of the phase composition of LATP – La_2O_3 composites as functions of La_2O_3 addition and sintering time. Secondary phases are identified, and the phase stability of LATP after co-sintering with La_2O_3 is also evaluated. The characterisation results are utilised to determine the optimum La_2O_3 addition and heat-treatment condition during sintering.

The power XRD patterns of pristine LATP, LATP *x* wt.% La_2O_3 composite and La_2O_3 nano powder are shown in Fig 3.1. The major peaks of the LATP – *x* wt.% La_2O_3 composite are associated with the pristine LATP, which has identical lattice structure with the $LiTi_2(PO_4)_3$ (PDF# 35-0754). The unchanged peak positions indicate the stability of LATP matrix during the co-sintering with La_2O_3 nano powder, no significant substitution in LATP lattice from La_2O_3 is observed. The detection of $LaPO_4$ phase instead of the introduced La_2O_3 nano powder suggests a possible solid-state reaction between the LATP matrix and La_2O_3 nano powder during sintering, where the LATP acted as phosphate donor and La_2O_3 the lanthanum donor to form $LaPO_4$ phase that increases as a function of La_2O_3 addition. Similar reactions are also observed in LATP – LLTO composites and LAGP – LLTO composites, where the introduced LLTO acted as lanthanum donor and formed $LaPO_4$ particles. In this work, although replacing LLTO with La_2O_3 as lanthanum donor to form $LaPO_4$ reduces the titanium ions introduced to the composite, $LiTiPO_5$ phase was identified in the composite samples as impurity phases as labelled by hollow diamond in Fig 3.1. It is believed that this phase is formed as a phosphorus-depleted phase when LATP donates phosphate to form $LaPO_4$ phase. At higher La_2O_3 addition, the growth in $LiTiPO_5$ is accompanied by the appearance of an unidentified impurity which is unlikely to be the unreacted La_2O_3 since the pick positions are different from that of La_2O_3 nano powder.

The relation between sintering time and the amounts of impurities was studied by sintering the LATP – 8 wt.% La_2O_3 composites at 1 to 10 h. The powder XRD results of the sintering product are shown in Fig 3.2. Although the peak intensity of $LaPO_4$ firstly increased until 4 h of sintering and then decreased, the $LiTiPO_5$ phase and unidentified impurity phase constantly remained despite a prolonged sintering time. This might indicate that the impurity phases are formed through thermodynamic processes, which should be eliminated through optimising the sintering temperature during co-sintering.

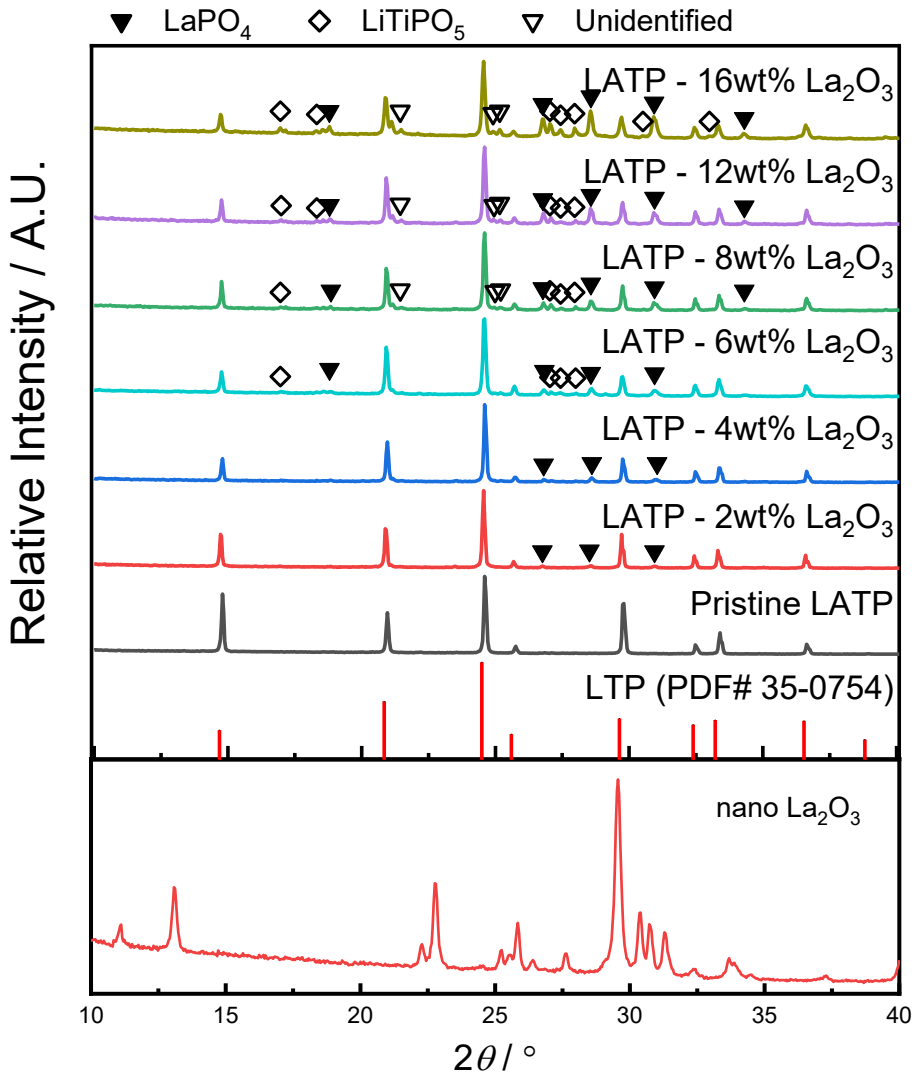

Figure 3.1 Powder XRD patterns of pristine LATP, LATP – *x* wt.% La_2O_3 composite and La_2O_3 nano powder. Peaks in addition to that from LTP lattice structure are identified as $LaPO_4$ (invert triangle) and $LiTiPO_5$ (hollow diamond), the unidentified peaks are labelled by hollow invert triangle.

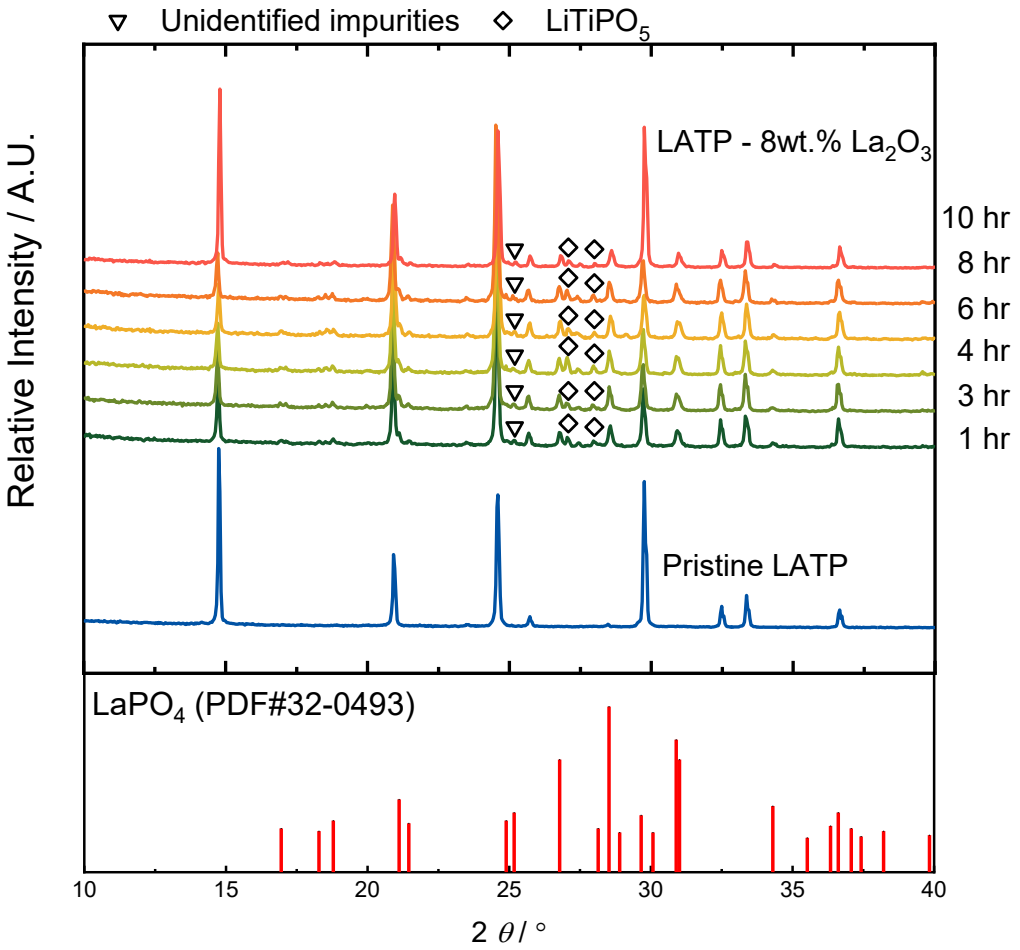

Figure 3.2 Powder XRD pattern of LATP – 8wt% La_2O_3 composites with sintering times ranging from 1 to 10 h, the unidentified impurity and $LiTiPO_5$ peaks are labelled by hollow inverted triangles and hollow diamonds.

3.4. Microstructural Analysis

In this section, the size and distribution of $LaPO_4$ particles in LATP matrix are investigated through SEM observations as functions of La_2O_3 addition and sintering time. The results provide vital evidence for determination of optimised sintering conditions. By comparing the size of La_2O_3 nano-powder and $LaPO_4$ particles before and after sintering based on SEM and DLS results, the effect of LATP – La_2O_3 reaction during sintering on the $LaPO_4$ particle distribution is elaborated.

The back-scattered SEM images of pristine LATP and LATP – *x* wt.% La_2O_3 composites are shown in Fig 3.3. The microstructures of the composites are consisted of dark matrix area and bright $LaPO_4$ particles. The $LaPO_4$ particles reflect more back-scattered electrons than the matrix due to the heavy lanthanum atom and therefore appear brighter. For La_2O_3 additions lower than 8 wt.%, the $LaPO_4$ particles remain isolated with diameters around 1 μm. The relatively small particle size can be attributed to the solid-state reaction between La_2O_3 and LATP during co-sintering. Although the nominal diameter of the La_2O_3 nano powder that are employed to produce the composites was approximately 100 nm, agglomeration of the particles can be severe due to aging of the reagent, as shown by the DLS and secondary electron SEM images in Fig 3.4. The agglomerated La_2O_3 powder has diameter ranging from 1 to 10 μm with mean diameter being 2.77 μm, which can be significantly larger than the particle sizes observed on Fig 3.3 (b)-(d). At higher La_2O_3 additions such as 12 and 16 wt.%, the $LaPO_4$ particles can severely aggregate to from large $LaPO_4$ clusters that breaks the continuity of the LATP matrix.

The microstructure of the LATP – 8 wt.% La_2O_3 composite is also investigated as a function of sintering time. As shown in Fig 3.5, the $LaPO_4$ particle exhibits evident aggregation behaviour when sintering time exceeds 4 h, suggesting that sintering LATP – La_2O_3 composite for longer than 4 h might result in deteriorated dispersion of $LaPO_4$ particles.

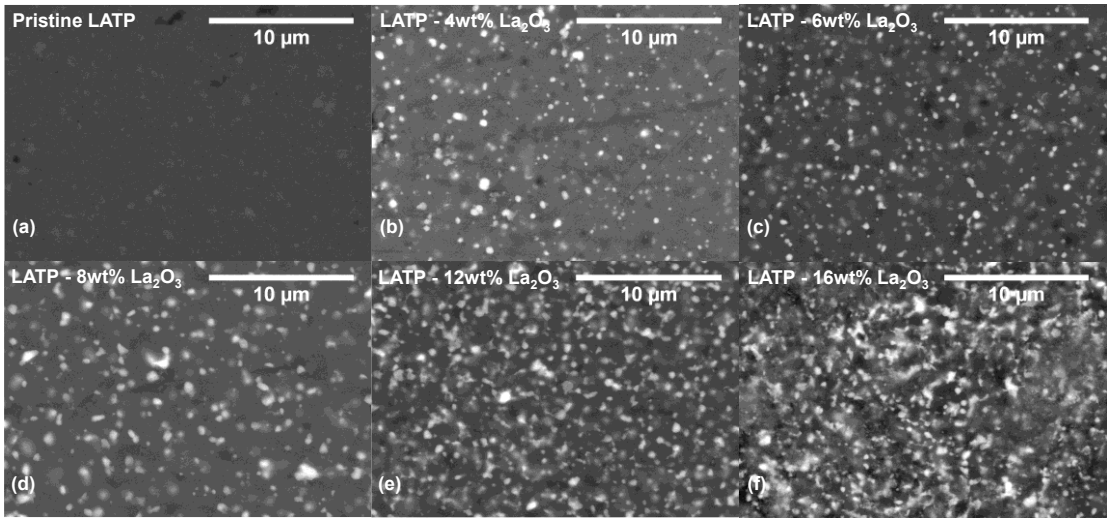

Figure 3.3 Back-scattered SEM images of (a) pristine LATP, (b) LATP – 4 wt.% La_2O_3, (c) LATP – 6 wt.% La_2O_3, (d) LATP – 8 wt.% La_2O_3, (e) LATP – 12 wt.% La_2O_3, and (f) LATP – 16 wt.% La_2O_3 composites.

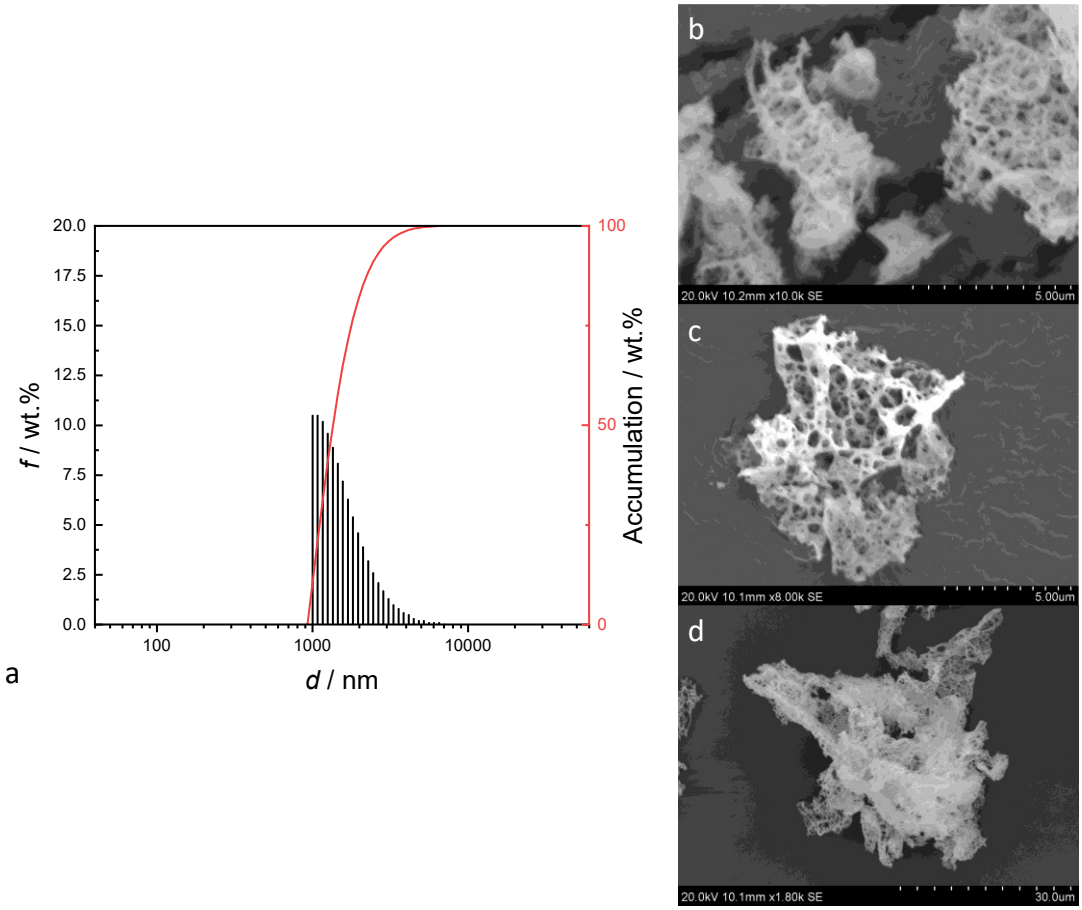

Figure 3.4 (a) Particle size distribution by weight percentages measured from DLS on La_2O_3 nano powder suspended in deionised water. (b)-(d) Secondary electron SEM images of La_2O_3 nano powder.

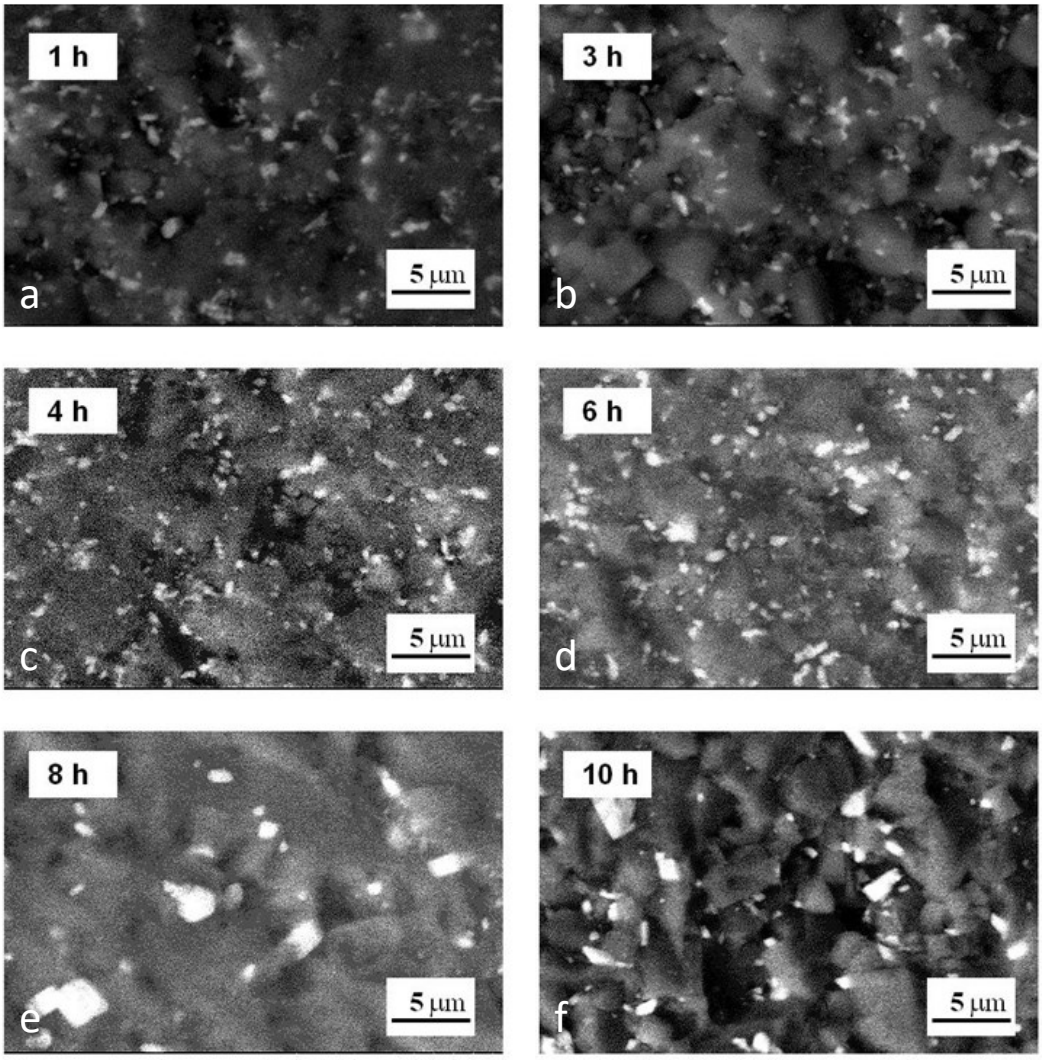

Figure 3.5 Back-scattered SEM images of LATP – 8 wt.% sintered for (a) 1 h, (b) 3 h, (c) 4 h, (d) 6 h, (e) 8 h, and (f) 10 h.

3.5. Electrochemical Analysis

In this section, the electrochemical property of the LATP – La_2O_3 composites are evaluated as functions of La_2O_3 addition and sintering time, based on conductivities and activation energies interpretated from room-temperature and temperature-dependent EIS analysis. The results are also compared with LATP – LLTO composites to study the difference in $LaPO_4$ aggregation limit and maximum conductivities between the two systems, which provides directions for further studies. The results are also used to determine the optimum heat-treating condition for sintering.

The Nyquist plots of EIS spectra for pristine LATP and LATP – *x* wt.% La_2O_3 composites measured at room temperature are shown in Fig 3.6. On the spectra for all samples, a semi-circle starting from 1.9 MHz and ending at 14 kHz which is followed by a linear section with slope approximately equal to 1 can be observed. Due to the limited frequency range, the semi-circles from the bulk and grain boundary of the samples are not resolved on the spectra. Therefore, the spectra are fitted by using a conventional equivalent circuit shown in the inset of Fig 3.6 to calculate the right end of the semi-circles as the total resistivities of the samples, which are summarised in Table 3.6 and plotted as a function of La_2O_3 addition in Fig 3.7. The conductivity of LATP – *x* wt.% La_2O_3 composite firstly increase and then decreased with the La_2O_3 addition, achieving a highest conductivity of 0.69 mS/cm at 6 wt.% of La_2O_3 addition. This phenomenon indicates that dispersion of the $LaPO_4$ particle in LATP matrix can enhance the conductivity, which is similar to what was observed in LATP – *x* wt.% LLTO and LAGP – *x* wt.% LLTO systems, as well as insulative particle dispersed systems in halide-based lithium-ion conductors [12,14,15]. At La_2O_3 introduction higher than 6 wt.%, the aggregation of the $LaPO_4$ becomes significant, forming large insulative $LaPO_4$ particles, as observed in Fig 3.3 (d)-(f), which impedes the long-range migration of lithium ions and hence reduces the conductivity.

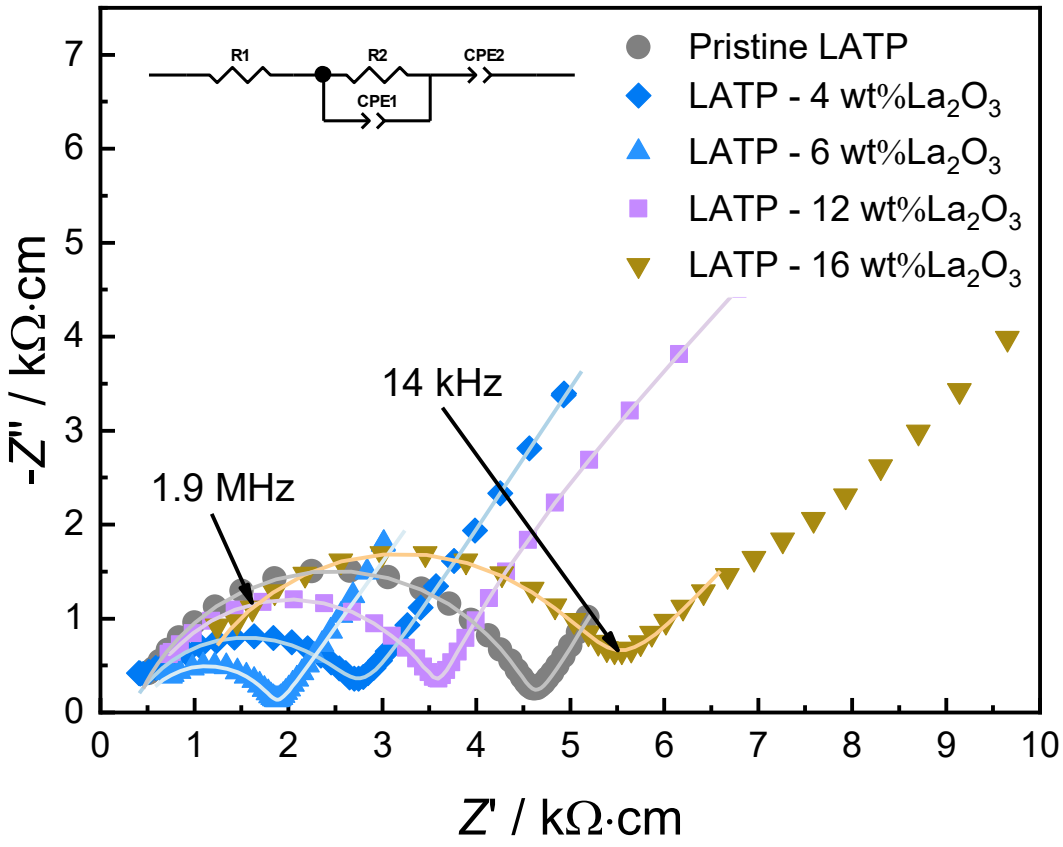

Figure 3.6 Normalised Nyquist plot of electrochemical impedance for pristine LATP and LATP – *x* wt.% La_2O_3 samples, measured at 25 °C.

Table 3.6 Room temperature conductivity and activation energy of LATP – *x* wt.% La_2O_3 composites.

La_2O_3 addition (wt.%)	σ (mS·cm^{-1})	E_a (eV)
0	0.2307	0.2545
2	0.2794	0.2523
4	0.4222	0.2934
6	0.6864	0.2802
8	0.6200	0.2704
12	0.3202	0.3111
16	0.2405	0.2884

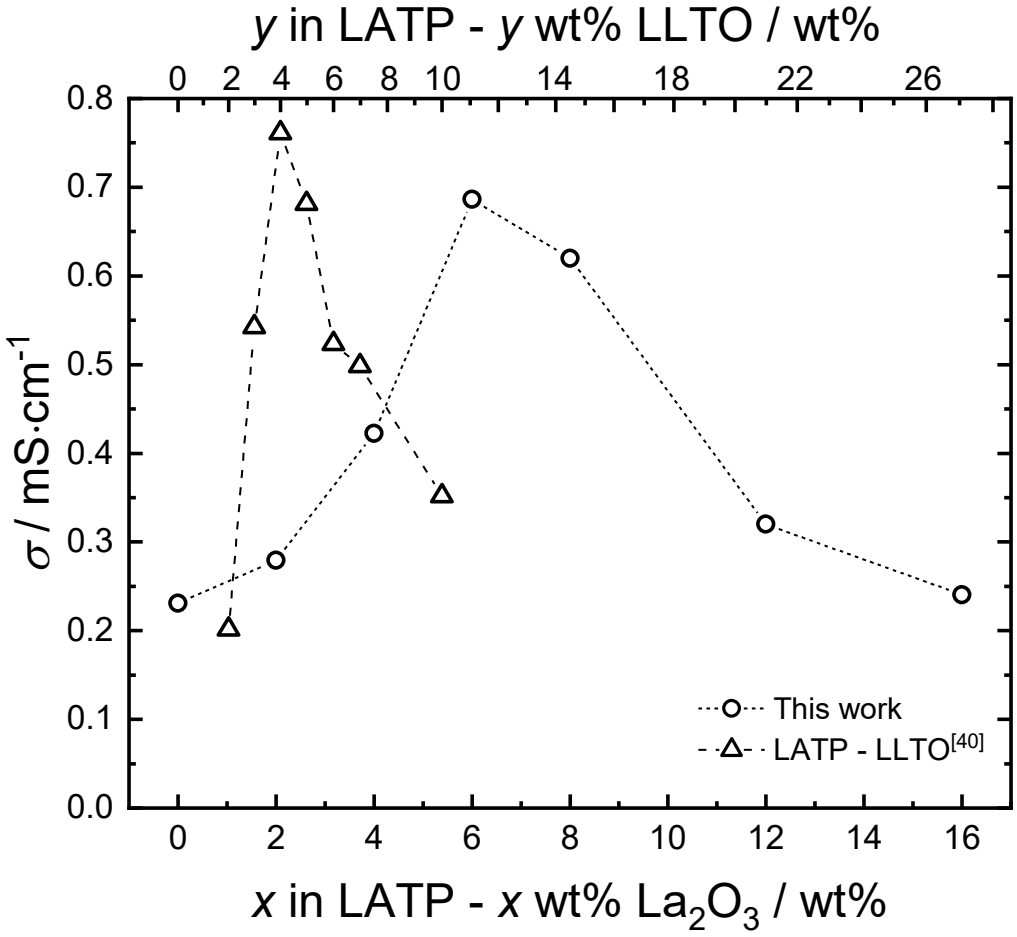

Figure 3.7 Conductivity of LATP – *x* wt.% La_2O_3 composites (open circles) measured at 25 °C, as a function of La_2O_3 addition, in comparison with the results in LATP – *y* wt.% LLTO system (open triangle) reported in ref. [12].

The room-temperature conductivities of LATP – *x* wt.% LLTO composites are also presented in Fig 3.7 for comparison, where the amount of LLTO addition is converted to the equivalent La_2O_3 addition based on the amount of lanthanum in the LLTO. The original wt.% of LLTO addition is labelled on the upper x axis. For LATP – LLTO system, the maximum conductivity for the composite is marginally higher than that of the LATP – La_2O_3 system. However, the aggregation of the $LaPO_4$ particle starts relatively earlier than that in LATP – La_2O_3 system, leading to early decline in conductivity at relatively low lanthanum addition. Despite the agglomeration observed in Fig 3.5, the relatively high reactivity of La_2O_3 nano-powder can yield $LaPO_4$ particles that are in smaller sizes and with more homogeneous distribution across the LATP matrix. This can lead to a higher tolerance of lanthanum addition in comparison to the LATP – LLTO system, and hence a slower $LaPO_4$ particle aggregation as a function of La_2O_3 addition. On the other hand, formation of $LiTiPO_5$ identified from powder XRD in Fig 3.1 can contribute to a lower maximum conductivity in the LATP – La_2O_3 system, which stresses the importance of minimising the impurity formation during the co-sintering process to further enhance the conductivity for the composite electrolytes.

The relationship between the sintering time and room-temperature conductivity of LATP – 8 wt.% La_2O_3 was also investigated with results listed in Table 3.7 and plotted as a function of sintering time in Fig 3.8, where the conductivity decreases with the sintering time. As sintering time increases, the growth of $LaPO_4$ particles as observed in Fig 3.5 leads to the decrease of LATP matrix / $LaPO_4$ particle interface, resulting in a reduced amount of space charge layer that exist at the vicinity of the interface and hence a reduced conductivity.

The EIS investigations of pristine LATP and LATP – *x* wt.% La_2O_3 were also conducted at the temperature range from 50 °C to 200 °C to examine the temperature dependence behaviours of the samples. The results are shown in the Arrhenius plots in Fig 3.9 (a), where linear behaviours for all of the samples can be observed and allows calculation of activation energy for conductivity for all of the samples (Table 3.6 and Fig 3.9 (b)) according to Arrhenius equation (Eq 3.2). Although the activation energy of LATP – *x* wt.% La_2O_3 composite is slowly increased with the La_2O_3 addition, the overall results are similar to that of the pristine LATP and that of the LATP – LLTO composites [12]. This indicates that the lithium migration mechanism in the LATP – La_2O_3 composites are in general consistent with the pristine LATP.

Table 3.7 Room temperature conductivity of LATP – 8 wt.% La_2O_3 composite with different sintering time.

Sintering time (h)	σ (mS·cm^{-1})
1	0.6370
3	0.5260
4	0.6200
6	0.1170
8	0.0720
10	0.0640

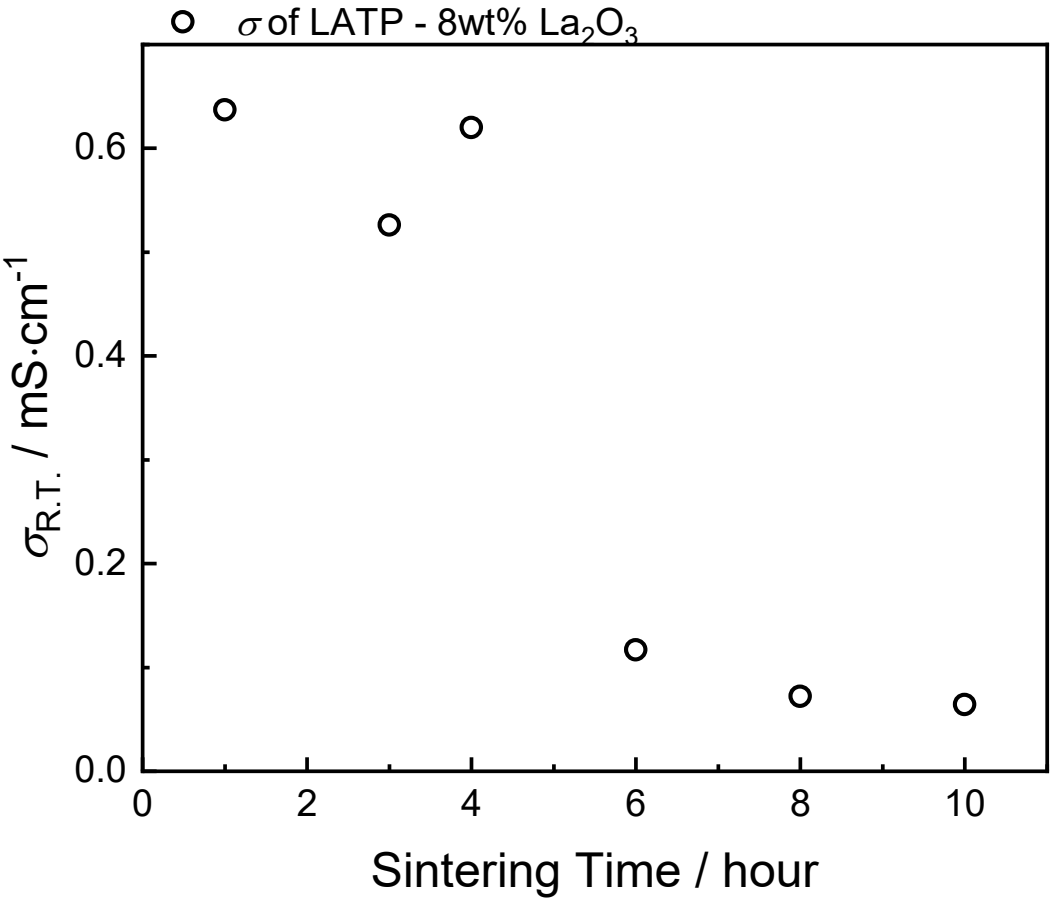

Figure 3.8 Conductivity of LATP – 8 wt.% La_2O_3 composite measured at 25 °C, as a function of sintering time.

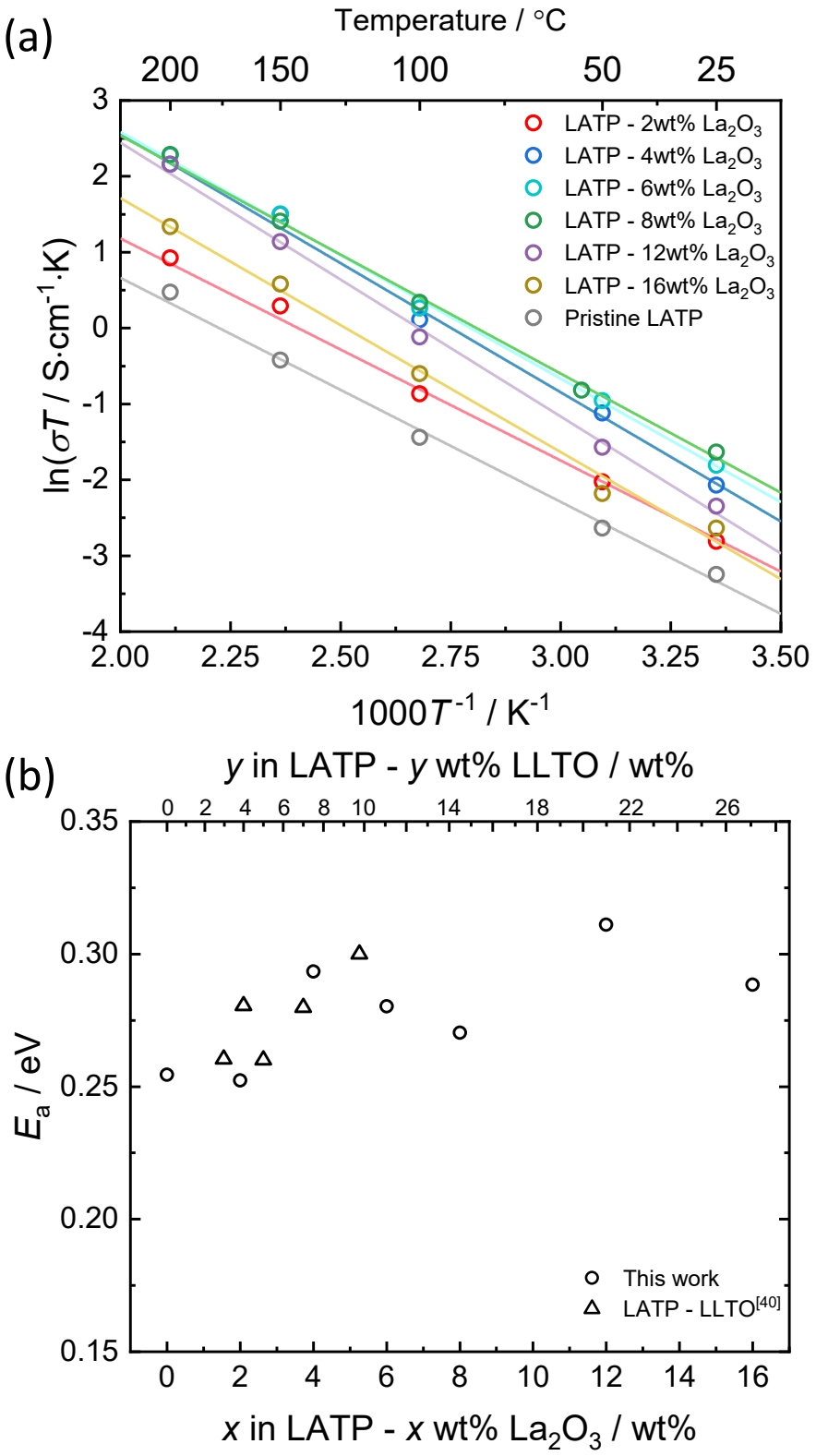

Figure 3.9 (a) Arrhenius plots for conductivity of LATP – *x* wt.% La_2O_3 samples and (b) activation energies of conductivities as a function of La_2O_3 addition, with the result of previous work on LATP – *y* wt.% LLTO system [12].

3.6. Summary

This chapter focuses on the synthesis of LATP – La_2O_3 composites, and their subsequent characterisation results on phase composition, microstructural evolution and electrochemical properties as functions of La_2O_3 addition and sintering time. Similar to LATP – LLTO composites [12], co-sintering LATP precursor with La_2O_3 nano-powder can form composite electrolytes with $LaPO_4$ particles in LATP matrix. The $LaPO_4$ particle is believed to be formed by reaction between the La_2O_3 (as lanthanum donor) and LATP precursor (as phosphorus donor). Although La_2O_3 nano-powder does not contain any impurity ion in contrast to LLTO, $LiTiPO_5$ impurity phase is formed in the LATP – La_2O_3 composites despite a prolonged or shortened sintering time. Such phase is believed to be the by-product of La_2O_3 – LATP reaction during sintering, where LATP becomes phosphorus-depleted after donating PO_4^{3-} to form $LaPO_4$ and eventually forms $LiTiPO_5$. Nonetheless, incorporating $LaPO_4$ particles in LATP matrix increases the room-temperature conductivity by a maximum of 2-fold (0.69 $mS \cdot cm^{-1}$) at 6 wt.% of La_2O_3 addition. Combining the results from powder XRD, SEM and EIS, the sintering time for sintering is optimised to 4 h, which gives minimum impurity phase, finest $LaPO_4$ with good distribution and satisfying room-temperature conductivity.

For further study, low-temperature EIS tests and ^7Li solid-state nuclear magnetic resonance (NMR) analysis on LATP – La_2O_3 composites are required to study the evolution of bulk, grain boundary and space charge layer conductivity as a function of La_2O_3 addition respectively, and directly observed the lithium-ion migration behaviour along the space charge layer [16,17]. It is also vital to explore secondary additives in the LATP – La_2O_3 system to serve as phosphorus donors that are alternative to LATP precursor to reduce the formation of $LiTiPO_5$ impurities.

3.7. Reference

[1] M.A. Subramanian, R. Subramanian, A. Clearfield, Lithium ion conductors in the system $AB(IV)_2(PO_4)_3$ (B = Ti, Zr and Hf), Solid State Ionics. 18 (1986) 562–569. https://doi.org/10.1016/0167-2738(86)90179-7

[2] Z.-X. Lin, H.-J. Yu, S.-C. Li, S.-B. Tian, Lithium ion conductors based on $LiTi_2P_3O_{12}$ compound, Solid State Ionics. 31 (1988) 91–94. https://doi.org/10.1016/0167-2738(88)90291-3

[3] H. Aono, E. Sugimoto, Y. Sadaoka, N. Imanaka, G. Adachi, Ionic conductivity of solid electrolytes based on lithium titanium phosphate, J. Electrochem. Soc. 137 (1990) 1023. https://doi.org/10.1149/1.2086597

[4] H. Aono, N. Imanaka, G. Adachi, High Li^+ conducting ceramics, Acc. Chem. Res. 27 (1994) 265–270. https://doi.org/10.1021/ar00045a002

[5] Z. Gao, H. Sun, L. Fu, F. Ye, Y. Zhang, W. Luo, Y. Huang, Promises, challenges, and recent progress of inorganic solid-state electrolytes for all-solid-state lithium batteries, Adv. Mater. 30 (2018) 1705702. https://doi.org/10.1002/adma.201705702

[6] F. Zheng, M. Kotobuki, S. Song, M.O. Lai, L. Lu, Review on solid electrolytes for all-solid-state lithium-ion batteries, J. Power Sources. 389 (2018) 198–213. https://doi.org/10.1016/j.jpowsour.2018.04.022

[7] M. Monchak, T. Hupfer, A. Senyshyn, H. Boysen, D. Chernyshov, T. Hansen, K.G. Schell, E.C. Bucharsky, M.J. Hoffmann, H. Ehrenberg, Lithium diffusion pathway in $Li_{1.3}Al_{0.3}Ti_{1.7}(PO_4)_3$ (LATP) superionic conductor, Inorg. Chem. 55 (2016) 2941–2945. https://doi.org/10.1021/acs.inorgchem.5b02821

[8] A.S. Best, P.J. Newman, D.R. Macfarlane, K.M. Nairn, S. Wong, M. Forsyth, Characterisation and impedance spectroscopy of substituted $Li_{1.3}Al_{0.3}Ti_{1.7}(PO_4)_{3-x}(ZO_4)_x$ (Z= V, Nb) ceramics, Solid State Ionics. 126 (1999) 191–196. https://doi.org/10.1016/S0167-2738(99)00212-X

[9] D.H. Kothari, D.K. Kanchan, Effect of doping of trivalent cations Ga^{3+}, Sc^{3+}, Y^{3+} in $Li_{1.3}Al_{0.3}Ti_{1.7}(PO_4)_3$ (LATP) system on Li^+ ion conductivity, Phys. B Condens. Matter. 501 (2016) 90–94. https://doi.org/10.1016/j.physb.2016.08.020

[10] Z. Cai, Y. Huang, W. Zhu, R. Xiao, Increase in ionic conductivity of NASICON-type solid electrolyte $Li_{1.5}Al_{0.4}Ti_{1.5}(PO_4)_3$ by Nb_2O_5 doping, Solid State Ionics. 354 (2020) 115399. https://doi.org/10.1016/j.ssi.2020.115399

[11] A. Kızılaslan, M. Kırkbınar, T. Cetinkaya, H. Akbulut, Sulfur doped $Li_{1.3}Al_{0.3}Ti_{1.7}(PO_4)_3$ solid electrolytes with enhanced ionic conductivity and a reduced activation energy barrier, Phys. Chem. Chem. Phys. 22 (2020) 17221–17228. https://doi.org/10.1039/D0CP03442H

[12] H. Onishi, S. Takai, T. Yabutsuka, T. Yao, Synthesis and electrochemical properties of LATP-LLTO lithium ion conductive composites, Electrochemistry. 84 (2016) 967–970. https://doi.org/10.5796/electrochemistry.84.967

[13] S. Takai, T. Yabutsuka, T. Yao, Synthesis and ion conductiviyt enhancement in oxide-based solid electrolyte LLZ-LLTO and LATO-LLTO compsite (in Japanese), in:

Technical Information Institute (Ed.), Dev. Technol. Mater. Fabr. Process Improv. Ion Conduct. All Solid State Batter., Technical Information Institute, Tokyo, 2017: pp. 74–80.

[14] J. Maier, Pushing nanoionics to the limits: charge carrier chemistry in extremely small systems, Chem. Mater. 26 (2014) 348–360. https://doi.org/10.1021/cm4021657

[15] S. Breuer, V. Pregartner, S. Lunghammer, H.M.R. Wilkening, Dispersed solid conductors: fast interfacial Li-ion dynamics in nanostructured LiF and LiF:γ-Al_2O_3 composites, J. Phys. Chem. C. 123 (2019) 5222–5230. https://doi.org/https://doi.org/10.1021/acs.jpcc.8b10978

[16] V. Gulino, M. Brighi, F. Murgia, P. Ngene, P. de Jongh, R. Černý, M. Baricco, Room-Temperature Solid-State Lithium-Ion Battery Using a $LiBH_4$–MgO Composite Electrolyte, ACS Appl. Energy Mater. 4 (2021) 1228–1236 https://doi.org/10.1021/acsaem.0c02525

4. Neutron Radiography and HR-TEM observation of LATP – LLTO composite

4.1. Introduction

This chapter is based on characterisations of the $Li_{1.3}Al_{0.3}Ti_{1.7}(PO_4)_3$ – $Li_{0.385}La_{0.55}TiO_3$ (LATP – LLTO) composite using neutron radiography and high-resolution transmission electron microscopy (HR-TEM) experiments to measure the tracer diffusion coefficients and observe the morphology of the $LaPO_4$ particles within the LATP – LLTO composites. In the previously reported LATP – LLTO composites, although the conductivity enhancement was ascribed to the formation of space charge layer at the LATP – $LaPO_4$ hetero-interface, the lithium-ion migration behaviour at the space charge layer in LATP – LLTO composite or other oxide-based systems are rarely studied [1]. Since the total ionic conductivity in LATP – $LaPO_4$ composite is higher than that of the pristine LATP, it is predicted by the Nernst-Einstein relation that the overall diffusion coefficient of lithium ion in LATP – $LaPO_4$ composite should be higher than LATP, assuming that the concentration of lithium ion in the composite and pristine LATP are identical [2,3]. Therefore, it is important to experimentally measure the long-range diffusion coefficient in LATP – $LaPO_4$ composite and compare with that of the LATP. Owing to the composite nature of the LATP – $LaPO_4$ system, it is also critical to select a suitable technique for the measurement of diffusion coefficient.

In ionic conductors, the chemical diffusion coefficient D_σ is usually derived from the electrochemical impedance spectroscopy (EIS) test results using the Nernst-Einstein relation [2,3]. One drawback of this method involves treating AC ionic conductivity as DC ionic conductivity, which, depending on the equivalent circuit employed to fit the conductivity, might introduce error from imaginary impedance and subsequently distort the diffusivity results. A most common method for diffusivity measurement in ionic conductors is galvanostatic intermittent titration technique (GITT) to calculate the chemical diffusion coefficient using the transient response of the ionic conductor to the pulsed DC perturbation [4]. To measure tracer diffusion coefficients D^* (self-diffusion coefficient), many works have been employing nuclear magnetic resonance (NMR) technique that operates on spin lattice relaxation mode (SLR) to interpret the tracer diffusion coefficient by measuring the atomic scale lattice relaxation [5–8]. However, the powder sample required by SLR NMR could yield particle-size-dependent results that are different from the bulk materials [3,8,9]. Hayamizu *et al.* have established a technique using pulsed-gradient

spin-echo (PGSE) NMR to measure the lithium tracer diffusion coefficients on micrometer scale, despite that the measured diffusion coefficient can be dependent to the observation time and pulse-filed gradient (PFG) [9–13]. Other techniques such as muon Spin Relaxation (μ^+SR) or quasi-elastic neutron scattering (QENS) have also been developed to measure the tracer diffusion coefficient in powder samples, these methods are also indirect methods that involve calculating long-range diffusion coefficients from atomic scale jump rates [14–18].

Direct measurements on long-range diffusion coefficient measurements usually involve direct observation of diffusion profiles which allows calculation of diffusion coefficients from solutions to the Fick's laws [19,20]. One established method is using secondary ion mass spectroscopy (SIMS) which visualizes the diffusion profiles of isotope lithium ions through depth-profiling [3,21–26], time of flight detection (ToF) [27], or mapping [28,29]. However, the knock-on effect from the incident ion beam in SIMS can be severe in depth-profiling mode, which can distort the positional information of isotope lithium ions [21,22]. It is also difficult to visualize the tracer concentration profile in the LATP – $LaPO_4$ composite electrolyte through SIMS detection since the heterogeneous microstructure (i.e., $LaPO_4$ particles embedded in LATP matrix) could introduce a significant amount of noise on the SIMS spectra.

Neutron radiography (NR) is an effective technique to visualise the diffusion profile in bulk samples on a macroscopic scale utilizing the large difference in neutron absorption ability (attenuation coefficients) for ^{6}Li and ^{7}Li isotopes [30–32]. The neutron flux is largely attenuated at ^{6}Li while barely interact with ^{7}Li, which allow the visualisation of lithium diffusion profile in the bulk sample with ^{7}Li as host and ^{6}Li as tracer. This method has been successfully applied to measure the lithium-ion tracer diffusion coefficients in a variety of lithium-ion conductive materials [30,31,33–37]. By directly visualising the tracer diffusion profiles of a bulk sample on a millimetre scale, the method is suitable for diffusion coefficient measurement for the LATP – $LaPO_4$ composite samples. Therefore, in this work, the NR method is employed to measure the lithium-ion tracer diffusion coefficients in LATP and LATP – $LaPO_4$ composite samples to study the difference in lithium-ion diffusion behaviour in these samples, with results compared to other works.

Although the formation of $LaPO_4$ phase in LATP – LLTO composites have been proven through the powder X-ray diffraction (XRD) patterns in previous work, the morphology of the $LaPO_4$ particle and of the surroundings of the hetero-interface have not been precisely observed. In this work, morphology, chemical composition, and lattice structure of the particles have been

investigated through HR-TEM imaging, energy dispersive spectrometry (EDS) and selected area electron diffraction (SAED) characterization. In addition, the morphology of LATP matrix / $LaPO_4$ particle interface has also been studied.

4.2. Experiments

4.2.1. Synthesis of natural lithium and ^{7}Li LLTO powder

^{7}Li LATP was prepared by conventional solid-state reaction methods with ^{7}Li provided from $^{7}Li_2CO_3$. The $^{7}Li_2CO_3$ was prepared by reacting $^{7}LiOH$ (Tomiyama's High Purity Chem., Japan) with gaseous CO_2 (>99.5%, Masuda Medical Instruments, Japan) at 130 to 140 °C in a round-bottom flask heated by a mantle heater (HF-500S, AS ONE, Japan).

Synthesis of natural-abundance-lithium- and ^{7}Li LLTO is similar to that introduced in section 3.2.1. Stoichiometric amount of $^{7}Li_2CO_3$ or natural Li_2CO_3 (99% Wako Pure Chem., Japan), La_2O_3 (99.99% Wako Pure Chem.) and TiO_2 (99.9% Wako Pure Chem., rutile) were mixed with an aid of ethanol (99.0 Wako Pure Chem.) in an alumina mortar by an automatic grinder for 5 h. The slurry was dried at 60 °C in air for overnight before further 24 h drying in 120 °C vacuum. The dried powder was uniaxially pressed into a green body using a ϕ22 mm die, which was calcined at 800 °C for 10 h, the detailed calcination condition is shown in Table 4.1.

The calcined product was crushed to form precursor powder using alumina mortar and pestle. The precursor powder was then weighed for uniaxial pressing in a ϕ7 mm die to form pellets, which were sealed in rubber probe covers using vacuum pump and subjected to isostatic pressing at 100 MPa for 3 min (Dr. CIP, KOBELCO, Japan). The isostatically press pellet was then sintered to form LLTO under conditions shown in Table 4.2. To prepare for composite fabrication and form ultrafine LLTO powder, the LLTO pellets were crushed in alumina mortar and pestle before ball milling in zirconia pot with zirconia balls (Pulverisette7 premium line, Fritsch, Germany) and ethanol (99% Wako Pure Chem.). The detailed ball milling conditions are listed in Table 4.3.

Table 4.1 Heat-treatment conditions for ^{N}Li and ^{7}Li LLTO calcination.

heating rate	5 °C/min
calcinating temperature	800 °C
calcinating time	10 h
cooling rate	5 °C/min
crucible	Al_2O_3
heat-treat atmosphere	air

Table 4.2 Heat-treatment conditions for natural lithium and ^{7}Li LLTO sintering.

heating rate	5 °C/min
sintering temperature	1300 °C
sintering time	10 h
cooling rate	5 °C/min
crucible	Al_2O_3
heat-treat atmosphere	air

Table 4.3 Ball-milling conditions for fine natural lithium and ^{7}Li LLTO powder formation.

pot and balls	zirconia (Fritsch)
ball size	ϕ5 mm
mass ratio (ball:sample)	10:1
ball-mill stage	Pulverisette7 premium line, Fritsch
duration	60 min
rest interval	60 min
cycles (total ball-milling time)	10 (10 h in total)
ball-mill media	ethanol (99% Wako Pure Chem)

4.2.2. Synthesis of natural lithium and ^{7}Li LATP precursor

Synthesis of natural lithium and ^{7}Li $Li_{1.3}Al_{0.3}Ti_{1.7}(PO_4)_3$ precursor is similar to that described in section 4.2.1. Stoichiometric amounts of starting materials: $^{7}Li_2CO_3$ or natural Li_2CO_3 (99% Wako Pure Chem.), γ-Al_2O_3 (97% Stream Chem., USA), TiO_2 (rutile, 99.9% High Purity Chem., Japan) and $NH_4H_2PO_4$ (99% Wako Pure Chem.) were weighed and mixed in alumina mortar and pestle by hand. The mixture was then transferred into another alumina mortar with a small amount of ethanol (99% Wako Pure Chem.) to form slurry for further mixing in automatic grinder for 5 h. The slurry was then dried at 60 °C in air overnight before drying at 120 °C in vacuum for 24 h, forming powder mixture. The mixture was weighed and uniaxially pressed using a ϕ22 mm die to form green compacts for calcination at 700 °C for 2 h (Table 4.4), after which the green compact was crushed using alumina mortar and pestle to form precursor powder. The LATP precursors were then subjected to ball-milling using zirconia pot and balls with an aid of ethanol to form finer precursor powder (Pulverisette7 premium line, Fritsch). The detailed ball-milling conditions are listed in Table 4.5.

4.2.3. Fabrication of ^{7}Li LATP and LATP – LLTO composite for neutron radiography

To fabricate ^{7}Li pristine LATP samples, the ^{7}Li LATP precursor was uniaxially pressed in a 7 mm × 7 mm rectangular die to form cuboid pellets, which were sealed in rubber probe covers using a vacuum pump and were isostatically pressed under 100 MPa for 3 min (Dr. CIP, KOBELCO). The pellets were then covered by LATP precursor and placed on platinum foil in alumina crucible and sintered under conditions shown in Table 4.6.

To fabricate LATP – LLTO composite pellets, the ^{7}Li LATP precursor and ^{7}Li LLTO powder were firstly mixed by alumina mortar and pestle and then transferred into zirconia pot with zirconia balls and ethanol (99% Wako Pure Chem.) for a 5 h mixing to ensure homogenous dispersion of LLTO among LATP precursor (Pulverisette7 premium line, Fritsch, detailed conditions are shown in Table 4.7). The ball-milled slurry was dried at 60 °C in air and subsequently 120 °C in vacuum for 24 h to remove the moisture and residual ethanol in order to form dried powder mixture. The mixture was weighed and uniaxially pressed to form pellets before being sealed in rubber probe covers by a vacuum pump. The sealed pellets were isostatically pressed under 100 MPa for 3 min (Dr. CIP, KOBELCO) and sintered under conditions listed in Table 4.6, during which the pellets were embedded in LATP – LLTO mixture powder to reduce lithium loss.

To prepare the cuboid samples for neutron radiography experiments, the cuboid samples were

polished on all sides using #1200 grid abrasive paper to achieve consistent dimensions (approximately 8 mm × 6 mm × 6 mm). To reduce permeation in diffusion experiments, a squared side of the samples were polished by up to #3000 grid abrasive paper until mirror finish was achieved.

4.2.4. Neutron radiography experiments

Before diffusion experiments, the samples were placed on an aluminium sample holder and subjected to neutron radiography experiments to check the position of the samples on the radiography images. A borax block was sticked on the sample holder to denote the distinguish the side of composite sample from the pristine sample. The relative positions of the samples on the sample holder were labelled by marker pen and recorded by taking photographs in order to repeat the sample positions in subsequent neutron radiography experiments. The aluminium sample holder was positioned at the centre of the neutron beam.

To prepare the cuboid samples for neutron radiography, saturated aqueous solution of $^{6}LiNO_3$ along with epoxy glue was applied as tracer to the polished side of the sample blocks which was pre-emptively labelled on the sample using a penile. The samples were placed in a tubular furnace to be annealed at 300 to 500 °C for 20 to 30 min in order to evaporate the epoxy glue and allow the tracer diffusion taking place at designated temperatures. The samples were extracted from the furnace and cooled to room temperature before being placed on the aluminium sample holder and subjected to neutron radiography experiments. The positioning of the samples on the sample holder was referred by the markers on the sample holder and previous photographs to improve the reproducibility of the sample positions on the neutron radiography images. The neutron radiography experiments were carried out at the neutron beam port BL-22 RADEN of the Material and Life Science Experimental Facility (MLF) at Japan Proton Accelerator Research Complex (J-PARC), Japan [38]. The spallation neutron source was operated at 709 kW. The neutron images of the transmitted neutron beam were converted by a $^{6}LiF/ZnS$ scintillator (50 μm in thickness) into visible light which is captured by a cooled CCD camera (ANDOR Ikon-L 936, 2048 × 2048 pixels). The CCD camera was operated at consecutive capture mode to capture 5 consecutive images during each neutron radiography experiments. The exposure duration for each image was 3 min.

After neutron radiography, the samples were inserted into the tubular furnace for further 20 to 30 min annealing before a next neutron radiography experiment. This process was repeated several times until a total annealing time reached the designated diffusion time.

Table 4.4 Heat-treatment condition for natural lithium and ^{7}Li LATP calcination.

heating rate	5 °C/min
calcinating temperature	700 °C
calcinating time	2 h
cooling rate	5 °C/min
crucible	Al_2O_3
heat-treat atmosphere	air

Table 4.5 Ball-milling conditions for the fine natural lithium and ^{7}Li LATP precursor formation.

pot and balls	zirconia (Fritsch)
ball size	ϕ5 mm
mass ratio (ball:sample)	10:1
ball-mill stage	Pulverisette7 premium line, Fritsch
duration	60 min
rest interval	60 min
cycles (total ball-milling time)	5 (5 h in total)
ball-mill media	ethanol (99% Wako Pure Chem)

Table 4.6 Heat-treatment conditions for LATP and LATP – LLTO composite sintering.

heating rate	5 °C/min
sintering temperature	1000 °C
sintering time	10 h
cooling rate	5 °C/min
crucible	Al_2O_3 with a Pt foil
heat-treat atmosphere	air

Table 4.7 Ball-milling conditions for LATP precursor – LLTP powder mixture fabrication.

pot and balls	zirconia (Fritsch)
ball size	ϕ5 mm
mass ratio (ball:sample)	10:1
ball-mill stage	Pulverisette7 premium line, Fritsch
duration	60 min
rest interval	60 min
cycles (total ball-milling time)	5 (5 h in total)
ball-mill media	ethanol (99% Wako Pure Chem)

4.2.5. Fabrication of natural lithium LATP – LLTO samples for HR-TEM observation

To fabricate natural lithium LATP – LLTO composite pellets, the natural lithium LATP precursor and 4 wt.% of natural lithium LLTO powder were mixed by alumina mortar and pestle and then transferred into zirconia pot with zirconia balls. A small amount of ethanol (99% Wako Pure Chem.) was added to form slurry before a further 5 h mixing through ball-milling (Pulverisette7 premium line, Fritsch) with conditions same as Table 4.7. The ball-milled slurry was dried at 120 °C in vacuum for 24 h. The mixture was uniaxially pressed and sealed in rubber probe covers by a vacuum pump for isostatic pressing under 100 MPa for 3 min to form pellets (Dr. CIP, KOBELCO). The subsequent sintering was under conditions listed in Table 4.6.

4.2.6. HR-TEM experiments

To prepare the sample for HR-TEM observation, the fabricated natural lithium LATP – LLTO composite pellets were roughly crushed to form coarse powder, which is dispersed on a copper grid sample holder for HR-TEM experiments in National Yunlin University of Science and Technology, Taiwan. To investigate the morphology, chemical composition and crystal structure of the prepared sample, a field-emission TEM (JEM-F200, JEOL, Japan) equipped with EDS detector (Oxford Instruments, UK) was employed. The TEM was operated at 200 kV in STEM mode to generate HR-TEM images.

4.3. Neutron Radiography Investigations

This section focuses on three topics: 1) basic normalising methods that are applied to the raw neutron radiography images obtained from CCD camera such that the noises, artefacts or other aberrations in the images can be minimised, 2) description of a traditional data processing method and an optimised method in calculation process of the tracer diffusion coefficients, and 3) discussion on the calculated tracer diffusion coefficients of pristine LATP and LATP – LLTO composites obtained at 300 °C to 500 °C, and comparison with results reported in other works.

4.3.1. Normalisation method of neutron radiography results

In neutron radiography, the random noise from the neutron flux commonly occurs due to the dark charge build-up in the CCD camera, or the fluctuation of the neutron beam by the fluctuating output at neutron source or scintillation screen [39]. Therefore, 5 radiography images were taken for each sample to obtain smoothened neutron radiography images through averaging calculation using ImageJ. Images with 3 min CCD camera exposure time were also captured without neutron beam (dark image) to probe the noise signal from ambient environment. By subtracting dark image from the averaged images using ImageJ, neutron radiography images with reduced environmental and random noise can be obtained (averaged image with background subtracted).

For most of the direct neutron beams, whether from spallation neutron source or nuclear reactor neutron source, the flux intensity of each point at image plane can be ununiform due to 1) divergence of neutron beam upon leaving the beam guiding tube, 2) asymmetries from neutron source and beam line, 3) irregular beam scattering off the collimator wall, and 4) geometrical difference of the radial distance from the beam aperture to the image plane [39–42]. During the experiment, the neutron radiography images with neutron beam and without samples were captured with 3 min CCD camera exposure time (flux profile image). By dividing the averaged images with background subtracted by the flux profile image, the images with reduced flux aberration can be obtained. The flow chart of the processes described above is summarised in Fig 4.1. The image qualities before and after the normalisation process are shown in Figs 4.2 and 4.3. Before normalisation, the intensity of the flux maxima at the centre and taper towards the edge, which gives an ununiform base intensity as shown in Fig 4.2 (c). After normalisation, the signal becomes even, generating a uniform base intensity (Fig 4.3 (c)).

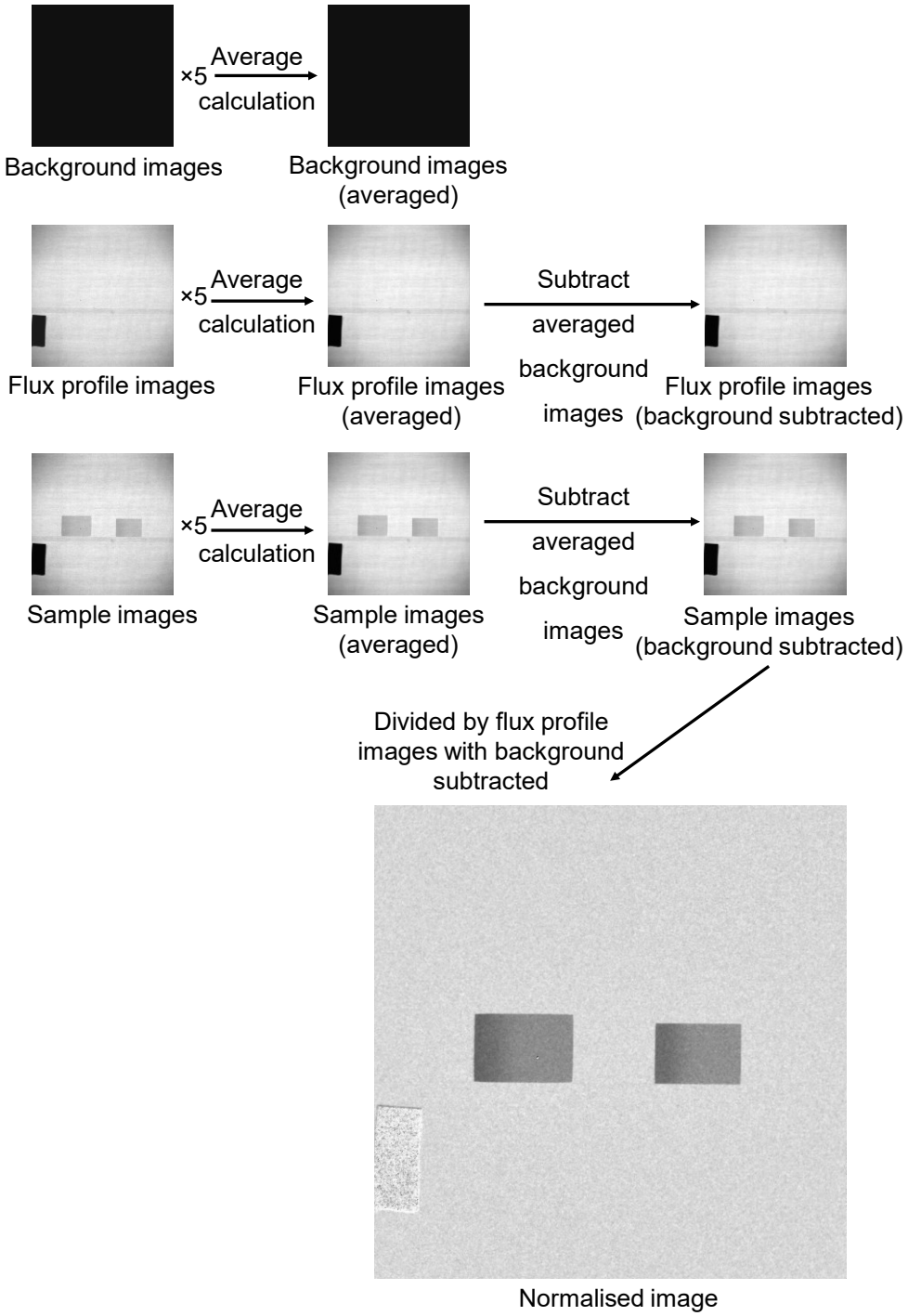

Figure 4.1 Flow chart of normalisation process for the neutron radiography images, taking LATP – LLTO composite (left block) and pristine LATP (right block) after diffusion experiment at 300 °C for 120 min as examples.

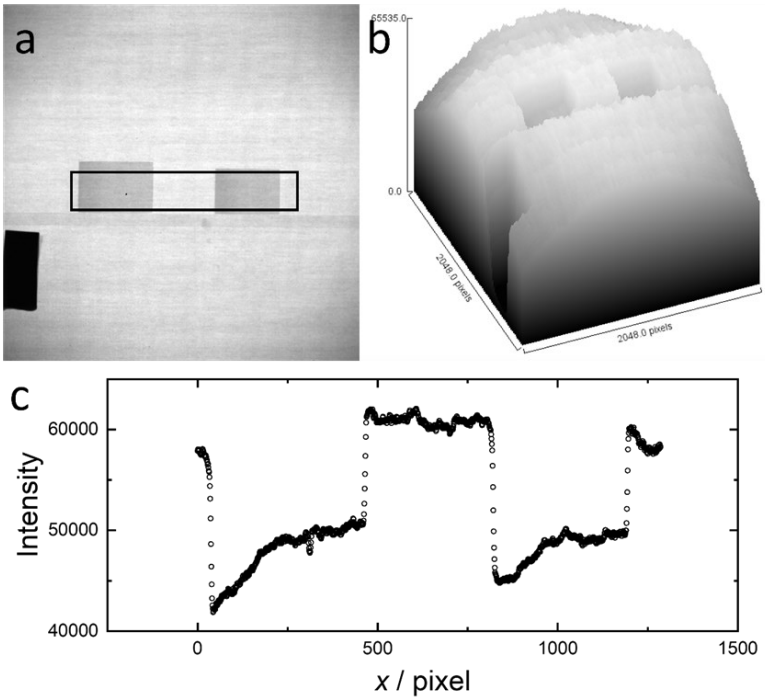

Figure 4.2 (a) Neutron radiography image before normalisation, taking LATP – LLTO (left) and pristine LATP (right) samples after diffusion experiment at 300 °C for 120 min as example. (b) surface plot of signal intensity, (c) intensity profile of the selected area in (a).

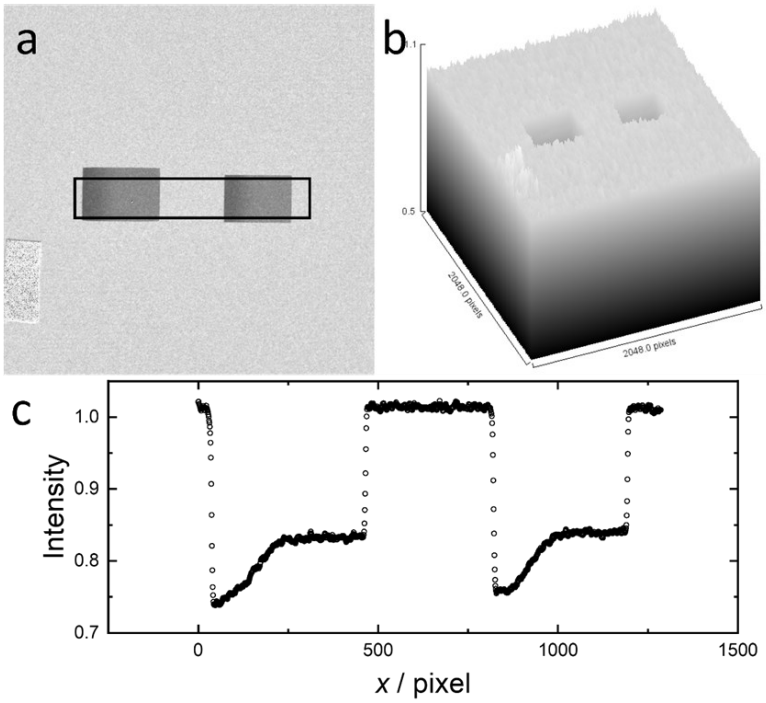

Figure 4.3 (a) Neutron radiography image after normalisation, taking LATP – LLTO (left) and pristine LATP (right) samples after diffusion experiment at 300 °C for 120 min as example. (b) surface plot of signal intensity, (c) intensity profile of the selected area in (a).

4.3.2. Two interpretation methods of neutron radiography results

The most common method to interpretate diffusion coefficient from neutron radiography results is to convert intensity I of the images into concentration c using Beer-Lambert's law to calculate the $\frac{\partial lnc}{\partial x^2}$ term (see next paragraphs) and subsequently diffusion coefficients D. Fig 4.4 (a)-(c) shows typical normalised neutron radiography images of composite and pristine LATP samples after diffusion experiment at 300 °C, of which the intensity profiles are shown in (d)-(e). After diffusion experiments, the ^{6}Li diffused from the diffusion surface towards the bulk interior of the samples, which contributes to the gradual decrease in neutron absorption (i.e., gradual increase in transmitted neutron flux / light intensity) in Fig 4.4 (e) and (f).

According to the Beer-Lambert's law, the concentration of the neutron-scattering species (i.e. ^{6}Li) c can be interpretated by the intensity of the transmitted neutron flux [43]:

$$\varepsilon l c = -\ln\left(\frac{I}{I_0}\right) \qquad (4.1)$$

where I is the attenuated beam intensity, I_0 is the unattenuated beam intensity, ε is the absorptivity of the attenuating species, l is the length of light path (thickness of the sample). Given that the term εl is constant, the concentration of ^{6}Li can be represented by $-\ln(I/I_0)$ with a factor εl^{-1}, as in Fig 4.5. According to the thin-film solution to the Fick's second law [19,20]:

$$c = \frac{M}{\sqrt{4\pi D^* t}} \cdot \exp\left(\frac{-x^2}{4D^* t}\right) \qquad (4.2)$$

where constant M is the total amount of diffusing species, D^* is the diffusion coefficient of ^{6}Li (i.e. tracer diffusion coefficient), t is the diffusion time. The $\frac{\partial lnc}{\partial x^2}$ term can therefore be calculated by measuring the reciprocal of the slope at the linear section of the $\ln(-\ln(I/I_0))$ against x^2 plot to calculate the $-4D^*t$ (shown in Fig 4.6). This method allows calculation of an averaged D^* at a given temperature from a series of D^*t at that temperature, while ignoring the ε and l constants, as shown in Fig 4.7.

The method described above is extensively employed in other works that measures tracer diffusion coefficients through long-range diffusion experiments [19,35–37]. However, this method involves multiple steps of calculation and plotting which can be time consuming. Furthermore, linear fitting on the $\ln(-\ln(I/I_0))$-x^2 plots requires elaboration of range of data points upon which the linear fitting is employed. This can lead to equivocal fitting results since different data section on a same $\ln(-\ln(I/I_0))$-x^2 plot can result in significantly different slopes and hence different tracer diffusion coefficients. Therefore, in this work, nonlinear fittings were employed

directly on the diffusion profiles to utilise the entire data set, which generates more reliable tracer diffusion coefficient results. By combining Eqs 4.1 and 4.2, the relationship between the transmitted neutron signal intensity I and spatial position from diffusion surface x can be expressed by,

$$-\ln\left(\frac{I}{I_0}\right) = \frac{M\varepsilon l}{\sqrt{4\pi D^* t}} \cdot \exp\left(\frac{-x^2}{4D^* t}\right) \qquad (4.3)$$

assuming the pre-exponential term $\frac{M\varepsilon l}{\sqrt{4\pi D^* t}}$ as constant, the $4D^*t$ term can be fitted as a parameter using the exponential equation $y = B \cdot \exp(-x^2/A)$, while avoiding calculating the implicit constants M and ε. The nonlinear fitting results are shown in Figs 4.7 and 4.8, and are listed in Table 4.8 and 4.9, the blue curves are in good agreements with the data points, resulting in R^2 close to unity. The fitted results are also used to calculate the $M\varepsilon l$ terms in Eq 4.3, which are proven to be constant in Table 4.8 and 4.9 for each sample as expected. The different $M\varepsilon l$ values between different samples might be contributed by different amount of $^6LiNO_3$ solution applied and different sample thickness, resulting in different absolute values for M and l.

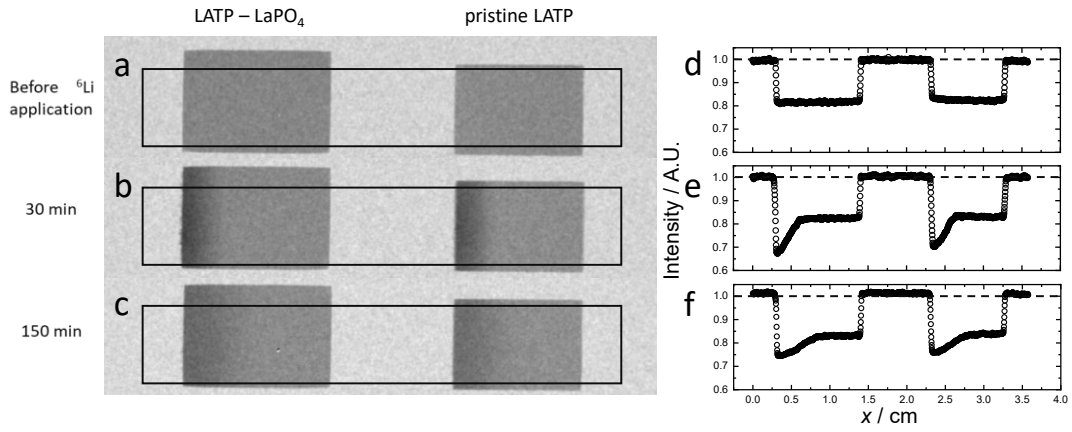

Figure 4.4 Typical normalized neutron radiography images of LATP – LLTO composite (left) and pristine LATP (right) samples (a) before application of $^{6}LiNO_3$, (b) applied with $^{6}LiNO_3$ followed by annealing at 300 °C for 30 min, and (c) annealing at 300 °C for 150 min. Plots (d)-(f) are transmitted intensity profiles corresponding to the selected rectangle areas in (a)-(c).

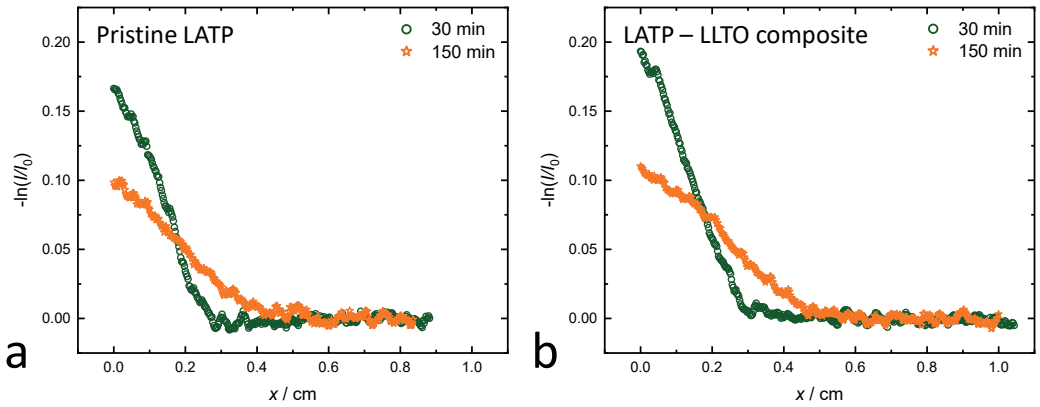

Figure 4.5 Diffusion profiles of (a) pristine LATP sample and (b) LATP – LLTO composite sample after diffusion experiments at 300 °C for 30 and 150 min, converted from the intensity profiles using Beer-Lambert's law.

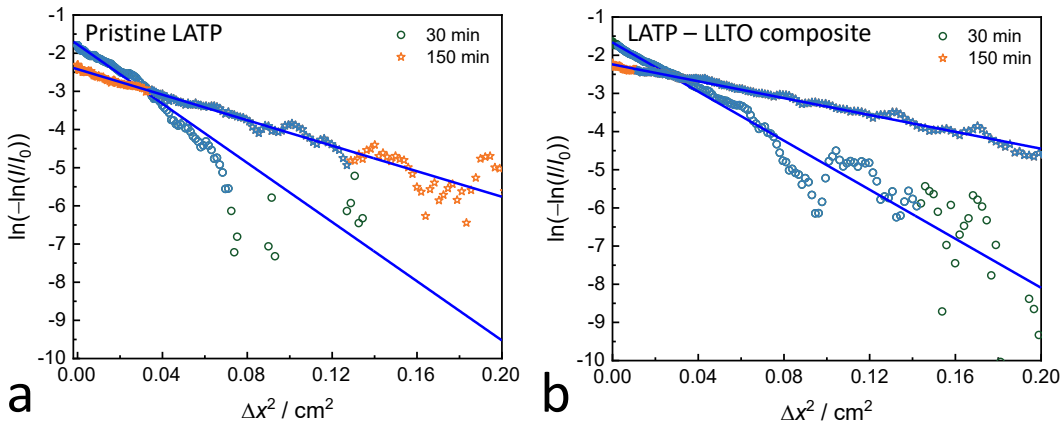

Figure 4.6 $\ln(-\ln(I/I_0))$-x^2 plots of (a) pristine LATP sample and (b) LATP – LLTO composite sample, converted from the diffusion profiles. Dark blue data points indicate the sections which are utilised to perform linear fittings. Blue lines are the results of the linear fittings.

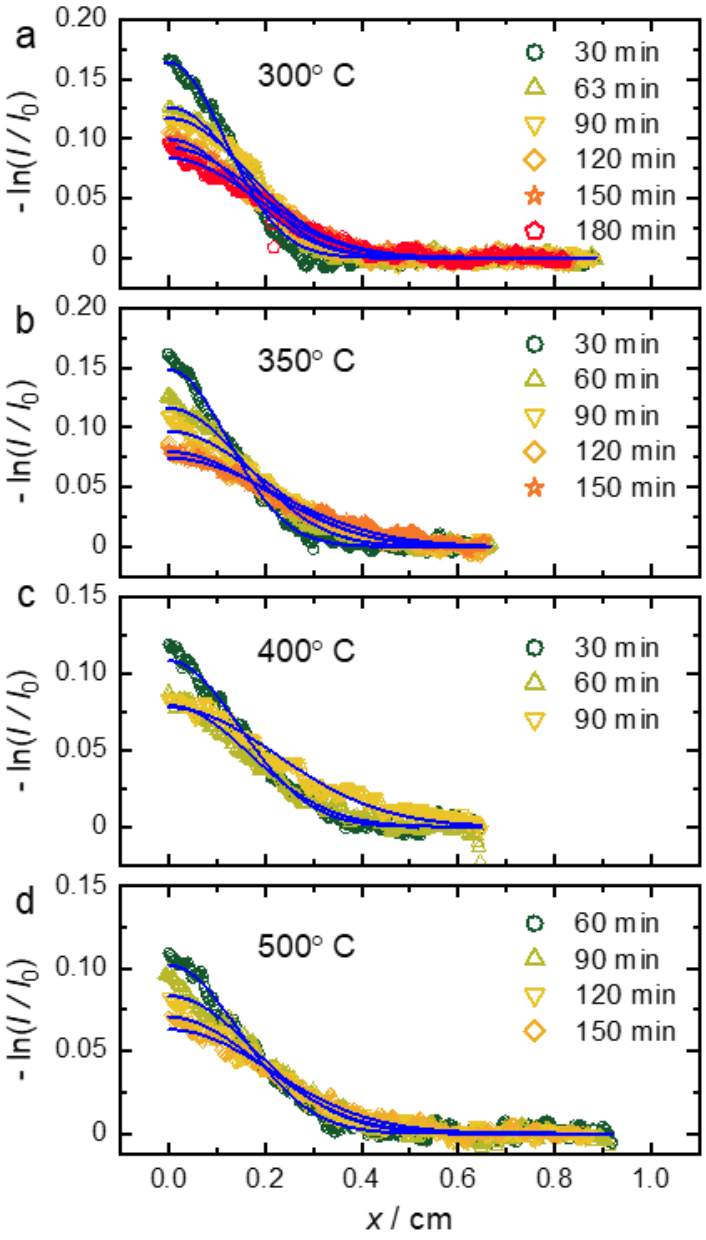

Figure 4.7 Diffusion profiles of pristine LATP with different diffusion times at (a) 300 °C, (b) 350 °C, (c) 400 °C, and (d) 500 °C.

Table 4.8 Results of nonlinear fitting on the diffusion profiles in pristine LATP sample basing on equation $y = B \cdot \exp(-x^2/A)$, $A = 4D^*t$, $B = M\varepsilon l/(4\pi D^*t)^{1/2}$.

temperature, time	*A*	*B*	*Mεl*	χ^2	R^2 (COD)
300 °C, 30 min	0.0271 (4)	0.1636 (9)	4.78E-02	2.54E−5	0.9905
300 °C, 63 min	0.0430 (6)	0.1261 (8)	4.63E-02	2.12E−5	0.9880
300 °C, 90 min	0.0555 (6)	0.1170 (5)	4.89E-02	1.11E−5	0.9932
300 °C, 120 min	0.0446 (5)	0.0993 (4)	3.71E-02	6.87E−6	0.9939
300 °C, 150 min	0.0646 (7)	0.0924 (5)	4.16E-02	8.38E−6	0.9912
300 °C, 180 min	0.0634 (10)	0.0836 (6)	3.73E-02	1.33E−5	0.9842
350 °C, 60 min	0.0431 (6)	0.1019 (6)	3.75E-02	1.18E−5	0.9888
350 °C, 90 min	0.0634 (10)	0.0834 (6)	3.72E-02	1.44E−5	0.9825
350 °C, 120 min	0.0705 (11)	0.0705 (5)	3.32E-02	1.01E−5	0.9832
350 °C, 150 min	0.0895 (15)	0.0630 (4)	3.34E-02	9.55E−6	0.9807
400 °C, 30 min	0.0297 (4)	0.1485 (8)	4.54E-02	2.06E−5	0.9917
400 °C, 60 min	0.0496 (6)	0.1160 (6)	4.58E-02	1.27E−5	0.9924
400 °C, 90 min	0.0710 (9)	0.0966 (6)	4.56E-02	1.36E−5	0.9884
400 °C, 120 min	0.0782 (11)	0.0795 (5)	3.94E-02	9.84E−6	0.9881
400 °C, 150 min	0.0973 (15)	0.0743 (5)	4.11E-02	1.26E−5	0.9812
500 °C, 30 min	0.0424 (6)	0.1084 (7)	3.96E-02	1.52E−5	0.9900
500 °C, 60 min	0.0553 (12)	0.0792 (7)	3.30E-02	2.03E−5	0.9754
500 °C, 90 min	0.0995 (17)	0.0779 (6)	4.36E-02	1.79E−5	0.9744

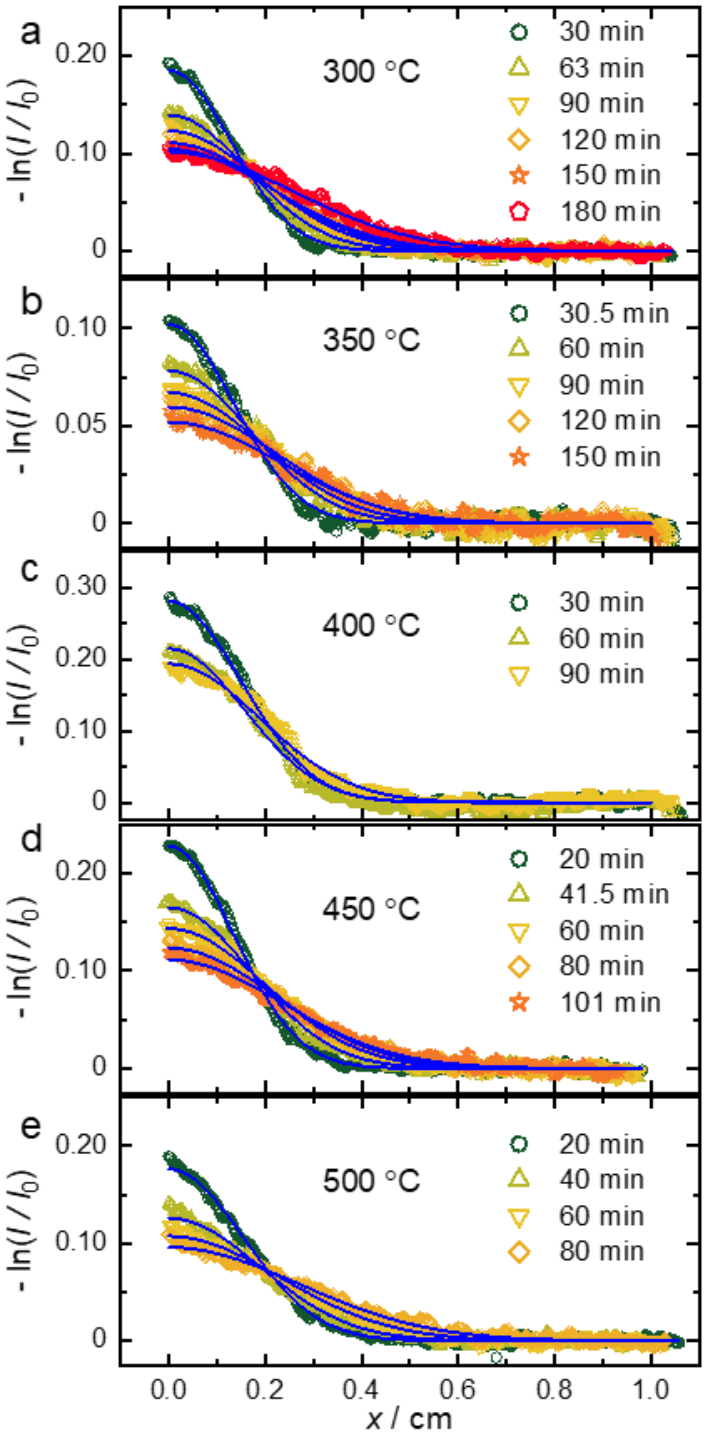

Figure 4.8 Diffusion profiles of LATP – $LaPO_4$ sample with different diffusion times at (a) 300 °C, (b) 350 °C, (c) 400 °C, (d) 450 °C, and (e) 500 °C.

Table 4.9 Results of nonlinear fitting on the diffusion profiles in LATP – $LaPO_4$ composite sample basing on equation $y = B \cdot \exp(-x^2/A)$, $A = 4D^*t$, $B = M\varepsilon l/(4\pi D^*t)^{1/2}$.

temperature, time	A	B	$M\varepsilon l$	χ^2	R^2 (COD)
300 °C, 30 min	0.0333 (2)	0.1851 (6)	5.99E-02	9.18E−6	0.9969
300 °C, 63 min	0.0516 (4)	0.1394 (5)	5.61E-02	1.02E−5	0.9950
300 °C, 90 min	0.0707 (8)	0.1232 (6)	5.80E-02	1.68E−5	0.9906
300 °C, 120 min	0.0833 (8)	0.1108 (5)	5.67E-02	9.87E−6	0.9932
300 °C, 150 min	0.0931 (8)	0.1043 (4)	5.64E-02	7.52E−6	0.9943
300 °C, 180 min	0.1318 (13)	0.1015 (4)	6.53E-02	1.07E−5	0.9919
350 °C, 30.5 min	0.0362 (4)	0.1019 (5)	3.43E-02	7.57E−6	0.9922
350 °C, 60 min	0.0575 (8)	0.0783 (5)	3.33E-02	9.81E−6	0.9854
350 °C, 90 min	0.0751 (11)	0.0671 (5)	3.26E-02	9.30E−6	0.9832
350 °C, 120 min	0.0976 (14)	0.0597 (4)	3.31E-02	6.93E−6	0.9838
350 °C, 150 min	0.1061 (17)	0.0520 (4)	3.00E-02	7.09E−6	0.9792
400 °C, 30 min	0.0447 (3)	0.2812 (8)	1.05E-01	2.08E−5	0.9974
400 °C, 60 min	0.0487 (9)	0.2151 (17)	8.41E-02	1.00E−4	0.9807
400 °C, 90 min	0.0713 (10)	0.1939 (11)	9.18E-02	5.53E−5	0.9871
450 °C, 20 min	0.0359 (2)	0.2278 (5)	7.65E-02	8.00E−6	0.9983
450 °C, 41.5 min	0.0577 (4)	0.1650 (5)	7.03E-02	1.03E−5	0.9965
450 °C, 60 min	0.0788 (5)	0.1434 (4)	7.13E-02	8.20E−6	0.9967
450 °C, 80 min	0.0965 (8)	0.1235 (4)	6.80E-02	1.01E−5	0.9947
450 °C, 101 min	0.1098 (11)	0.1114 (5)	6.54E-02	1.17E−5	0.9925
500 °C, 20 min	0.0472 (3)	0.1762 (5)	6.79E-02	1.05E−5	0.9965
500 °C, 40 min	0.0710 (7)	0.1259 (5)	5.95E-02	1.08E−5	0.9940
500 °C, 60 min	0.1071 (12)	0.1073 (5)	6.22E-02	1.44E−5	0.9899
500 °C, 80 min	0.1471 (15)	0.0970 (4)	6.59E-02	1.09E−5	0.9906

4.3.3. Tracer diffusion coefficients

The D^*t terms obtained from the nonlinear fittings in section 4.3.2 are plotted in Fig 4.9 against diffusion times to calculate the tracer diffusion coefficients from the slopes of the data points, which are listed in Table 4.10. Fig 4.10 is the Arrhenius plot of the measured tracer diffusion coefficients. For comparison, the chemical diffusion coefficients of pristine LATP and LATP – LLTO composites are also calculated from conductivities reported in other works using Nernst-Einstein relation:

$$D_\sigma = \frac{k_B \cdot T}{n \cdot (Z \cdot e)^2} \cdot \sigma \qquad (4.4)$$

where n is the concentration of charge carrier, Z is the valence of charge carrier, e is the charge of an electron, T is the absolute temperature, and σ is the dc ionic conductivity.

The tracer diffusion coefficients of the pristine LATP are generally in good coherent with the results obtained by simulation and SIMS reported by other works [44,45]. The total lithium-ion conductivity at above 130 °C is reported to be dominated by the bulk lithium conduction rather than that from the grain boundary [45]. Therefore, the contribution from the grain boundary diffusion in both pristine LATP and composite samples are negligible, which suggests that the higher diffusion coefficient of LATP – LLTO composite should be contributed by the LATP matrix / $LaPO_4$ particle interface. However, the extent of increase in diffusion coefficients for composite sample at 300 to 500 °C is relatively limited in comparison to room temperature, indicating that the enhancement in lithium-ion migration at LATP matrix / $LaPO_4$ particle interface can become suppressed at elevated temperatures. Such phenomenon resembles the results reported in other halide-based composite lithium-ion conductors [46–48]. As described in chapter 1, section 1.2, the Debye length of the space charge layer surrounding the $LaPO_4$ particles can be largely reduced at 300 °C-500 °C [46,49], leading to thinner space charge layer and therefore a lower conductivity enhancement effect. As a result, the overall diffusion coefficient in composite samples becomes similar to that of the pristine samples.

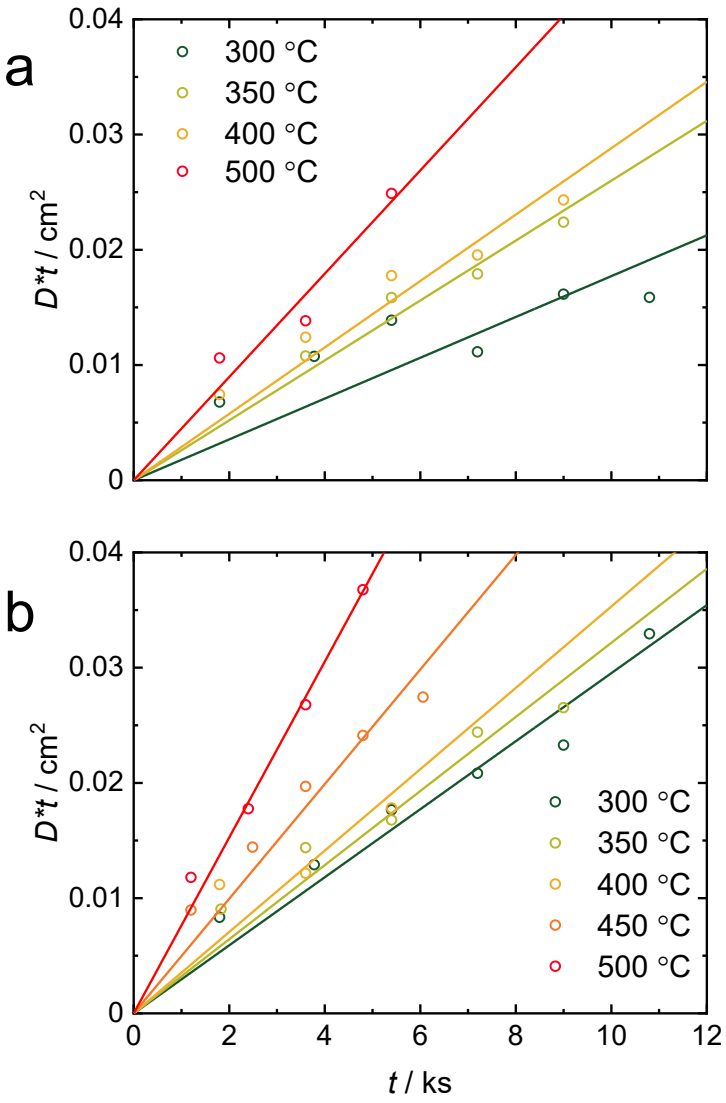

Figure 4.9 *D**t-t* plots for (a) pristine LATP and (b) LATP – $LaPO_4$ composite samples at 300 to 500 °C. Slopes of the lines represent the average *D** at given temperatures.

Table 4.10 Tracer diffusion coefficient of lithium ion in LATP and LATP – $LaPO_4$ composite obtained by neutron radiography.

Temperature / °C	Diffusion coefficient, D^* / 10^{-6} $cm^2 \cdot s^{-1}$	
	pristine LATP	LATP – $LaPO_4$ composite
300	1.71 (20)	2.95 (14)
350	2.60 (12)	3.22 (19)
400	2.88 (16)	3.53 (53)
450	-	4.97 (27)
500	4.48 (37)	7.63 (25)

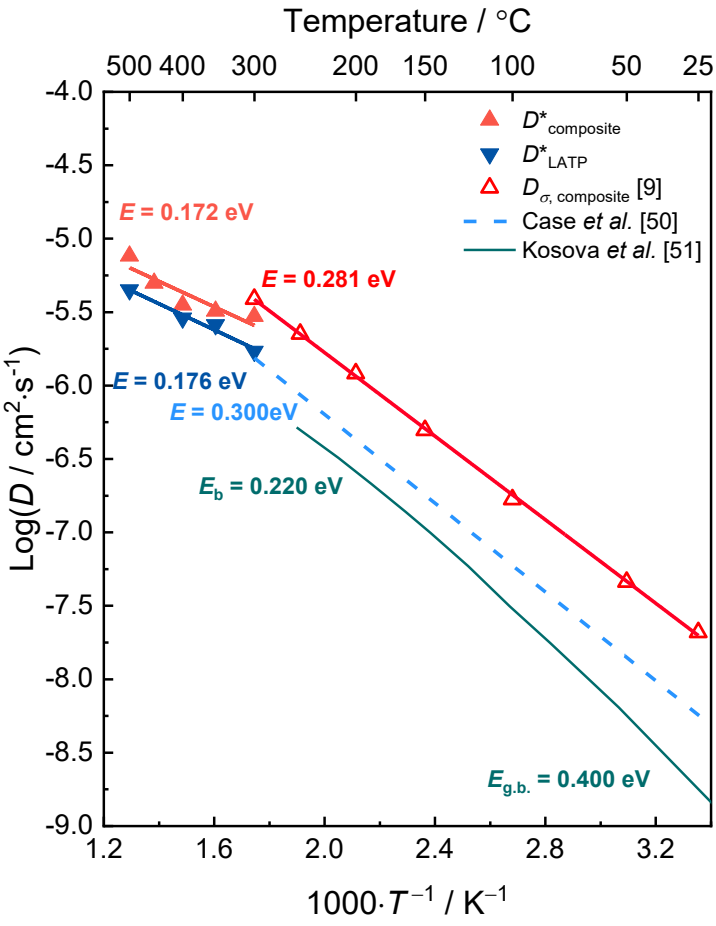

Figure 4.10 Arrhenius plots of the tracer diffusion coefficients of pristine LATP (▼) and LATP – $LaPO_4$ composite (▲). The open triangles are conduction diffusion coefficients LATP – $LaPO_4$ composite calculated from conductivities measured by previous work [1]. The blue dash line and cyan solid line are bulk tracer diffusion coefficient and conduction diffusion coefficients converted from simulation results and conductivity [44,45].

Unlike the grain boundaries which are percolating across the microstructure of polycrystalline samples, the $LaPO_4$ particles are isolated withing the LATP matrix as observed by the scanning electron microscopy (SEM) and HR-TEM experiments in previous works [1,50]. Therefore, while the diffusion coefficients of grain boundaries can be calculated separately from the diffusion profiles once the penetration depth of the diffusion satisfies the condition of the Harrison type B regime (grain boundary width $\delta \leq$ diffusion distance $(Dt)^{1/2} \leq$ grain size d), similar processing is unapplicable to probe the diffusion along the LATP matrix / $LaPO_4$ particle interface. To precisely investigate the diffusion coefficient of interface, short-range diffusion investigation techniques such as solid-state NMR is required [51].

The tracer diffusion coefficients of LATP – LLTO composites are lower than the chemical diffusion coefficients. The Haven ratios of LATP – LLTO composites are ranging from 0.44 to 0.69 (Haven ratio $H_R = D^*/D_\sigma$), which are in good agreements with other inorganic ionic conductors [44,52,53]. It has to be noted that since the tracer diffusion coefficients in this work and conductivities used to calculate the chemical diffusion coefficients are measured from a macroscopic scale, which includes contributions form bulk, grain boundaries and LATP matrix / $LaPO_4$ particle interface. The calculated Haven ratios hence provides limited information about the correlation factors for lithium-ion migration within the samples. A short-range diffusion experiment, solid-state NMR and low temperature EIS characterisations are required to investigate the tracer diffusion coefficients and chemical diffusion coefficients at bulk, grain boundary and interfaces respectively to draw further conclusions.

Since no obvious change in slopes is observed in the Arrhenius plots in Fig 4.10, the activation energy for pristine LATP is believed to be constant within 300 to 500 °C. Given that the diffusion in bulk is the predominant mechanism in pristine LATP at elevated temperatures, the unchanged activation energy suggests a stable NASICON-type lattice structure at elevated temperatures [44,54]. The activation energies for both pristine and composite samples are approximately 0.17 eV, falling within the range of 0.15 - 0.30 eV reported by other works [44,55–57]. This result also suggests that the predominant lithium-ion migration mechanism for LATP – LLTO composite at 300 to 500 °C is bulk diffusion.

4.4. HR-TEM observation

This section demonstrates the TEM experiment results on the LATP – LLTO composite, which substantiate the existence of $LaPO_4$ phase through SAED patterns, and captured multiple high-resolution images at the LATP / $LaPO_4$ boundary area where the LATP matrix and $LaPO_4$ particles are identified with aid of EDS scanning results. The images reveal intimate contacts between the $LaPO_4$ particles and LATP matrix, providing further evidence for the existence of space charge layer at the LATP / $LaPO_4$ interface.

HR-TEM experiments have been conducted to investigate the precise morphology of the dispersed particle in the LATP – LLTO composites. Fig 4.11 shows the TEM images at the boundary area between the matrix and particle. A rod-shaped particle with darker contrast can be distinguished from the matrix, which is estimated to be below 500 nm in size and with an intimate contact with the LATP matrix. The *d*-spacing of the HR-TEM image in Fig 4.11 (b) and the corresponding SAED pattern index in Fig 4.11 (c) identify the particle as the monoclinic structure $LaPO_4$ (a = 0.684 nm, b = 0.708 nm, c = 0.651 and β = 103.24 °). Chemical composition of the particle and matrix areas are studied by the EDS point analysis, the results of which are shown in Fig 4.12. The atomic percentages of the cations in the particle area (upper-right inset) are coincide with the ideal values of $LaPO_4$, while that of the matrix area (lower-left inset) agree with the ideal values of the LATP. These results can confirm that in LATP – LLTO composites, the introduced LLTO particle decomposed into $LaPO_4$ particles and formed LATP matrix - $LaPO_4$ particle microstructure.

Another TEM image with particle / matrix configuration is shown in Fig 4.13, where the dark (a) and bright (b) field images exhibit distinct contrast at the boundary. The intimate contact between the matrix and particle is exhibited in the enlarged image in (c). A line EDS scanning was conducted along the yellow line in Fig 4.13 (c), where the dark contrast represents matrix and bright contrast represents particle. The results in Fig 4.13 (d) shows that the titanium signal from matrix is higher than the particle, while the lanthanum signal from particle is higher. The gradual changes in titanium and lanthanum signals might be caused by the spot size of the incident electron beam or the contribution of the matrix that is lying beneath the $LaPO_4$ particle. Nevertheless, this observation is in good agreement with the chemical composition of the LATP matrix and $LaPO_4$ particle, and further suggests that the introduced LLTO powder decomposed during the sintering of LATP – LLTO composite to form $LaPO_4$ particles that do not contain

titanium. The intimate contact observed in Figs 4.11 and 4.13 can be essential for the space charge layer model which can explain the conductivity improvement in the insulative particle-dispersed ionic conductors [46,47]. For the LATP matrix, the FFT pattern of HR-TEM image at the matrix area in Fig 4.14 is consistent with the structure of LATP with hexagonal lattice ($a = b = 0.850$ nm, $c = 2.08$ nm) [56].

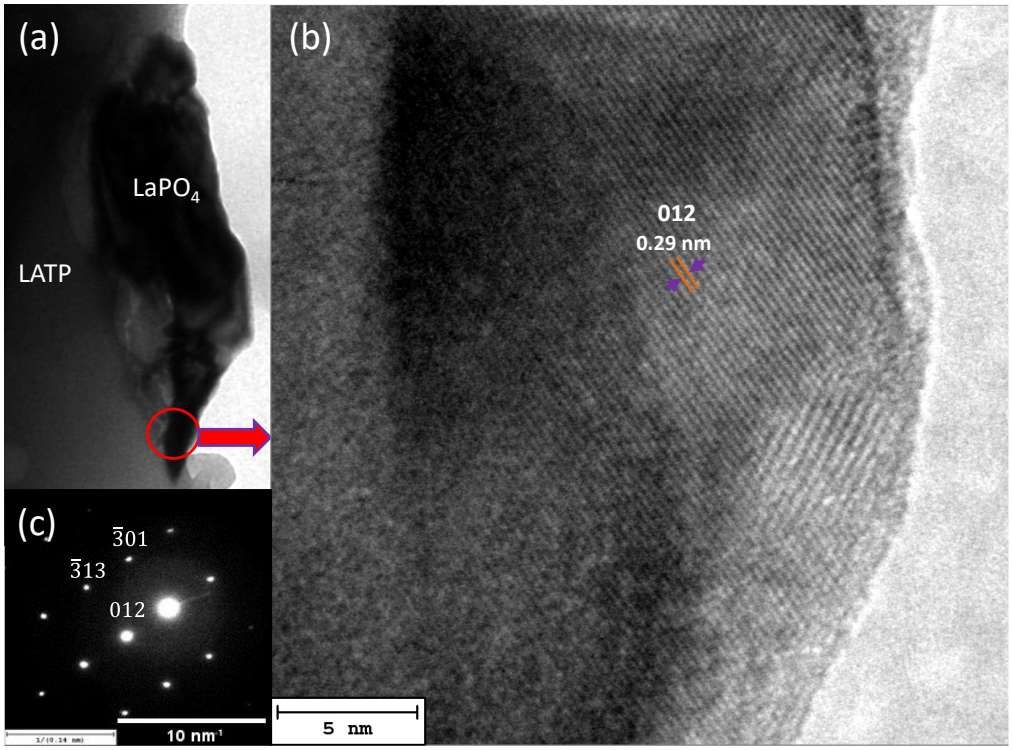

Figure 4.11 (a) TEM image at matrix / particle boundary region. (b) HR-TEM image at the particle area. (c) SAED pattern at the particle area.

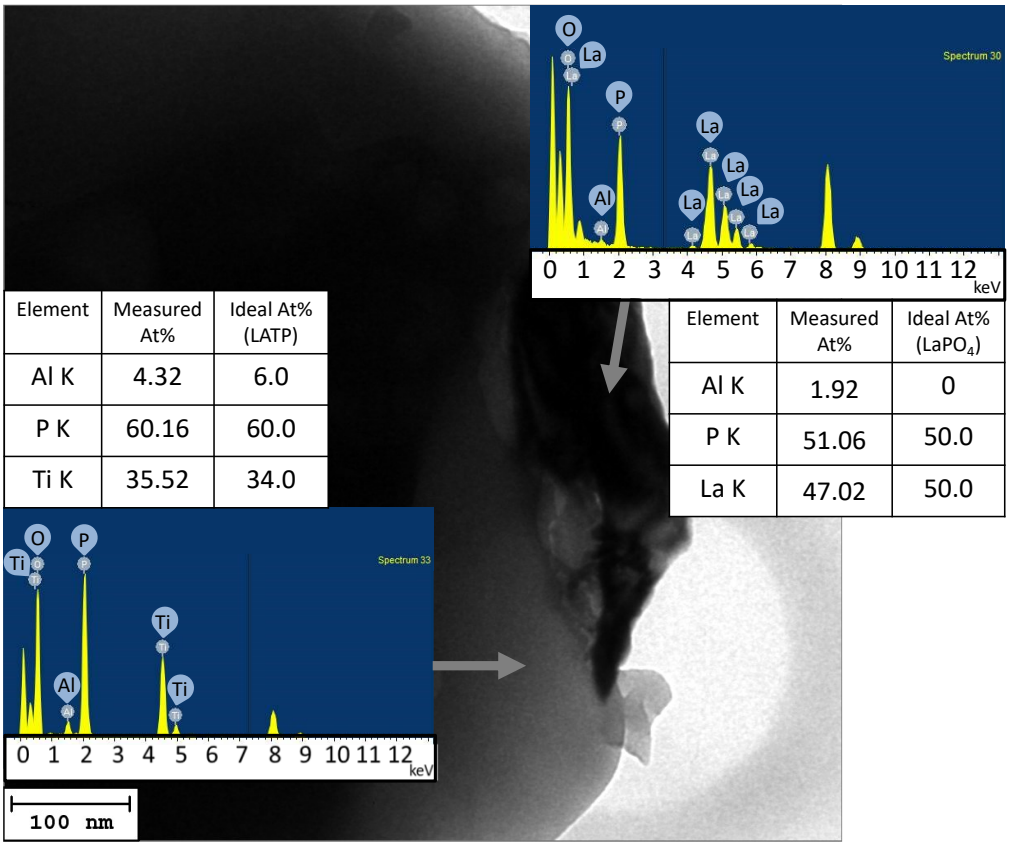

Element	Measured At%	Ideal At% (LATP)
Al K	4.32	6.0
P K	60.16	60.0
Ti K	35.52	34.0

Element	Measured At%	Ideal At% ($LaPO_4$)
Al K	1.92	0
P K	51.06	50.0
La K	47.02	50.0

Figure 4.12 Point EDS results at matrix (lower-left) and particle (upper-right) areas.

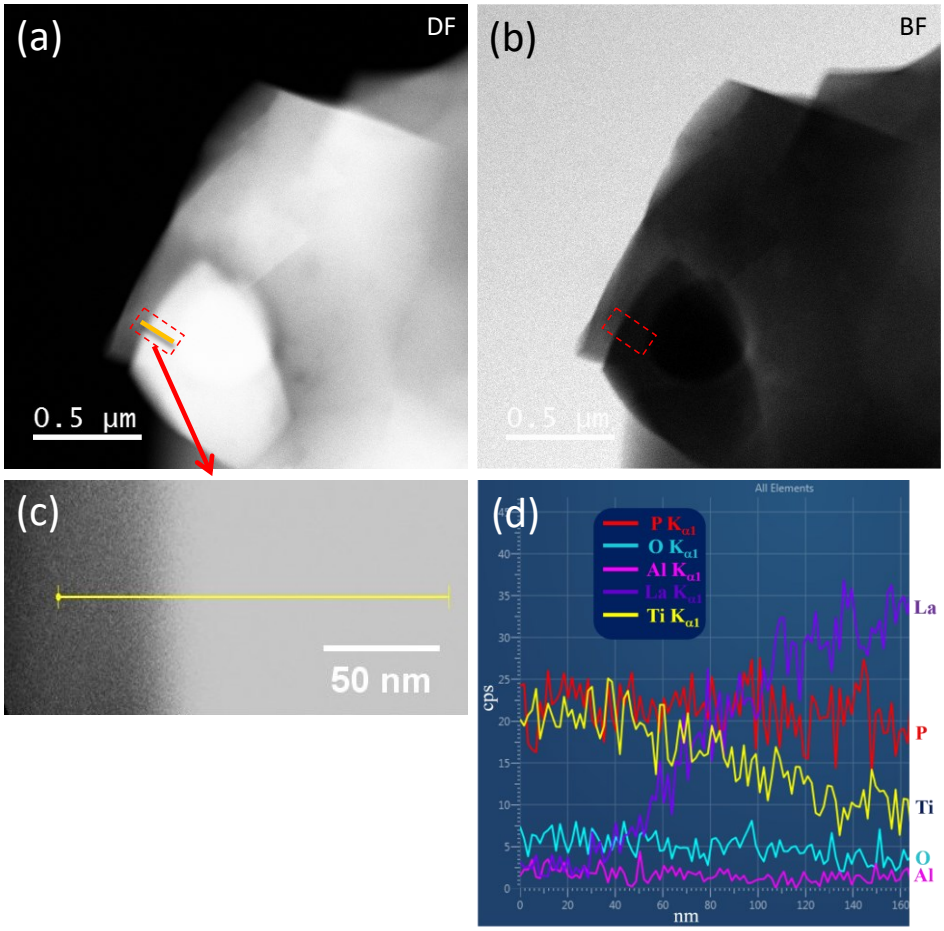

Figure 4.13 (a) and (b) dark field and bright field TEM image at matrix / particle boundary area. (c) Enlarged image at matrix / particle boundary and EDS scanning trace. (d) EDS scanning result.

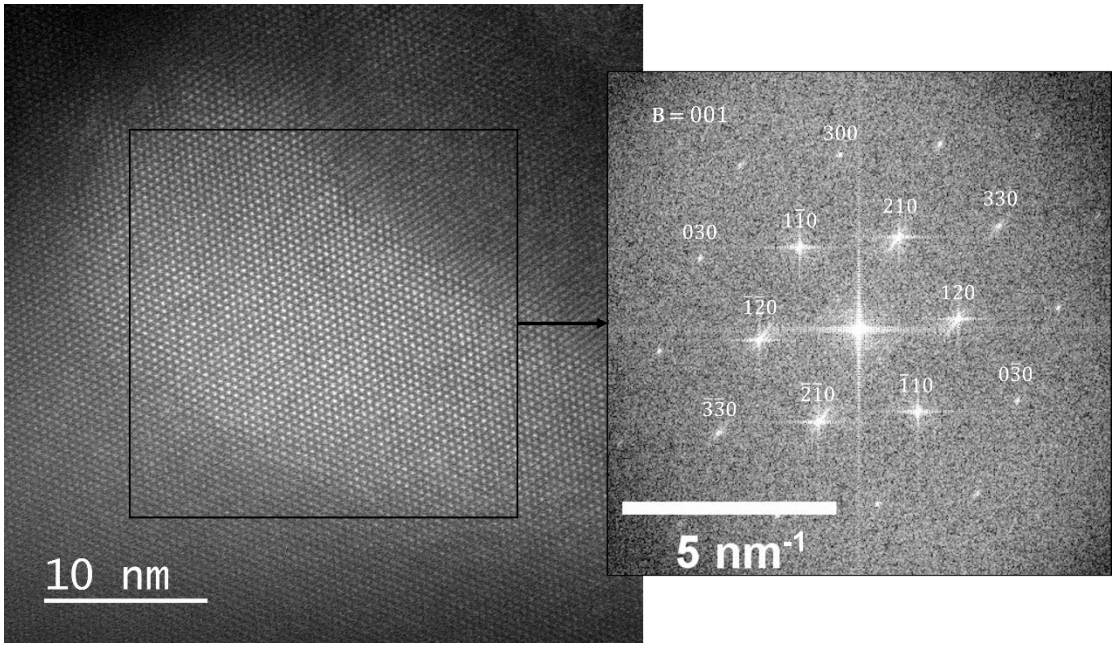

Figure 4.14 HR-TEM image at bulk of LATP matrix and indexed FFT pattern.

4.5. Summary

In summary, the long-range tracer diffusion coefficients of pristine LATP and LATP – $LaPO_4$ composite have been measured in the first time through the neutron radiography technique in the temperature range 300 °C to 500 °C. While the tracer diffusion coefficients of LATP – $LaPO_4$ is slightly higher than that of pristine LATP, the difference is smaller than that expected from the room-temperature conductivity. This is presumably due to the reduced Debye length of the space charge layer which results in an enhanced bulk diffusion contribution in this temperature range. For further precise discussion on the contribution of space charge layer, diffusion measurements should be carried out at lower temperatures where the enhancement effect from space charge layer is more signfinicant, such that the difference in tracer diffusion coefficients between composite and pritine LATP at these tempeartures can be verified. At near room temperatures, owing to the ralatively low lithium mobitliy, solid-state NMR experimens should be employed instead of NR to investigate the lithium diffusion behaviors in composite samples [51]. Nonetheless, it has been revealed that the long-range lithium diffusion in the LATP-based system which demonstrated their potential as solid-state electrolytes for All-Solid-State-Batteries. From HR-TEM and EDS results, the $LaPO_4$ particles dispersed in LATP matrix have been directly observed. TEM images at LATP matrix / $LaPO_4$ particle interface suggest an intimate contact that is attributed to the reaction between LATP precursor and LLTO during the sintering process. Such microstructural feature is essential for the formation of the space charge layer at the LATP matrix / $LaPO_4$ particle interface.

4.6. References

[1] H. Onishi, S. Takai, T. Yabutsuka, T. Yao, Synthesis and electrochemical properties of LATP-LLTO lithium ion conductive composites, Electrochemistry. 84 (2016) 967–970. https://doi.org/10.5796/electrochemistry.84.967

[2] P. Heitjans, S. Indris, Diffusion and ionic conduction in nanocrystalline ceramics, J. Phys. Condens. Matter. 15 (2003) R1257. https://doi.org/10.1557/PROC-676-Y6.6

[3] R.H. Brugge, R.J. Chater, J.A. Kilner, A. Aguadero, Experimental determination of Li diffusivity in LLZO using isotopic exchange and FIB-SIMS, J. Phys. Energy. 3 (2021) 34001. https://doi.org/10.1088/2515-7655/abe2f7

[4] C. Wagner, Investigations on silver sulfide, J. Chem. Phys. 21 (1953) 1819–1827. https://doi.org/10.1063/1.1698670

[5] A. Kuhn, S. Narayanan, L. Spencer, G. Goward, V. Thangadurai, M. Wilkening, Li self-diffusion in garnet-type $Li_7La_3Zr_2O_{12}$ as probed directly by diffusion-induced ^7Li spin-lattice relaxation NMR spectroscopy, Phys. Rev. B. 83 (2011) 94302. https://doi.org/10.1103/PhysRevB.83.094302

[6] A. Kuhn, V. Epp, G. Schmidt, S. Narayanan, V. Thangadurai, M. Wilkening, Spin-alignment echo NMR: probing Li^+ hopping motion in the solid electrolyte $Li_7La_3Zr_2O_{12}$ with garnet-type tetragonal structure, J. Phys. Condens. Matter. 24 (2011) 35901. http://doi.org/10.1088/0953-8984/24/3/035901

[7] V. Epp, Q. Ma, E.-M. Hammer, F. Tietz, M. Wilkening, Very fast bulk Li ion diffusivity in crystalline $Li_{1.5}Al_{0.5}Ti_{1.5}(PO_4)_3$ as seen using NMR relaxometry, Phys. Chem. Chem. Phys. 17 (2015) 32115–32121. https://doi.org/10.1039/C5CP05337D

[8] P. Bottke, D. Rettenwander, W. Schmidt, G. Amthauer, M. Wilkening, Ion dynamics in solid electrolytes: NMR reveals the elementary steps of Li^+ hopping in the garnet $Li_{6.5}La_3Zr_{1.75}Mo_{0.25}O_{12}$, Chem. Mater. 27 (2015) 6571–6582. https://doi.org/10.1021/acs.chemmater.5b02231

[9] K. Hayamizu, Y. Matsuda, M. Matsui, N. Imanishi, Lithium ion diffusion measurements on a garnet-type solid conductor $Li_{6.6}La_3Zr_{1.6}Ta_{0.4}O_{12}$ by using a pulsed-gradient spin-echo NMR method, Solid State Nucl. Magn. Reson. 70 (2015) 21–27. https://doi.org/10.1016/j.ssnmr.2015.05.002

[10] K. Hayamizu, Y. Aihara, Lithium ion diffusion in solid electrolyte $(Li_2S)_7(P_2S_5)_3$ measured by pulsed-gradient spin-echo ^7Li NMR spectroscopy, Solid State Ionics. 238 (2013) 7–14. https://doi.org/10.1016/j.ssi.2013.02.014

[11] K. Hayamizu, Y. Aihara, N. Machida, Anomalous lithium ion migration in the solid electrolyte $(Li_2S)_7(P_2S_5)_3$; fast ion transfer at short time intervals studied by PGSE NMR spectroscopy, Solid State Ionics. 259 (2014) 59–64. https://doi.org/10.1016/j.ssi.2014.02.016

[12] K. Hayamizu, Y. Aihara, T. Watanabe, T. Yamada, S. Ito, N. Machida, NMR studies on lithium ion migration in sulfide-based conductors, amorphous and crystalline Li_3PS_4, Solid State Ionics. 285 (2016) 51–58. https://doi.org/10.1016/j.ssi.2015.06.016

[13] K. Hayamizu, S. Seki, T. Haishi, Lithium ion micrometer diffusion in a garnet-type cubic $Li_7La_3Zr_2O_{12}$ (LLZO) studied using ^7Li NMR spectroscopy, J. Chem. Phys. 146 (2017) 24701. https://doi.org/10.1063/1.4973827

[14] J. Sugiyama, K. Mukai, Y. Ikedo, H. Nozaki, M. Månsson, I. Watanabe, Li diffusion in Li_xCoO_2 probed by muon-spin spectroscopy, Phys. Rev. Lett. 103 (2009) 147601. https://doi.org/10.1103/PhysRevLett.103.147601

[15] Y. Ikedo, J. Sugiyama, O. Ofer, M. Månsson, H. Sakurai, E. Takayama-Muromachi, E.J. Ansaldo, J.H. Brewer, K.H. Chow, Comparative μ^+SR study of the zigzag chain compounds $NaMn_2O_4$ & $LiMn_2O_4$, in: J. Phys. Conf. Ser., 2010: p. 12017. https://doi.org/10.1088/1742-6596/225/1/012017

[16] M. Amores, T.E. Ashton, P.J. Baker, E.J. Cussen, S.A. Corr, Fast microwave-assisted synthesis of Li-stuffed garnets and insights into Li diffusion from muon spin spectroscopy, J. Mater. Chem. A. 4 (2016) 1729–1736. https://doi.org/10.1039/C5TA08107F

[17] H. Nozaki, M. Harada, S. Ohta, I. Watanabe, Y. Miyake, Y. Ikedo, N.H. Jalarvo, E. Mamontov, J. Sugiyama, Li diffusive behavior of garnet-type oxides studied by muon-spin relaxation and QENS, Solid State Ionics. 262 (2014) 585–588. https://doi.org/10.1016/j.ssi.2013.10.014

[18] K. Kamazawa, H. Nozaki, M. Harada, K. Mukai, Y. Ikedo, K. Iida, T.J. Sato, Y. Qiu, M. Tyagi, J. Sugiyama, Interrelationship between Li^+ diffusion, charge, and magnetism in $^7LiMn_2O_4$ and $^7Li_{1.1}Mn_{1.9}O_4$ spinels: Elastic, inelastic, and quasielastic neutron scattering, Phys. Rev. B. 83 (2011) 94401. https://doi.org/10.1103/PhysRevB.83.094401

[19] S.E. Ormrod, D.L. Kirk, The relationship between sodium ion diffusion and conductivity in polycrystalline β"-alumina, J. Phys. D. Appl. Phys. 10 (1977) 1497. https://doi.org/10.1088/0022-3727/10/11/014/

[20] Y. Nosé, T. Ikeda, H. Nakajima, H. Numakura, Tracer and Chemical Diffusion in $L1_2$-Ordered Pt_3Fe, Mater. Trans. 44 (2003) 34–39. https://doi.org/10.2320/matertrans.44.34

[21] E. Zinner, Depth profiling by secondary ion mass spectrometry, Scanning. 3 (1980) 57–78. https://doi.org/10.1002/sca.4950030202

[22] T. Okumura, T. Fukutsuka, Y. Uchimoto, N. Sakai, K. Yamaji, H. Yokokawa, Determination of lithium ion diffusion in lithium–manganese-oxide-spinel thin films by secondary-ion mass spectrometry, J. Power Sources. 189 (2009) 643–645. https://doi.org/10.1016/j.jpowsour.2008.09.043

[23] J. Rahn, E. Hüger, L. Dörrer, B. Ruprecht, P. Heitjans, H. Schmidt, Li self-diffusion in lithium niobate single crystals at low temperatures, Phys. Chem. Chem. Phys. 14 (2012) 2427–2433. https://doi.org/10.1039/C2CP23548J

[24] J. Rahn, P. Heitjans, H. Schmidt, Li self-diffusivities in lithium niobate single crystals as a function of Li_2O content, J. Phys. Chem. C. 119 (2015) 15557–15561. https://doi.org/10.1021/acs.jpcc.5b04391

[25] D. Wiedemann, S. Nakhal, J. Rahn, E. Witt, M.M. Islam, S. Zander, P. Heitjans, H. Schmidt, T. Bredow, M. Wilkening, M. Lerch, Unravelling ultraslow lithium-ion diffusion in γ-$LiAlO_2$: experiments with tracers, neutrons, and charge carriers, Chem. Mater. 28 (2016) 915–924. https://doi.org/10.1021/acs.chemmater.5b04608

[26] N. Kuwata, G. Hasegawa, D. Maeda, N. Ishigaki, T. Miyazaki, J. Kawamura, Tracer Diffusion Coefficients of Li Ions in $Li_xMn_2O_4$ Thin Films Observed by Isotope Exchange Secondary Ion Mass Spectrometry, J. Phys. Chem. C. 124 (2020) 22981–22992. https://doi.org/10.1021/acs.jpcc.0c06375

[27] C. Schwab, A. Höweling, A. Windmüller, J. Gonzalez-Julian, S. Möller, J.R. Binder, S. Uhlenbruck, O. Guillon, M. Martin, Bulk and grain boundary Li-diffusion in dense $LiMn_2O_4$ pellets by means of isotope exchange and ToF-SIMS analysis, Phys. Chem. Chem. Phys. 21 (2019) 26066–26076. https://doi.org/10.1039/C9CP05128G

[28] N. Kuwata, X. Lu, T. Miyazaki, Y. Iwai, T. Tanabe, J. Kawamura, Lithium diffusion coefficient in amorphous lithium phosphate thin films measured by secondary ion mass spectroscopy with isotope exchange methods, Solid State Ionics. 294 (2016) 59–66.

[29] N. Kuwata, M. Nakane, T. Miyazaki, K. Mitsuishi, J. Kawamura, Lithium diffusion coefficient in $LiMn_2O_4$ thin films measured by secondary ion mass spectrometry with ion-exchange method, Solid State Ionics. 320 (2018) 266–271.

[30] M. Kamata, T. Esaka, K. Takami, S. Takai, S. Fujine, K. Yoneda, K. Kanda, Studies on the lithium ion conduction in $Ca_{0.95}Li_{0.10}WO_4$ using cold neutron radiography, Solid State Ionics. 91 (1996) 303–306. https://doi.org/10.1016/j.ssi.2016.06.015

[31] M. Kamata, T. Esaka, K. Takami, S. Takai, S. Fujine, K. Yoneda, K. Kanda, Application of Cold Neutron Radiography to Study the Lithium Ion Movement in $Li_{1.33}Ti_{1.67}O_4$, Denki Kagaku Oyobi Kogyo Butsuri Kagaku. 64 (1996) 984–987. https://doi.org/10.5796/kogyobutsurikagaku.64.984

[32] J.C. Hopkins, D.M. Drake, H. Conde, Elastic and inelastic scattering of fast neutrons from ^6Li and ^7Li, Nucl. Phys. A. 107 (1968) 139–152. https://doi.org/10.1016/0375-9474(68)90731-8

[33] S. Takai, M. Kamata, S. Fujine, K. Yoneda, K. Kanda, T. Esaka, Diffusion coefficient measurement of lithium ion in sintered $Li_{1.33}Ti_{1.67}O_4$ by means of neutron radiography, Solid State Ionics. 123 (1999) 165–172. https://doi.org/10.1016/S0167-2738(99)00095-8

[34] M. Hayashi, H. Sakaguchi, S. Takai, T. Esaka, Lithium ion conduction in scheelite-type oxides and analysis of lithium ion motion by neutron radiography, Solid State Ionics. 140 (2001) 71–76. https://doi.org/10.1016/S0167-2738(01)00704-4

[35] S. Takai, K. Kurihara, K. Yoneda, S. Fujine, Y. Kawabata, T. Esaka, Tracer diffusion experiments on LISICON and its solid solutions by means of neutron radiography, Solid State Ionics. 171 (2004) 107–112. https://doi.org/10.1016/S0167-2738(03)00305-9

[36] S. Takai, T. Mandai, Y. Kawabata, T. Esaka, Diffusion coefficient measurements of $La_{2/3-x}Li_{3x}TiO_3$ using neutron radiography, Solid State Ionics. 176 (2005) 2227–2233. https://doi.org/10.1016/j.ssi.2005.06.012

[37] S. Takai, K. Yoshioka, H. Iikura, M. Matsubayashi, T. Yao, T. Esaka, Tracer diffusion coefficients of lithium ion in $LiMn_2O_4$ measured by neutron radiography, Solid State Ionics. 256 (2014) 93–96. https://doi.org/10.1016/j.ssi.2014.01.013

[38] T. Shinohara, T. Kai, K. Oikawa, T. Nakatani, M. Segawa, K. Hiroi, Y. Su, M. Ooi, M. Harada, H. Iikura, H. Hayashida, J.D. Parker, Y. Matsumoto, T. Kamiyama, H. Sato, Y. Kiyanagi, The energy-resolved neutron imaging system, RADEN, Rev. Sci. Instrum. 91 (2020) 43302. https://doi.org/10.1063/1.5136034

[39] W.J. Richards, M.R. Gibbons, K.C. Shields, Neutron tomography developments and applications, Appl. Radiat. Isot. 61 (2004) 551–559. https://doi.org/10.1016/j.apradiso.2004.03.121

[40] S.H. Giegel, A.E. Craft, G.C. Papaioannou, A.T. Smolinski, C.L. Pope, Neutron Beam Characterization at Neutron Radiography (NRAD) Reactor East Beam Following Reactor Modifications, Quantum Beam Sci. 5 (2021) 8. https://doi.org/10.3390/qubs5020008

[41] S.W. Morgan, J.C. King, C.L. Pope, Beam characterization at the neutron radiography reactor, Nucl. Eng. Des. 265 (2013) 639–653. https://doi.org/10.1016/j.nucengdes.2013.08.059

[42] T. Nemec, J. Rant, E. Kristof, B. Glumac, Characterization of the Ljubljana TRIGA thermal column neutron radiographic facility, in: 2nd Regional Meeting: Nuclear Energy in Central Europe, Portoroz, 1995: pp. 161–167. https://www.osti.gov/etdeweb/servlets/purl/314360.

[43] S. Kasperl, P. Vontobel, Application of an iterative artefact reduction method to neutron tomography, Nucl. Instruments Methods Phys. Res. Sect. A Accel. Spectrometers, Detect. Assoc. Equip. 542 (2005) 392–398. https://doi.org/10.1016/j.nima.2005.01.167

[44] D. Case, A.J. McSloy, R. Sharpe, S.R. Yeandel, T. Bartlett, J. Cookson, E. Dashjav, F. Tietz, C.M.N. Kumar, P. Goddard, Structure and ion transport of lithium-rich $Li_{1+x}Al_xTi_{2-x}(PO_4)_3$ with $0.3< x< 0.5$: A combined computational and experimental study, Solid State Ionics. 346 (2020) 115192. https://doi.org/10.1016/j.ssi.2019.115192

[45] N. V Kosova, E.T. Devyatkina, A.P. Stepanov, A.L. Buzlukov, Lithium conductivity and lithium diffusion in NASICON-type rich $Li_{1+x}Al_xTi_{2-x}(PO_4)_3$ (x=0; 0.3) prepared by mechanical activation, Ionics. 14 (2008) 303–311. https://doi.org/10.1007/s11581-007-0197-5

[46] J. Maier, Ionic conduction in space charge regions, Prog. Solid State Chem. 23 (1995) 171–263. https://doi.org/10.1016/0079-6786(95)00004-E

[47] J. Maier, Pushing nanoionics to the limits: charge carrier chemistry in extremely small systems, Chem. Mater. 26 (2014) 348–360. https://doi.org/10.1021/cm4021657

[48] P. Knauth, Inorganic solid Li ion conductors: An overview, Solid State Ionics. 180 (2009) 911–916. https://doi.org/10.1016/j.ssi.2009.03.022

[49] T. Jow, J.B. Wagner Jr, The effect of dispersed alumina particles on the electrical conductivity of cuprous chloride, J. Electrochem. Soc. 126 (1979) 1963. https://doi.org/10.1149/1.2128835

[50] F. Song, H. Onishi, W.-J. Chen, T. Yabutsuka, T. Yao, S. Takai, TEM Observation of $LaPO_4$-Dispersed LATP Lithium-Ion Conductor, Electrochemistry. (2021) 21–71. https://doi.org/10.5796/electrochemistry.21-00071

[51] S. Breuer, V. Pregartner, S. Lunghammer, H.M.R. Wilkening, Dispersed solid conductors: fast interfacial Li-ion dynamics in nanostructured LiF and LiF: γ-Al_2O_3 composites, J. Phys. Chem. C. 123 (2019) 5222–5230. https://doi.org/https://doi.org/10.1021/acs.jpcc.8b10978

[52] N.M. Vargas-Barbosa, B. Roling, Dynamic ion correlations in solid and liquid electrolytes:

how do they affect charge and mass transport?, ChemElectroChem. 7 (2020) 367–385. https://doi.org/10.1002/celc.201901627

[53] G.E. Murch, The Haven ratio in fast ionic conductors, Solid State Ionics. 7 (1982) 177–198. https://doi.org/10.1016/0167-2738(82)90050-9

[54] K. Arbi, M. Hoelzel, A. Kuhn, F. Garcia-Alvarado, J. Sanz, Local structure and lithium mobility in intercalated $Li_{1+x}Al_xTi_{2-x}(PO_4)_3$ NASICON type materials: a combined neutron diffraction and NMR study, Phys. Chem. Chem. Phys. 16 (2014) 18397–18405. https://doi.org/10.1039/C4CP02938K

[55] S.D. Jackman, R.A. Cutler, Effect of microcracking on ionic conductivity in LATP, J. Power Sources. 218 (2012) 65–72. https://doi.org/10.1016/j.jpowsour.2012.06.081

[56] M. Monchak, T. Hupfer, A. Senyshyn, H. Boysen, D. Chernyshov, T. Hansen, K.G. Schell, E.C. Bucharsky, M.J. Hoffmann, H. Ehrenberg, Lithium diffusion pathway in $Li_{1.3}Al_{0.3}Ti_{1.7}(PO_4)_3$ (LATP) superionic conductor, Inorg. Chem. 55 (2016) 2941–2945. https://doi.org/10.1021/acs.inorgchem.5b02821

[57] X. He, Y. Zhu, Y. Mo, Origin of fast ion diffusion in super-ionic conductors, Nat. Commun. 8 (2017) 1–7. https://doi.org/10.1038/ncomms15893

5. Conclusions and future works

5.1. Conclusions

The works presented in this dissertation focus on the synthesis and characterisations of composite solid-state electrolytes based on NASICON-type compounds, with a goal of achieve and understand the mechanisms of conductivity enhancement through insulative particle dispersion in $Li_{1.5}Al_{0.5}Ge_{1.5}(PO_4)_3$ (LAGP) and $Li_{1.3}Al_{0.3}Ti_{1.7}(PO_4)_3$ (LATP).

Chapter 2 reports the synthesis procedures of forming composite solid-state electrolytes with $LaPO_4$ particle embedded in LAGP matrix through co-sintering of LAGP precursor with $Li_{0.348}La_{0.55}TiO_3$ (LLTO) powder. Powder X-ray diffraction (XRD) and scanning electron microscopy (SEM) observations confirm that the introduced LLTO decomposed to form $LaPO_4$ particles during the sintering, while the crystallographic structure of NASICON-type LAGP is preserved. Electrochemical impedance spectroscopy (EIS) tests suggest that the conductivity of the LAGP – LLTO composites can be improved in comparison to the pristine LAGP, with maximum of 0.40 mS/cm achieved at 4 wt.% of LLTO introduction. According to the Arrhenius plots of temperature-dependent conductivity, the activation energy of conductivity for LAGP – LLTO system is relatively steady despite an increased LLTO content, which suggests that the bulk diffusion in LAGP matrix remains to be the dominant lithium-ion diffusion mechanism in LAGP – LLTO system.

Chapter 3 demonstrates the synthesis methods of type of composite electrolyte that incorporates $LaPO_4$ particles in LATP matrix through co-sintering of LATP precursor with La_2O_3 nano-powder which is referred to as LATP – La_2O_3 composites. $LaPO_4$ particles and $LiTiPO_5$ impurity are identified though powder XRD and SEM investigations. The room-temperature conductivity is increased with the incorporation of $LaPO_4$ particles and peaks to 0.69 mS/cm at 6 wt.% of La_2O_3 addition, followed by steady decrease with further La_2O_3 content. It is also reported that the room-temperature conductivity of LATP – La_2O_3 is inversely dependent to the dwelling time during sintering process. The temperature dependency of conductivities concluded that although the activation energy of conductivity for LATP – La_2O_3 system steadily increases as a function of La_2O_3 addition, the lithium diffusion mechanism at lower La_2O_3 contents remains similar to that of the pristine LATP.

In Chapter 4, lithium-ion diffusion behaviour and $LaPO_4$ particle morphology are investigated

through neutron radiography technique and high-resolution transmission electron microscopy (HR-TEM) respectively. Standardised data processing methods for data normalisation and tracer diffusion calculation are assessed to reduce noise in data and ensure repeatability in calculation results. The obtained tracer diffusion coefficients of pristine LATP and LATP – LLTO composites are in good agreements with the conductivity results from previous work and other published literatures. Within the temperature range from 300 °C to 500 °C, the tracer diffusion coefficient in composite is marginally higher than that of the pristine LATP, which is in contrast with the 3-fold difference in conductivity at room temperature [1]. This result suggests that the contribution to the lithium-ion diffusion from the LATP matrix increases with the temperature and outcompetes that from the space charge layer at the LATP matrix / $LaPO_4$ interface, resulting in an increasingly similar diffusion coefficient in LATP – LLTO composite and pristine LATP. The crystallographic structures of LATP matrix and $LaPO_4$ particles are identified through HR-TEM images and selected area electron diffraction (SAED) patterns. Identification of the two phase subsequently aid to confirm the intimate contact between LATP matrix and $LaPO_4$ particle, which is a key microstructural feature for the formation of space charge layer at the matrix / particle interface.

5.2. Suggested future works

The conductivity enhancement observed in LAGP – LLTO (Chapter 2) and LATP – La_2O_3 composites (Chapter 3) are ascribed to the formation of space charge layer at the vicinity of the matrix / $LaPO_4$ particle interface, which provides fast migration pathway for lithium-ion migration. However, due to the limited amount of interface formation within the composite electrolytes, the relatively unchanged activation energies in both composite systems *viz-a-viz* the pristine LAGP or LATP samples was unable to provide evidence for the existence of space charge layers as a ternary lithium-ion migration mechanism (in addition to the bulk and grain boundary). This requires further EIS characterisations under lower temperatures (e.g. −95 °C to –70 °C) to resolve the semi-circles of bulk, grain boundary and matrix / particle interfaces on the Nyquist plots [2,3]. This would allow respective calculation of bulk, grain boundary and matrix / interface conductivities from the resolved semi-circles, such that i) the existence of space charge layer conductivity can be substantiated, ii) evolution of bulk and grain boundary conductivity as a function of secondary phase incorporation can be observed, and iii) the temperature dependence and activation energies of bulk, grain boundary and matrix / particle interface can be observed and calculated. The obtained information would also enable comparison between difference

composite electrolytes to develop further discussions. Solid-state nuclear magnetic resonance (NMR) has been employed to study the LiF – γ-Al_2O_3 system and successfully observed a motionally narrowed signal on the ^{7}Li NMR spectra that is attributed to the highly mobile lithium ions at the hetero-interface (i.e., LiF matrix / γ-Al_2O_3 particle interface) [4–6]. This is another viable characterisation technique that can be applied to the composite systems reported in this work, which not only reveals the lithium-ion migration at space charge layer but also allows calculation of the proportions of mobile lithium-ions at both the bulk and the matrix / particle interface. In terms of application of the composite electrolytes, LAGP – 4wt.% LLTO and LATP – 6wt.% La_2O_3 composites should be integrated into battery cells to carry out further electrochemical measurements such as cyclic voltammetry test using a full cell with lithium foil as anode to probe the electrochemical stability window of the composite samples and compare with the pristine NASICON electrolytes.

Synthesis wise, Chapter 2 and Chapter 3 have proven that $LaPO_4$ is an effective insulative dispersant to formulate space charge layer at the matrix / particle interface. However, direct incorporation of $LaPO_4$ particles failed to replicate the conductivity enhancement that is observed in LAGP – LLTO and LATP – La_2O_3 composites. Further evidence in Chapter 4 suggests that an intimate contact between insulative particle and ionic-conductive matrix is vital to the formation of space charge layer and subsequent enhancement in conductivity, which might be lack in the case where the NASICON precursors were directly co-sintered with $LaPO_4$ particles. Therefore, engineering of the NASICON matrix / $LaPO_4$ particle interface can be a valuable further work. This topic can be explored by 1) reducing the initial particle size of the initial $LaPO_4$ particles to facilitate recrystallisation during sintering, 2) alter the dwelling temperature of the co-sintering process to facilitate a liquid-phase sintering process such that the $LaPO_4$ phase can be wettened by the NASICON precursor during the sintering or *vice versa*, 3) introducing ternary additives as binders to introduce liquid-phase sintering behaviour. The proposed ideas are focused on enhancing conductivity of NASICON-type lithium-ion conductors by direct incorporation of $LaPO_4$ particles, mainly because that eliminating chemical reactions during the sintering prevents NASICON matrix from donating phosphorus to form $LaPO_4$ with the lanthanum donor, such that formation of impurity phase from decomposition of additives (such as unidentified phases in Chapter 2) or phosphorus depleted NASICON (such as $LiTiPO_5$ in Chapter 3) may be avoided.

5.3. References

[1] H. Onishi, S. Takai, T. Yabutsuka, T. Yao, Synthesis and electrochemical properties of LATP-LLTO lithium ion conductive composites, Electrochemistry. 84 (2016) 967–970. https://doi.org/10.5796/electrochemistry.84.967.

[2] I. V Krasnikova, M.A. Pogosova, A.O. Sanin, K.J. Stevenson, Toward Standardization of Electrochemical Impedance Spectroscopy Studies of Li-Ion Conductive Ceramics, Chem. Mater. 32 (2020) 2232–2241.

[3] C.R. Mariappan, C. Yada, F. Rosciano, B. Roling, Correlation between micro-structural properties and ionic conductivity of Li1.5Al0.5Ge1.5(PO4)3 ceramics, J. Power Sources. 196 (2011) 6456–6464. https://doi.org/10.1016/j.jpowsour.2011.03.065.

[4] S. Breuer, V. Pregartner, S. Lunghammer, H.M.R. Wilkening, Dispersed solid conductors: fast interfacial Li-ion dynamics in nanostructured LiF and LiF: $γ$-Al2O3 composites, J. Phys. Chem. C. 123 (2019) 5222–5230. https://doi.org/https://doi.org/10.1021/acs.jpcc.8b10978.

[5] V. Epp, M. Wilkening, Motion of Li+ in nanoengineered LiBH4 and LiBH4: Al2O3 comparison with the microcrystalline form, ChemPhysChem. 14 (2013) 3706–3713.

[6] V. Gulino, M. Brighi, F. Murgia, P. Ngene, P. de Jongh, R. Černý, M. Baricco, Room-Temperature Solid-State Lithium-Ion Battery Using a LiBH4--MgO Composite Electrolyte, ACS Appl. Energy Mater. 4 (2021) 1228–1236.

List of Publication

Chapter 2

- F. Song, T. Yamamoto, T. Yabutsuka, T. Yao, S. Takai, Synthesis and Characterization of LAGP-Based Lithium Ion-Conductive Composites with an LLTO Additive, *J. Alloys Compd*. **853** (2021) 157089. https://doi.org/10.1016/j.jallcom.2020.157089

Chapter 3

- F. Song, M. Uematsu, T. Yabutsuka, T. Yao, S. Takai, Synthesis and Characterization of Lithium-Ion Conductive LATP-$LaPO_4$ Composites Using La_2O_3 Nano-Powder, *Materials.* **14** (2021) 3502. https://doi.org/10.3390/ma14133502

Chapter 4

- F. Song, H. Onishi, W.-J. Chen, T. Yabutsuka, T. Yao, S. Takai, TEM Observation of $LaPO_4$-Dispersed LATP Lithium-Ion Conductor, *Electrochemistry*. **89** (2021) 480-483. https://doi.org/10.5796/electrochemistry.21-00071

- F. Song, H. Chen, H. Hayashida, T. Kai, T. Shinohara, T. Yabutsuka, T. Yao, S. Takai, Tracer Diffusion Coefficients Measurements on $LaPO_4$-Dispersed LATP by means of Neutron Radiography, Solid State Ionics. **377** (2022) 115873. https://doi.org/10.1016/j.ssi.2022.115873

Acknowledgment

I would like to express my utmost gratitude to Professor Takai Shigeomi for his supervision. His unreserved education demonstrates me the correct way to approach engineering and scientific problems with prudence and integrity. The neutron radiography and other characterisation experiments are impossible to be materialised without his help in corresponding with fellow researchers in J-PARC, JRR-3 and other facilities.

My appreciations also go to Dr. Yabutsuka Takeshi, the inspiring conversations with whom have always been delightful and encouraging. His great skills in shakedown testing and handling of FT-SEM machines are immense help in the microscopic characterisations.

Sincere Acknowledgments to Dr. Hayashida Hirotoshi of CROSS and Shinohara Takenao at J-PARC centre for the helps in neutron radiography experiments, Prof. Chen Wen-Jauh of National Yunlin University of Science and Technology for HR-TEM characterisations, and Dr. Ito Daisuke of Kyoto University Reactor for helps in *in-situ* neutron radiography experiments.

The 3-year-life in the Fundamental Solid-State Chemistry laboratory has been an unforgettable journey thanks to all its members, especially Mr. Yamamoto Takayuki and Mr. Chen Heng, who had laid the foundations in the research on LAGP – LLTO composite and neutron radiography characterisations. Many thanks to Mr. Wu Yuwei and Mr. Xiao Linxu, who have been great teammates and candid friends inside and outside of my research life.

Great thanks to Mr. Kang Jian, Dr. Xie Kaiye, Mrs. Yu Mingzhe and Mr. Matsuki Hisakazu. Despite our different field of research, we shared the bitter and joy, and perhaps the most importantly, the job-hunting information throughout our times as PhD candidates. Hat-tips also to the friends at home for their encouragements and entertainments during my difficult times.

Many thanks to my family for their financial and mental supports, and for believing in me during this journey.

Finally, I would like to thank my better half Miss. Guan Zitong who has been my anchor, emotional support, and a perfect partner. Together we had been through the toughest years during the COVID-19 pandemic as well as my PhD candidacy. Thank you for riding this bumpy road with me.